

*An In-situ Soil Moisture Sensor Array for Real-Time Soil Moisture Depth Sensing.*

*Edward Munns*

School of Civil & Mechanical Engineering Project Thesis  
Curtin University

Semester 2, 2024

Edward Munns, 1/58 Coode Street,  
South Perth,  
WA 6151

29/10/2024

The Head  
School of Civil & Mechanical Engineering,  
Curtin University,  
Kent Street,  
Bentley,  
WA 6102

Dear Sir,

I submit this thesis entitled “*An In-situ Soil Moisture Sensor Array for Real-Time Soil Moisture Depth Sensing*”, based on MXEN4000 Mechatronic Engineering Research Project 1 and MXEN4004 Mechatronic Engineering Research Project 2, undertaken by me as part-requirement for the degree of B.Eng. in Mechatronic Engineering.

Yours faithfully,



Edward Munns  
18871773

## **Acknowledgments**

### **Professor Tele Tan.**

I would like to thank Professor Tele Tan for the guidance and direction he provided throughout the course of this thesis project. In particular, he has my thanks for his advice to carry out the optimization phase of this project with a software modelling approach, this advice is the primary reason the design presented in this work was functional.

### **Dr Julia Easton.**

I would like to thank Dr Julia Easton for her advice on experimental design for the characterization phase of this project. This was an aspect of the project that was underestimated until the process of developing the experimental procedure began. Her advice to read into the literature to assist in planning the experiment was invaluable.

### **Mr Jayden Ng.**

I would like to thank my peer Jayden Ng who worked on the signal generation, conditioning and conversion side of this project throughout the course of this work.

## **Abstract**

In recent years, the widespread adoption of minimum tillage sowing systems in the Australian agricultural industry has enabled the use of a crop sowing optimization method known as moisture seeking. In moisture seeking, seed placement depth is adjusted downwards in the soil profile to place seed at a soil layer with enough moisture to allow germination to begin immediately after planting and crop emergence dates to be predicted with a high level of confidence. The adjustment process on sowing machines currently must be performed manually. This work performed an initial investigation into the viability of a closed loop control system to automate this process with a focus on the design of a capacitive soil moisture sensing array designed to be placed in the feedback loop of such a control system. First, an initial PCB based design was developed incorporating an array of 4 capacitive soil moisture sensors covered by an  $Al_2O_3$  substrate as an environmental shield. An investigation was then performed to compare the performance of coplanar (CPC) and inter-digital (IDC) capacitive sensor designs for this use-case. The work found CPC designs to be better suited to this sensing domain due to demonstrating lower attenuation of the fringing fields when penetrating the shield layer. Finite Element Analysis (FEA) modelling was then performed to optimize sensor design during which 2 optimizations pathways were compared, doubling the length of the CPC and mirroring sensor electrodes on both sides of the PCB. Simulations demonstrated the electrode mirroring technique to be the superior optimization pathway for this use-case as it resulted in shifts upward in both the minimum and maximum values of C and percentage  $\Delta C$  of the sensors, while doubling length resulted in only a scaling of the minimum and maximum values of C. A prototype was then designed and constructed using the results of the modelling and an attempt at characterization of the sensor array was performed over several clay and sand mixtures. This characterization demonstrated the sensor array could provide functionality in this sensing environment; however, the results demonstrated a more in-depth study would be required for full characterization of the design.

## Table Of Contents

1. Introduction .....	1
2. Literature Review.....	2
3. Background .....	4
3.1 Crop Establishment and Sowing Time .....	4
3.2 Moisture Seeking to Optimize Crop Emergence .....	5
3.3 Nil-till and No-till Sowing Systems.....	5
3.4 Constraints of the Sensing Environment.....	6
3.5 Capacitive Sensors in Moisture Sensing.....	6
3.6 Challenges in Soil Moisture Sensing .....	9
4. Design and Development of Sensing Prototypes.....	13
4.1 Investigation and Initial Design Development .....	13
4.1.1 Dealing with the Sensing Environment .....	13
4.1.2 Comparison of Commercially Available CPC and IDC Sensors.....	14
4.1.3 Frequency Analysis.....	15
4.1.4 Substrate Penetration .....	16
4.2 Design Optimization .....	17
4.2.1 Design Parameters Examined .....	17
4.2.2 Device Under Test Layout .....	17
4.2.3 Description of Modelling World.....	19
4.2.4 Optimization .....	20
4.2.5 Design Selection .....	20
4.3 Prototype Fabrication.....	20
4.3.1 PCB Design.....	20
4.3.2 PCB Fabrication.....	20
4.3.3 Prototype Validation .....	20
4.4 Frequency Analysis of Prototype.....	20
4.4.1 Apparatus: .....	21
4.4.2 Methodology:.....	21
4.4.3 Results Analysis:.....	21
4.5 Characterization of Prototype .....	21
4.5.1 Apparatus: .....	21
4.5.2 Test Samples: .....	22
4.5.3 Sample Preparation: .....	23
4.5.4 Approach to Measurement:.....	23
4.5.5 Results Analysis:.....	24
5. Results and Discussion .....	25

5.1 Investigation and Initial Design Development .....	25
5.1.1 Frequency Analysis of IDC and CPC sensors .....	25
5.1.2 Substrate Penetration .....	28
5.2 Design Optimization .....	30
5.2.1 Visual Examination of E-Field Simulations .....	30
5.2.2 IDC Modelling .....	32
5.2.3 Data Presentation of CPC Modelling.....	33
5.2.4 CPC Single vs Dual Sided .....	34
5.2.5 CPC Dual Sided 40mm vs 80mm Length.....	38
5.2.6 Selection of Sensor Design .....	41
5.3 Prototype Fabrication and Verification.....	41
5.3.1 PCB Design.....	41
5.3.2 PCB Fabrication.....	42
5.3.3 Prototype Validation .....	43
5.4 Frequency Analysis of Prototype.....	44
5.5 Characterization of Prototype .....	45
5.5.1 Initial Attempt at Characterization.....	45
5.5.2 Updates to Characterization Methodology .....	48
5.5.3 Second Attempt at Characterization .....	49
6. Conclusions.....	51
7. Future Work .....	52
7.1 Evaluation of Mechanical Performance of Shield in Real-World Environment .....	52
7.2 In-Depth Characterization of Sensor Response to Soil Texture .....	52
7.3 Examination of Lower Frequency Sensor Response to Characterize Conductivity .....	52
References.....	53
Appendix A: Coleoptile Length Classification of Certain Wheat Varieties .....	A
Appendix B: Deviation of Method Described by Rego Segunda et al .....	B
Appendix C: Properties Table of Alumina Ceramics .....	C

## Table of Figures

Figure 1: Wheat seed during germination.....	4
Figure 2: Diagram of "Nill-Till" sowing system .....	5
Figure 3: Parallel Plate Capacitor .....	6
Figure 4: Electric Field of Parallel Plate Capacitor .....	6
Figure 5: Transformation from Parallel Plate to Coplanar Capacitor.....	7
Figure 6: Coplanar Capacitor and Coplanar Capacitor with Ground Plane.....	7
Figure 7: Diagram of IDC.....	8
Figure 8: Soil Texture Triangle.....	9
Figure 9: Complex Permittivity of Water as a Function of Frequency.....	10
Figure 10: Complex Permittivity of Water and Kaolinite Clay Mixtures .....	10
Figure 11: Relative Permittivity vs VMC at Variable Soil Porosities .....	11
Figure 12: Initial Design Layout of Sensor Array .....	14
Figure 13: Radiocontrolli IDC Sensor and Grow CPC Sensor.....	15
Figure 14: Apparatus used for frequency analysis.....	15
Figure 15: Circuit used for frequency analysis .....	16
Figure 16: Substrate penetration testing setup .....	17
Figure 17: CPC and IDC Sensor Array Layout for FEA modelling.....	18
Figure 18: FEA Modelling World Diagram.....	19
Figure 19: Range of Soil Textures used for Creating Samples.....	22
Figure 20: Grow CPC Sensor Frequency Plot.....	26
Figure 21: Radiocontrolli IDC Sensor Frequency Plot.....	27
Figure 22: Result of IDC Al <sub>2</sub> O <sub>3</sub> substrate penetration testing.....	28
Figure 23: Result of CPC Al <sub>2</sub> O <sub>3</sub> substrate penetration testing.....	29
Figure 24: Visual Comparison of E-Field for CPC and IDC Designs.....	31
Figure 25: Simulation of E-Field in Air and Water .....	31
Figure 26: Simulation Results for Dual Sided 40mm IDC .....	32
Figure 27: A Note on Data Presentation for CPC Modelling .....	33
Figure 28: Simulation Results for Single Sided 40mm CPC.....	34
Figure 29: Simulation Results of Dual Sided 40mm CPC.....	35
Figure 30: Change in Capacitance of Single and Dual Sided 40mm CPC.....	36
Figure 31: Percentage Change in Capacitance of Single and Dual Sided 40mm CPC.....	36
Figure 32: Change in E Field in MUT of Single and Dual Sided 40mm CPC .....	37
Figure 33: Simulation Results of Dual Sided 80mm CPC.....	38
Figure 34: Change in Capacitance of Dual Sided 40mm and 80mm CPC .....	39
Figure 35: Percentage Change in Capacitance of Dual Sided 40mm and 80mm CPC.....	39
Figure 36: Change in E Field in MUT of Dual Sided 40mm and 80mm CPC .....	40
Figure 37: KiCad PCB Design of Prototype.....	42
Figure 38: Bare PCB of Prototype and with Al <sub>2</sub> O <sub>3</sub> Shield Installed .....	43
Figure 39: Results of Prototype Verification Frequency Sweep .....	43
Figure 40: Prototype Frequency Sweep Apparatus .....	44
Figure 41: Prototype Frequency Sweep Results .....	44
Figure 42: Table of Results from Initial Attempt at Characterization .....	45
Figure 43: Plot of First Attempt at Characterization .....	46
Figure 44: Examination of Sensor-to-Sensor Variability for Sandy Loam Dataset .....	47
Figure 45: IDC Optimization Model Parameters .....	47
Figure 46: Revised Sensor Connection Method .....	48
Figure 47: Table of Results for Second Attempt at Characterization .....	49
Figure 48: Plot of Second Attempt at Characterization .....	49
Figure 49: Coleoptile length, establishment , and yield of wheat varieties at variable depth .... A	A

Figure 50: List of wheat varieties and their coleoptile group classifications. .... A  
Figure 51: Properties Table of Alumina Ceramics ..... C

## Nomenclature

Symbols	Definition	SI unit
V	Voltage	Volt
$V_{pp}$	Peak to peak voltage	Volt
Q	Electric charge	Coulomb
f	Frequency	Hertz
$f_{cutoff}$	Cut-off frequency	Hertz
$\omega$	Angular frequency	Radians/second
R	Resistance	Ohms
C	Capacitance	farad
j	Imaginary unit	-
$\epsilon_0$	Permittivity of free space, $8.854 \times 10^{-12}$	farads/meter
$\epsilon$	Absolute complex permittivity	farads/meter
$\epsilon'$	Real component of $\epsilon$	-
$\epsilon''$	Imaginary component of $\epsilon$	-
$\epsilon_r$	Relative complex permittivity	-
$\epsilon_r'$	Real component of $\epsilon_r$	-
$\epsilon_r''$	Imaginary component of $\epsilon_r$	-
$\Delta$	Change in	-

## Abbreviations

Abbreviations	Definition
MUT	Material under test
DUT	Device under test
PCB	Printed circuit board
FDR	Frequency domain reflectometry
PPC	Parallel plate capacitor
CPC	Coplanar capacitor
IDC	Inter-digital capacitor
DMM	Digital multi-meter
AC	Alternating current
VMC	Volumetric Moisture Content
GMC	Gravimetric Moisture Content

## **1. Introduction**

For cereal crop growers in the Australian agricultural industry, one of the points in a season most critical to crop yield, risk management, and profitability outcomes occurs early in the season during the crop sowing stage. Crop varieties can be broadly classified into long, mid and short season, with ideal crop emergence date windows and time to flowering varying greatly between these classes. It is common practice in the industry to begin sowing operations with long season varieties, then switch to mid and short season varieties as sowing progresses. These variety specific optimizations of sowing, germination, and emergence dates are performed early in the season, but the main intention of these optimizations is to shift the crop flowering window to a point at the end of the season with a high probability of favourable climatic conditions for grain development and finishing. Ideally, flowering should occur after the risk of frost has diminished so flower frost risks are lowered, and grain development should be complete before temperatures increase towards the end of the spring season (Department of Primary Industries 2024).

Seed can be either “wet sown” or “dry sown”. In wet sowing, seed is planted into wet soil with enough moisture present to allow the germination process to begin immediately and seedling emergence time is known at the time of sowing. In dry sowing, seed is planted into dry soil and germination cannot begin until the next rainfall event occurs. Emergence time for dry sown crops is therefore dependant on climatic conditions. For this reason, the wet sowing process is preferable to dry sowing, but the large areas that must be sown in the Australian agricultural industry require a large portion of the national crop to be dry sown due to the logistics of covering such large areas (GRDC 2016).

In the last few decades, the method of crop sowing in Australia has seen a large shift away from the traditional full tillage methods towards more recently developed minimum tillage methods. Traditional full tillage methods till soil in a wide, shallow pattern with the intention of maximizing mechanical weed control in front of planting. In contrast, minimum tillage sowing systems cut narrow, deep slots into the soil at wider row spacings and offer vastly superior control of seed and fertilizer placement in the soil profile. Over 70% of Australian cereal crops are now sown using this minimum tillage method (Llewellyn and Ouzman 2020).

The increase in control of seed placement bought about by the widespread adoption of minimum tillage sowing systems brings with it a sowing optimization pathway known as moisture seeking. In moisture seeking, the sowing depth is manually adjusted on the sowing machine to place seed deeper into the soil profile at a soil layer containing enough moisture to allow the germination and emergence process to begin immediately. Planting seed at this point in the soil profile allows the benefits of wet sowing in conditions that traditionally would have had to be dry sown (GRDC 2024).

Adjustment of sowing depth on sowing machines must currently be performed manually, but developments in the fields of embedded electronics and soil moisture sensing in recent years may enable this process to be automated. This thesis performs an initial investigation into the viability of a closed loop control system to automate the adjustment of seed placement and enable control of hardware during these moisture seeking operations. The focus of this work is on the development of a capacitive soil moisture sensing array designed for use in the feedback loop of such a control system.

## 2. Literature Review

This research began with an in-depth review of the current literature. The purpose of this review was to establish the current state and trends of soil moisture sensing, to identify technologies applicable to the real-time, in-situ requirements of this application, and to identify related works this research could build upon.

Yu et al published a review of soil moisture sensing technologies and research in 2021. In this review weight, tensiometer, neutron probe, gamma-ray, infra-red, and dielectric soil moisture sensing methodologies were examined. A summary of the major findings of previous studies into many commercially available sensors was included in this review. Capacitive sensors were identified as providing major cost benefits over time domain reflectometry devices, but the review also highlighted the importance of correction algorithm optimization in providing accurate measurements. Factors affecting accuracy of capacitive sensors identified include installation method, temperature drift, soil type, ionic conductivity and unoptimized or inappropriate algorithms (Yu, et al. 2021).

Escriba et al developed a co-planar soil sensor capable of sensing both soil salinity at lower frequency (300-1000 kHz) and soil moisture at higher frequency (4-10 MHz) by switching of the oscillation sources providing excitation to the sensor. This design was based on a traditional coplanar capacitor (CPC) design with electrodes arranged in a novel double helix layout. Results showed dissolved Ionics present in the material under test (MUT) lead to high variability of moisture readings at lower frequencies with these readings converging at higher frequencies. This work also examined the effects of including a polymer layer encasing the sensor to provide mechanical shielding. This shielding demonstrated a constant increase in measured capacitance across the 10-60% soil moisture range of an estimated 14.7pF and an overall reduction in sensor sensitivity of 12% due to the additional parasitic capacitance introduced by this layer (Escriba, et al. 2020).

Claudel et al presented an analytical method for optimization of interdigital capacitive (IDC) sensors. Results of this method were validated against finite element analysis simulations. This study demonstrated penetration depth and bandwidth were largely dependent upon electrode and inter-electrode gap widths (Claudel, et al. 2021).

Patle et al developed a sensor array consisting of 5 sensors placed at 5 cm increments over a 25 cm soil depth profile. These sensors were IDCs constructed on a 2-layer PCB with the IDC electrodes mirrored on both sides. This mirroring of the electrodes demonstrated a tripling of capacitance compared to earlier works with an average  $\Delta C$  of 300pF across the 5 sensors. The design used time domain multiplexing to iterate through all sensors in the array over a 250ms period with output signals fed into a counter to convert capacitance to pulse rate (Patle, et al. 2022).

Kim, Chae and Nishigaki developed a method of compensating for air content present in soil pores using ethanol injection. This ethanol displaced air in samples and FDR measurements were taken at a frequency of 1 GHz. The method presented allows for the estimation of effective and physical porosities in saturated soils by calculation of total permittivity estimates from known permittivity values of soil component materials and the ratios of these materials in the sample (Kim, Chae and Nishigaki 2008).

Finlay and Howard iteratively developed prototypes of 1, 3, and 36 row crop sowing machines featuring a semi-autonomous real-time depth control system implemented with hydraulic actuators and using an array of soil moisture sensors to provide system feedback. Field trials were performed across multiple growing seasons beginning with the single tine prototype. This design was trailer mounted and towed by a utility vehicle. The trial tested various sensor types and helped to refine the hydraulic control system. A major limitation of this trial was that the single row rendered concurrent testing of multiple sensors impossible. The 3-tine prototype was mounted on a small agricultural tractor. In this trial the hydraulic system was supplied by the tractor. The higher tine count allowed for concurrent testing of multiple sensors, but increased the actuation system complexity significantly as actuators also had to be controlled concurrently. Pressure and load sensors were incorporated to provide data of forces in tines at variable tillage depths. The latest trial occurred in 2023 with the 36-row design. The 36 sowing tines were mounted on a 12-meter frame for full-scale testing of the system. The parallel compute requirements due to the high tine count made control software a challenge. Objectives of the project in 2024 include implementing system control over ISOBUS, further in-field trials and the development of a new sensor to improve accuracy and wear resistance (Finlay and Howard 2024).

Sulek and Ogorkiewicz analysed the effects of sowing depth and seed size on germination quality and harvest yield of wheat plants. Sowing depths of 1 cm, 3 cm, 5 cm, and 7 cm and seed size classes of small (1.8-2.2 mm), medium (2.2-2.5 mm), and large ( $>2.5$  mm) were evaluated on germination time and germination percentage. Results showed higher germination rates with the large seed group, the 5 cm and 7 cm deep sowing delayed germination and reduced germination rate, and the optimal group was the large seed with 3 cm sowing depth (Sulek and Ogorkiewicz 2020).

Rego Segundo et al presented a method of approximating complex permittivity using a current-to-voltage conversion circuit and dual frequency amplitude measurement. This method had the benefit of not requiring phase measurement of signals, leading to lower component speed requirements and lower complexity of circuits compared to the traditional method of measuring both amplitude and phase of signals. Results demonstrated maximum error of 0.6% for electrical conductivity measurement and maximum error of 2% for relative permittivity measurement (Rêgo Segundo, et al. 2019).

With a low cost of construction, real-time sensing capability, and no requirement for direct contact between sensing electrodes and the MUT, capacitive sensing was identified as an applicable sensing pathway. The review identified coplanar capacitor designs used in capacitive sensors could be classified into CPC and IDC designs. The method of switching sensing domains by switching between low and high frequencies presented by Escriba et al could enable real-time measurement of both permittivity and ionic characteristics of the soil profile with the type of sensor array proposed for this work. Finally, the method of complex permittivity characterization presented by Rego Segundo et al was recognized as an approach which could benefit the accuracy and economics of a sensor array design.

### 3. Background

#### 3.1 Crop Establishment and Sowing Time

Sowing time and quality of seedling establishment have a large influence on the yield outcomes of cereal crops and is a critical decision-making point in a season for agricultural business. Seed can be wet sown, where it will begin growing immediately, or dry sown, where it will lay dormant in the soil until a rainfall event. Wet sowing refers to placing the seed at a depth in the soil profile with enough moisture to begin germination, it can still be performed when the surface layers of the soil are dry. Sowing using this method can accelerate emergence times (GRDC 2016), lead to better establishment rates and provide better control of weed species from knockdown and pre-emergent herbicide applications. With the large scale of many Australian cropping operations, it is often not possible to use this method over an entire program, and waiting for rain before sowing is often not an option. To cover the large areas involved, dry sowing a percentage of a cropping program with long season cereal varieties is a common practice. These crops will begin growing with the opening rains of a season, but these areas must be prepared in advance to ensure weed seed burdens are low as the use of knockdown herbicides is not possible (Congreve 2022).

A seed will start germinating when 35-45% of its dry weight in moisture has been absorbed. Proteins and starch in the seed are converted by enzymes into sugars for energy, and the radicle, seminal roots and coleoptile emerge from the seed (GRDC 2016). The coleoptile is vital to the successful emergence of the seedling. This structure encases the first leaves to protect them from damage, it elongates as it pushes through the soil, guiding them to the surface. On reaching the surface the leaves emerge from the tip of the coleoptile and the seedling can begin acquiring energy through photosynthesis (Oregon State University 2024).

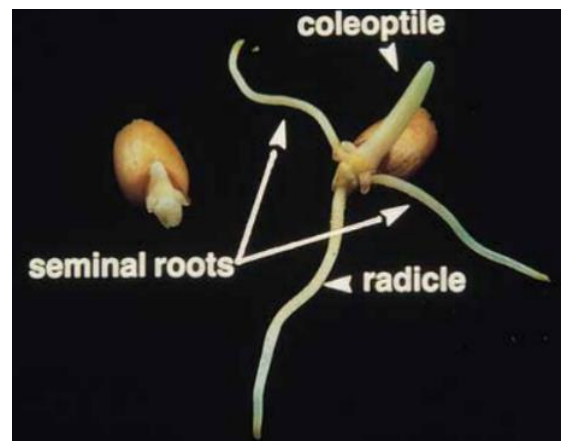


Figure 1: Wheat seed during germination. From: (GRDC 2016).

Seed size can have a large impact on the success of crop emergence. Until photosynthesis begins, the only energy the seedling can access comes from the starch in the seed. Zareian et al compared sizes of wheat seeds for germination and emergence rates. They found that although seed size had little impact on germination, it had a large impact on emergence rates, with the 2-2.2 mm seed group having an emergence rate of 67.95% compared to the 2.8-3 mm group at 80.55% (Zareian, et al. 2013).

The coleoptile length of a cereal crop species can vary greatly between varieties and is a major factor in the ability of seed to emerge for depth. Pumpa et al suggest a sowing depth which exceeds the coleoptile length of the variety can result in poor crop establishment due to shoots emerging from the coleoptile below the ground surface (Pumpa, et al. 2013). Appendix A shows a table of wheat varieties and the results from a 2021 field trial which compared coleoptile length, sowing depth, and yield of several wheat varieties.

### **3.2 Moisture Seeking to Optimize Crop Emergence**

Moisture seeking refers to the implementation of strategies to conserve pre-sowing soil moisture allowing crops to be wet sown into a layer of the soil profile where the germination and emergence process will begin straight after sowing. Strategies to conserve soil moisture include minimizing soil tillage to avoid losses from evaporation and removing weed species over the summer period with knockdown herbicides. During planting, sowing depth is adjusted to place seed at a high moisture point in the soil profile. Recent wheat breeding research conducted by the CSIRO has focussed on creating longer coleoptile crop varieties capable of emerging from deeper in the soil profile. Field trials on two new wheat varieties (Mac and Mace 18) successfully emerged from a sowing depth of 120 mm (GRDC 2024). Commercial release of varieties with these traits could vastly increase the opportunity for growers to take advantage of moisture seeking practices to optimize crop yields.

### **3.3 Nil-till and No-till Sowing Systems**

The dominant broad-acre crop sowing method in Australia is based on a system referred to in the industry as “minimum-till”, “nil-till” or “no-till”, with 74% of Australian cereal crops sown using this method as of 2016 (Llewellyn and Ouzman 2020). This system has largely replaced traditional aggressive tillage methods, where tillage points were designed to till wide and shallow to remove weed plants in front of seed placement. In contrast, the minimum-till system uses long (150-250 mm), thin (~15 mm) tillage points to penetrate soil layers below the sowing depth (Ausplow 2024). The major benefits of this system over the traditional method are to increase the control of seed and fertilizer placement in the soil profile below, to minimize the loss of soil moisture caused by the tilling process, and to optimize the outcomes of Trifluralin based pre-emergent herbicide application.

Figure 2 shows an implementation of a minimum-till sowing system. The tilling point cuts a narrow, deep slot into the soil profile. Behind the tilling point is a fertilizer dropper where solid or liquid fertilizers are dropped into the slot at depth and soil is then allowed to backfill the slot. Next, the opening tool re-opens the top portion of the slot at a pre-set sowing depth and seed is placed at this depth through a seed dropper. Sowing depth can be adjusted by vertical adjustment of this opening tool; however, this cannot be done in real-time as it requires the adjustment of mechanical fasteners as illustrated by the 2 adjustment bolts in figure 2. Finally, a press wheel compresses the soil directly over the seed. Changes in local soil height are compensated for by connecting the entire seed placement assembly to the main assembly through a spring-loaded hinge which rides on the press wheel as the local soil height changes.

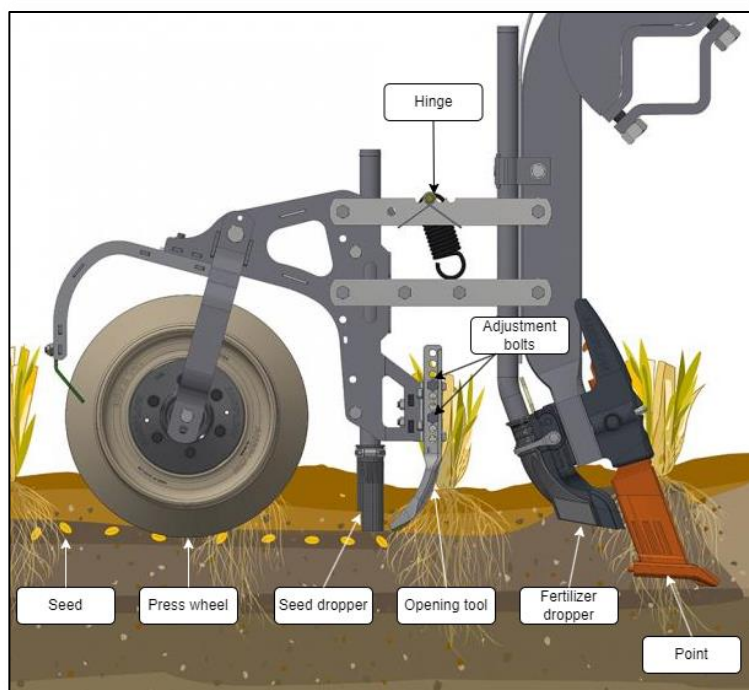


Figure 2: Diagram of "Nil-Till" sowing system. From: (Ausplow 2024).

### 3.4 Constraints of the Sensing Environment

The sensing environment of this application presents significant design challenges. The sensor array must be located below the soil surface in contact with the soil between the tillage point and the opening tool in figure 2 to provide the required readings. This environment is extremely abrasive, mechanically aggressive, and crop fertilizers being applied to this zone can be highly corrosive. A successful design must be capable of accurate and reliable measurement while providing an acceptable operational lifetime in this environment and being economically viable.

### 3.5 Capacitive Sensors in Moisture Sensing

In electrical circuits, a capacitor is a component which can store electrical energy over time. The most common type of capacitor is the parallel plate capacitor (PPC), where electrodes are conductive plates on parallel planes with area  $A$ , separated by a dielectric of thickness  $d$  and permittivity  $\epsilon$  (figure 3). A voltage at the plates causes the charges  $+Q$  and  $-Q$  to accumulate opposing charges in the dielectric at the surface of the plates. This polarization generates an electric field in the dielectric. Capacitance is a measure of the ability of a capacitor to store electric charge:

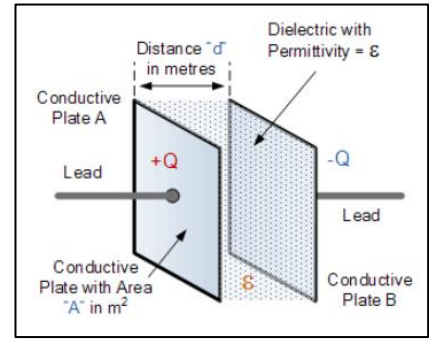


Figure 3: Parallel Plate Capacitor  
From: (Electronics Tutorials 2024).

$$C = \frac{Q}{V} \quad (1)$$

Which for a PPC can be approximated by:

$$C = \epsilon \frac{A}{d} = \epsilon_0 \epsilon_r \frac{A}{d} \quad (2)$$

This approximation requires that  $d$  is small and is uniform at every point over the area  $A$ . This simplifies the above calculation by allowing the electric field to be treated as a uniform electric field with force vectors perpendicular to the plate surfaces at all points of  $A$ . In this case, the force vectors which extend out beyond the edge of the plates (figure 4) can be considered insignificant. This protrusion of the field from the edges of the capacitor is known as a fringing field.

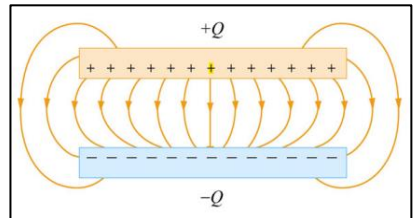


Figure 4: Electric Field of Parallel Plate Capacitor From: (MIT n.d.)

For sensing applications, the dielectric of a capacitor is replaced with the MUT and a  $\Delta\epsilon$  of the MUT results in a  $\Delta C$  of the capacitor. A PPC arrangement requires the MUT to be placed between the electrodes which limits the sensing domains of PPC sensors. CPCs overcome this limitation by rearranging the plates from a parallel (Figure 5, Left) to a coplanar layout (Figure 5, Right).

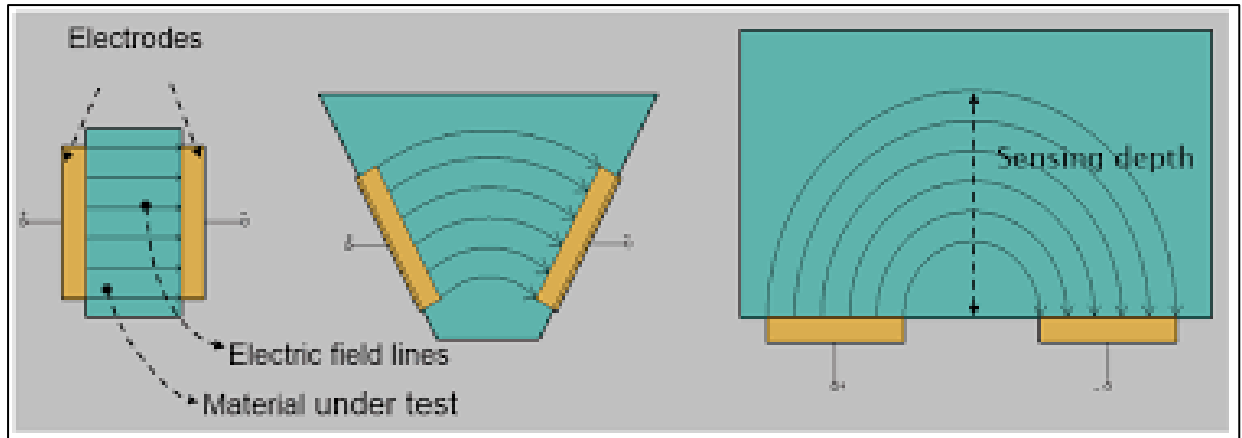


Figure 5: Transformation from Parallel Plate (Left) to Coplanar (Right) Capacitor From: (Yang, et al. 2015).

This change also transforms the electric field from being primarily uniform to being primarily a fringing field. Switching to a fringing field makes the modelling of CPC capacitance a greater challenge compared to the PPC case. The geometric parameters of a CPC are the electrode width  $w$ , the gap width  $g$ , the electrode length  $L$ , the electrode height  $h$ , and the depth of the field  $T$ . Claudel et al suggest the following model can reliably approximate CPC capacitance, providing  $L \gg w$  and  $\frac{w}{g} \gg 1$  (Claudel, et al. 2021):

$$C = \frac{2\epsilon_0\epsilon_r L}{\pi} \ln \left[ \sqrt{\left(1 + \frac{2w}{g}\right)^2 - 1} + \left(1 + \frac{2w}{g}\right) \right] \quad (3)$$

Important factors for CPC designs are the minimisation of parasitic capacitance and directing of the fringing field. The electrode height  $h$  creates a PPC-like arrangement across the gap between the electrodes. Minimizing  $h$  results in a minimal value of  $A$  in equation 2, which minimizes this parasitic capacitance. Figure 6 demonstrates the use of ground planes for directing the fringing field into the MUT. The CPC with no ground plane (Figure 6, left) emits fields from both sides of the electrodes. If the intention of such a design is for the MUT to be placed only on one side of the sensor, a large percentage of the total field is not in the MUT, only contributing noise to the output signal. By placing a ground plane below the excitation electrode (Figure 6, right) the noise in the output signal is replaced with a constant parasitic capacitance through the substrate.

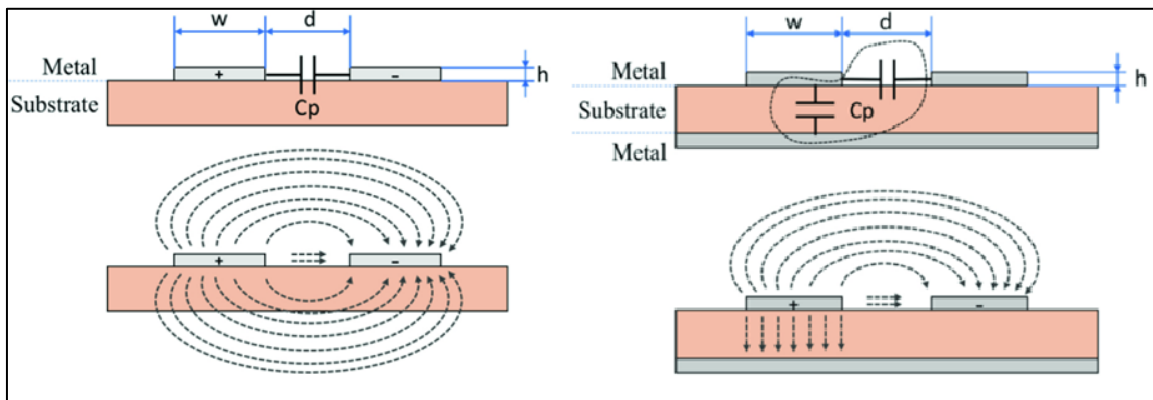


Figure 6: Coplanar Capacitor (Left) and Coplanar Capacitor with Ground Plane (Right) From: (Bodini, et al. 2018).

The method presented by Patle et al of mirroring electrodes of the same charge on both sides of a PCB is a more optimized field directing technique which can be implemented in double

sided sensing applications. Excitation electrodes are mirrored on both sides of the PCB and the repulsive force between them reduces the parasitic capacitance in the substrate and directs the fields into the MUT on either side. Patle et al demonstrated a tripling of usable capacitance with this method in a comparison with earlier works (Patle, et al. 2022).

IDC sensors are a subset of CPC sensors with electrodes consisting of sets of interleaved fingers (figure 7). By surrounding the perimeter of fingers of one electrode with those of the other, IDCs can have advantages over CPCs. This arrangement can provide much higher capacitance for a given area. The geometric parameters of gap width, electrode width, and periodicity  $\lambda$  can also be tuned to optimize the field penetration depth.

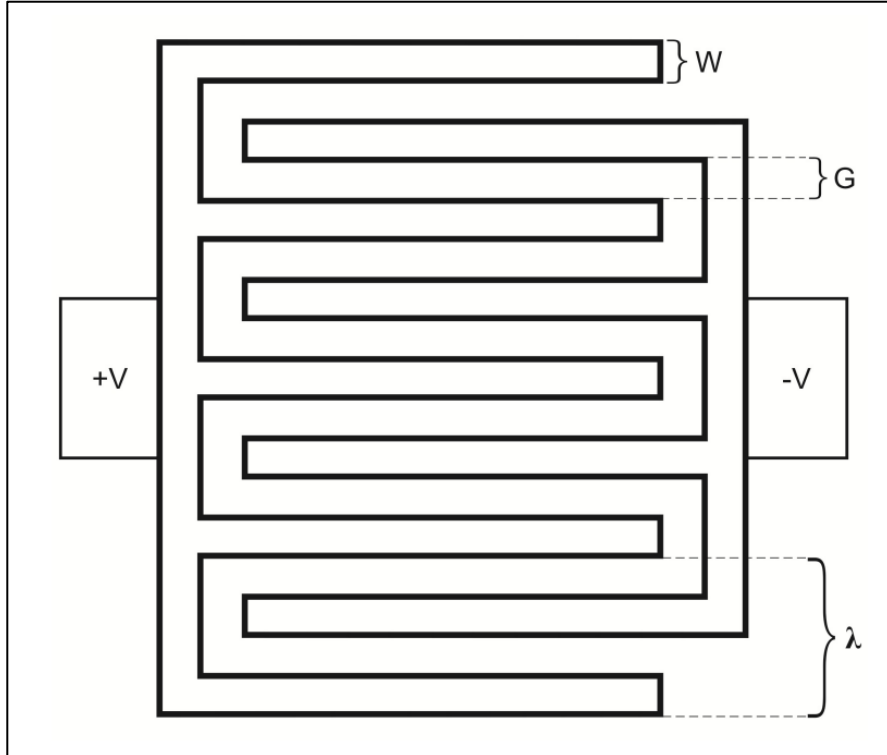


Figure 7: Diagram of IDC. From: (González, et al. 2015).

### 3.6 Challenges in Soil Moisture Sensing

Calibration of capacitive soil moisture sensors is normally required to suit the soil at the installation site to provide accurate output. This project requires calibration to be performed autonomously in real-time. Soil parameters such as ionic content, conductivity, pH, carbon content, void density, and texture can change over short distances and the permittivity of the MUT will change with these factors. This will require advanced control system algorithms and possibly additional perception pipelines to be implemented in the future, but in the design phase of the project it is critical that as much reliable data can be provided from the sensor array as possible. Soil texture is a measure of the sand, silt and clay particles present in soil and can be used to broadly classify soil types as seen in the soil triangle diagram below (Queensland Government 2024).

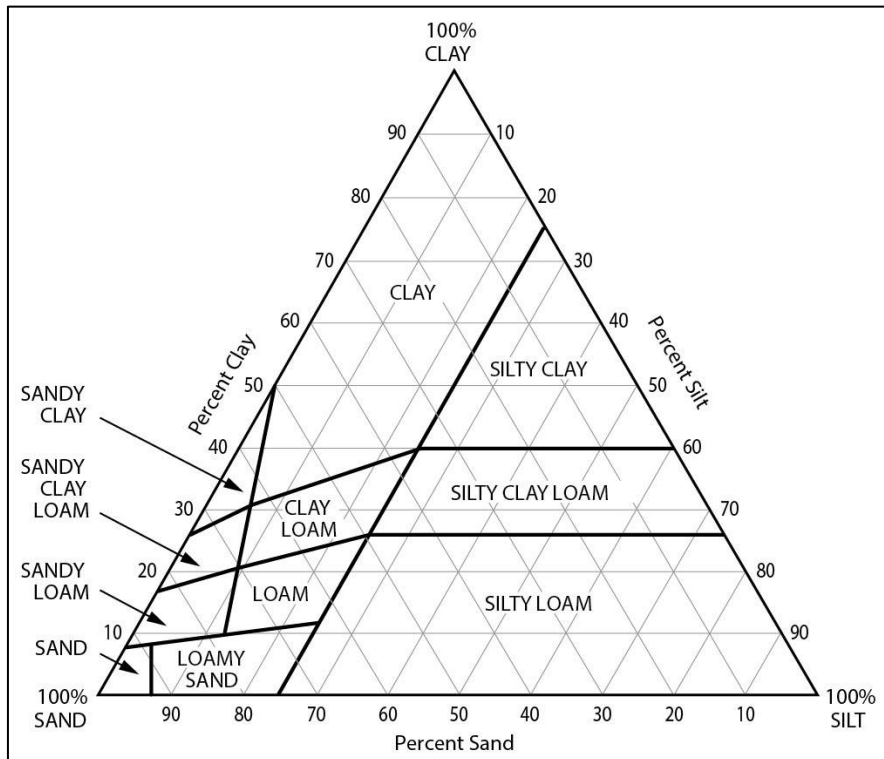


Figure 8: Soil Texture Triangle (Queensland Government 2024).

For materials with isotropic dielectric properties,  $\epsilon$  is a complex number (Li, Wu and Shen 2022) with real and imaginary components:

$$\epsilon = \epsilon' - j\epsilon'' \quad (4)$$

$$\text{where } j = \sqrt{-1} \quad (5)$$

$\epsilon$  is also frequency dependant and can be represented as a function of the angular frequency  $\omega$  of the input signal:

$$\epsilon(\omega) = \epsilon'(\omega) - j\epsilon''(\omega) \quad (6)$$

$$\text{where } \omega = 2\pi f \quad (7)$$

Figure 9 from Li et al shows the magnitudes of the  $\epsilon'$  and  $\epsilon''$  components of  $\epsilon$  for water as function of frequency.

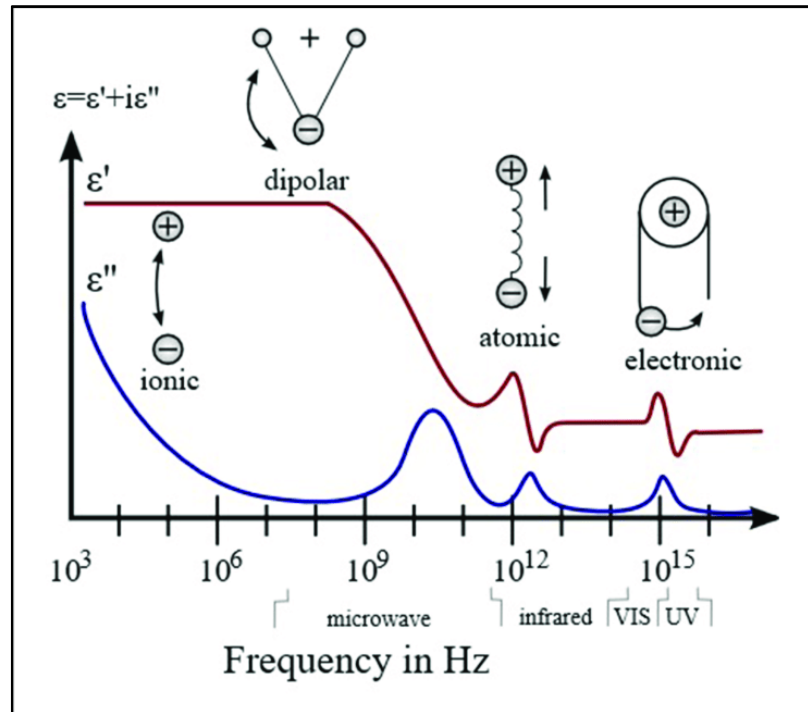


Figure 9: Complex Permittivity of Water as a Function of Frequency (Li, et al. 2019).

Figure 10 shows the same relationship for a mixture of water and kaolinite clay and demonstrates that the addition of the clay component has a large effect on the real and imaginary components of  $\epsilon$  (Dong and Wang 2008). This variation in response presents a significant challenge to characterization of soil moisture across soil types with variable levels of clay content.

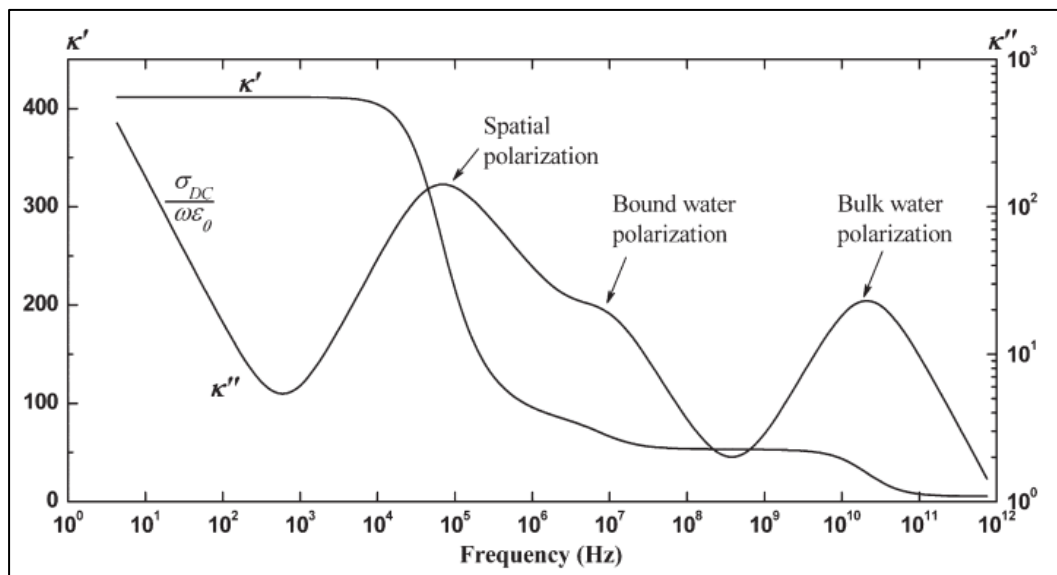


Figure 10: Complex Permittivity of Water and Kaolinite Clay Mixtures (Dong and Wang 2008).

In addition to the polarization effects present in figure 10, the clay and silt components of soil texture also alter the soil porosity  $\eta$ , as can be seen in figure 11 .

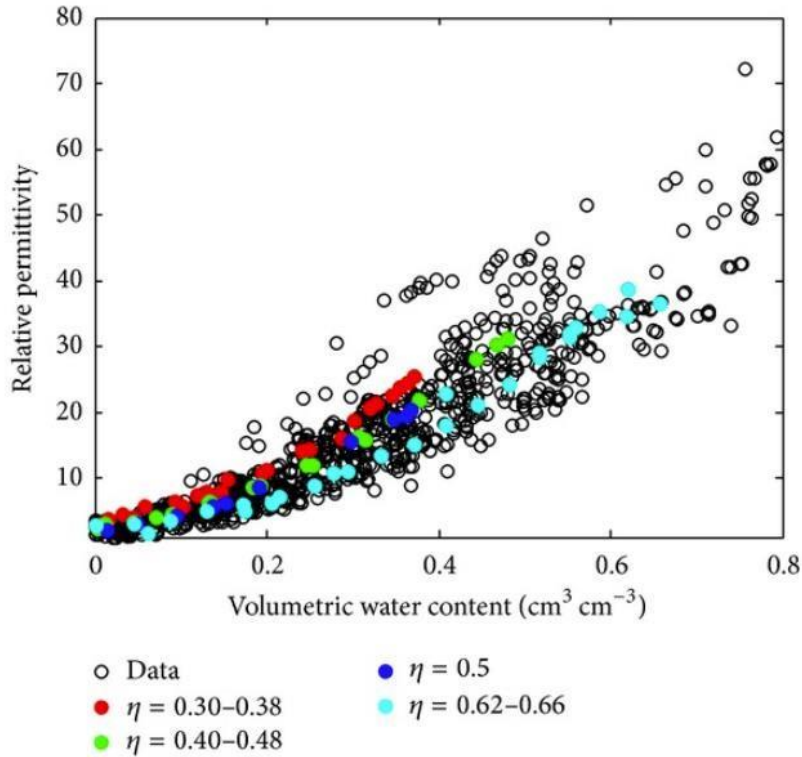


Figure 11: Relative Permittivity vs VMC at Variable Soil Porosities (Mukhlisin and Saputra 2013).

The complex permittivity can be used to classify the field propagation and dielectric properties of materials:

$$\text{Dielectric Class}(\boldsymbol{\varepsilon}) = \begin{cases} \text{Lossless, perfect dielectric, } \varepsilon''/\varepsilon' = 0 \\ \text{Low - loss, good dielectric, } \varepsilon''/\varepsilon' \ll 1 \\ \text{Lossy propergation medium, } \varepsilon''/\varepsilon' \approx 1 \\ \text{High - loss, poor dielectric, } \varepsilon''/\varepsilon' \gg 1 \\ \text{Perfect conductor, } \varepsilon''/\varepsilon' \rightarrow \infty \end{cases} \quad (8)$$

The method proposed by Rego Segundo et al suggests the following approach for real-time measurement of complex permittivity. For sub-GHz excitation frequencies, relaxation effects of the real component of complex permittivity can be neglected (as seen in figure 8) and  $\boldsymbol{\varepsilon}_r$  can be modelled as:

$$\boldsymbol{\varepsilon}_r = \varepsilon_r' - j \frac{\sigma}{\omega \varepsilon_0} \quad (9)$$

Where  $\sigma$  is the electric conductivity in siemens per meter (Rêgo Segundo, et al. 2019), and the complex admittance  $\mathbf{Y}$  can be approximated with:

$$\mathbf{Y} = j\omega k_g \varepsilon_0 \boldsymbol{\varepsilon}_r \quad (10)$$

Where  $k_g$  is the geometric configuration constant of the sensor (Rêgo Segundo, et al. 2019), i.e. for the simple PPC case in equation 2,  $k_g = \frac{A}{d}$ . A full derivation of this method can be seen in Appendix B.

This method uses a similar dual frequency approach to the one presented by Escriba et al to measure conductivity at a lower frequency and permittivity at a higher frequency, enabling both components of the complex permittivity to be characterized without the need for the high-speed circuits required for phase measurement. It is highly likely a characterization of both components would greatly improve the soil type classification outcomes of a control system for this work.

## **4. Design and Development of Sensing Prototypes**

### ***4.1 Investigation and Initial Design Development***

The literature review highlighted several aspects that were critical to the viability of the project, so as a first step an investigation phase was performed to gain some insight into this sensing domain. The three main unresolved questions after review of the literature were:

1. How could a design deal with the constraints presented by this sensing environment.
2. Would CPC or IDC designs be more suitable for this use-case.
3. Which capacitive sensor optimization pathways would have the greatest positive impact on functionality in this sensing domain.

This section details the preliminary work performed during this investigation phase and the initial design developed from the results this phase provided.

#### ***4.1.1 Dealing with the Sensing Environment***

The primary concern at the beginning of this project was developing a design capable of providing reliable operation in this sensing environment. The combination of the electromagnetic properties required for capacitive sensing and the mechanical constraints placed on a design by this sensing domain would require some form of mechanical shield to be placed over the sensing electrodes to protect the sensors from the highly abrasive environment, while also allowing transmission of the sensing signal through the MUT with attenuation levels low enough that effective sensing can still be achieved reliably. Materials with properties that satisfy both aspects of the requirement list are somewhat specialized. The shield material cannot be metallic as fringing fields would be negated by a metal. Polymers are commonly used for shielding of sensing elements in soil moisture applications, as was the case in Escriba et al, but it is highly unlikely a polymer could provide the wear resistance this use-case demands. This left ceramics as the most likely class of material to satisfy the design requirements.

Research into the properties of suitable ceramics identified high purity alumina (HPA) as a material that could be capable of meeting the electrical, mechanical, and economic requirements of this shield layer. HPA ceramic is highly resistant to abrasion and mechanical wear, finding widespread industrial use in wear plate and liner applications (China Alumina Ceramic 2022) and is highly resistant to chemical corrosion. Available grades of alumina have a dielectric constant ( $\epsilon'$ ) value between 9 and 10 at low frequencies which, while certainly not ideal, was hypothesized to be low enough to allow a functional sensor design to be achieved. This material also finds widespread use as an insulating substrate material for electronic applications and was commonly available as premade substrates of variable thickness in purities from 96% to >99%. Substrates of 0.5mm, 1 mm and 2 mm were purchased for testing. A table of the material properties for various grades of alumina can found in Appendix C.

Once this method of environmental shielding was identified, an initial design layout was developed for use in testing (figure 12). This layout consists of a printed circuit board with sensing elements implemented with copper traces on the outside copper layer of a PCB. Over these traces an  $Al_2O_3$  substrate is installed so the bottom face of the substrate is in contact with the sensing electrodes. This layout requires the fringing fields of the sensor to penetrate the shield layer while sensing, this will likely attenuate the sensing signal of sensors considerably. These electromagnetic aspects of the design are the focus of this work. It should be noted that assessing the ability of the design to withstand the mechanical constraints of the sensing

environment unfortunately fell outside the scope of this work, but these aspects are critical to design functionality and are the suggested priority for future work.

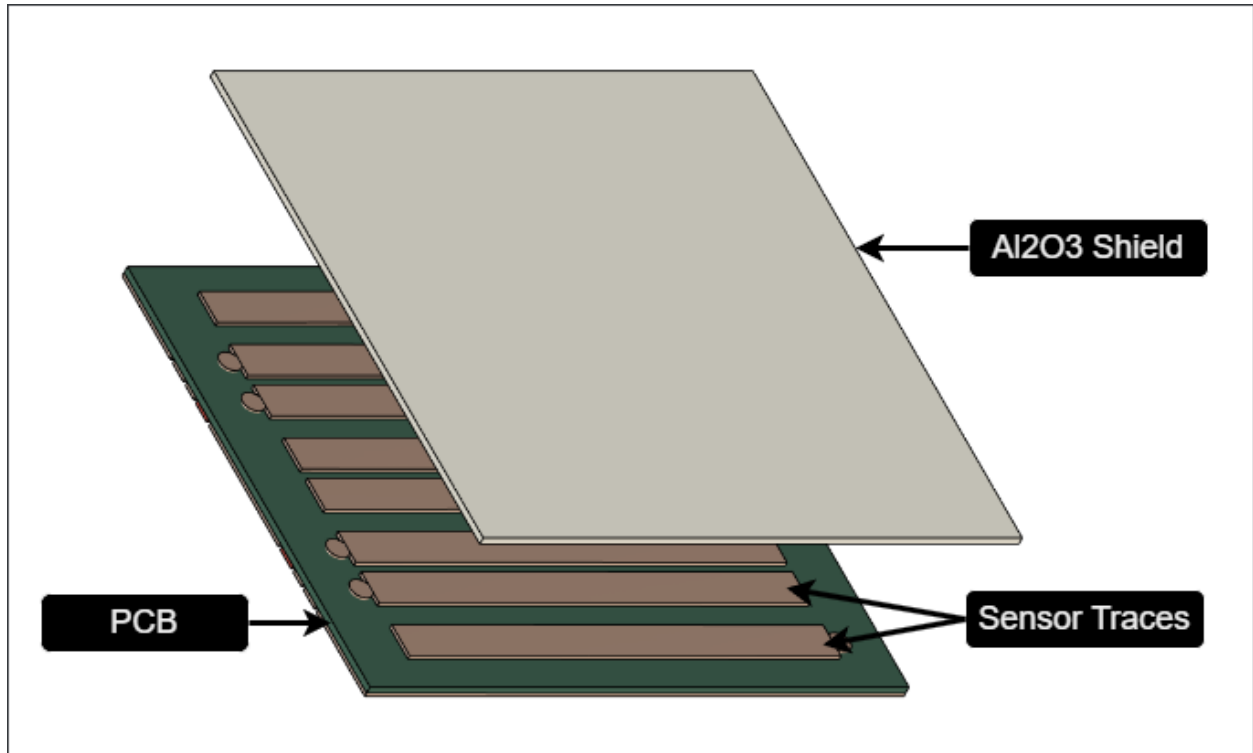


*Figure 12: Initial Design Layout of Sensor Array.*

#### 4.1.2 Comparison of Commercially Available CPC and IDC Sensors

The literature review identified CPC and IDC designs were used for soil moisture applications, but a direct comparison between them was not found. Commercially available sensors of both CPC and IDC designs were sourced during this phase of the project for experimental comparison. The first sensor was a Radiocontrolli RC-SPC1K capacitive rain sensor featuring a high digit count, low digit width IDC sensing element on one face of a thick-film substrate of alumina. The sensing element is covered with a thin blue polymer layer which keeps the sensing element electrically isolated from the MUT. The data sheet states a minimum capacitance of 100pF when completely dry and a maximum capacitance of >550pF when completely wet (Radiocontrolli n.d.). This sensor was designed to measure rain, but output depends on permittivity of the sample, thus it can also function as a soil moisture sensor. The primary reasons for selecting this sensor for testing were the IDC layout, high capacitance, and thick-film alumina ceramic construction. The sensor was waterproofed to enable complete submersion in liquid samples by 3D printing a small mounting frame and filling the frame with epoxy resin.

The second sensor was a Grow soil moisture sensor featuring mirrored CPC sensing elements constructed on the inner 2 layers of a 4-layer FR4 PCB. The sensor uses a 555-timer IC to generate the excitation signal and outputs a frequency which varies with  $\epsilon$  of the MUT. The 555-timer circuit was disconnected from the sensing elements by severing the PCB traces so input and output signal wires could be soldered directly to the electrode pads. The construction

technique of this sensor ensures the sensing elements are electrically isolated from the MUT, so no further waterproofing was required.

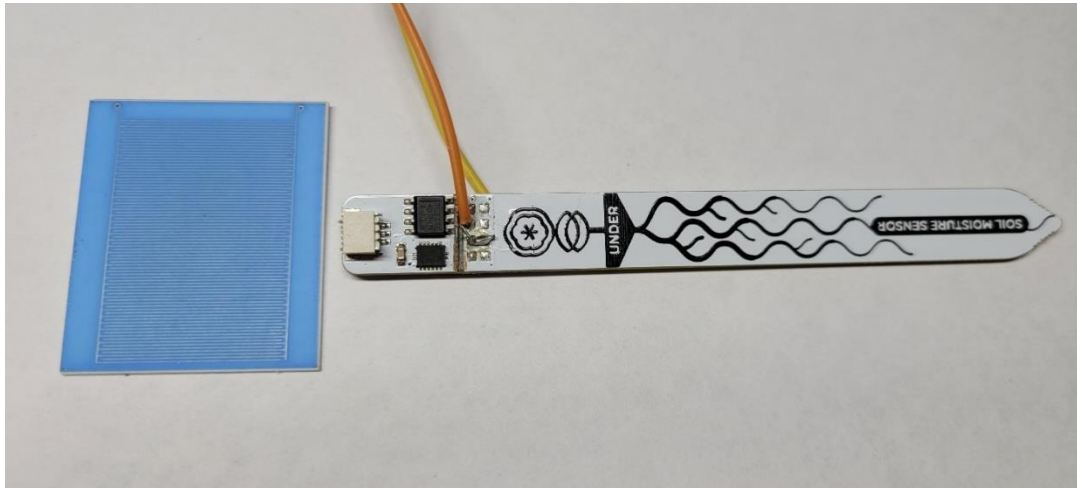


Figure 13: Radiocontroli IDC Sensor (left) and Grow CPC Sensor (right).

#### 4.1.3 Frequency Analysis

Frequency analysis was performed on both sensors to visualize the effects of  $\epsilon_r'$  and  $\epsilon_r''$  over a bandwidth of 1kHz to 120MHz. A Siglent SDS1204 X-E 200MHz oscilloscope and SDG2122X 120MHz signal generator were connected over USB to allow NI-VISA commands sent from the oscilloscope to control the generator. 50  $\Omega$  coaxial cables of equal length were connected from both outputs of the generator to a multi-channel SMA test fixture with the configuration seen in figure 13. Two 50  $\Omega$  feed-through terminations were used at oscilloscope inputs 1 and 3 to match the input impedance of the generator. Channel 2 of the signal generator was then slaved to channel 1 and the Bode plot function was setup for a frequency sweep from 1kHz to 120MHz with a 1 V<sub>pp</sub> AC sin wave input. This configuration uses the input at channel 1 of the oscilloscope as a reference signal to generate the magnitude and phase plots of the input on channel 3.

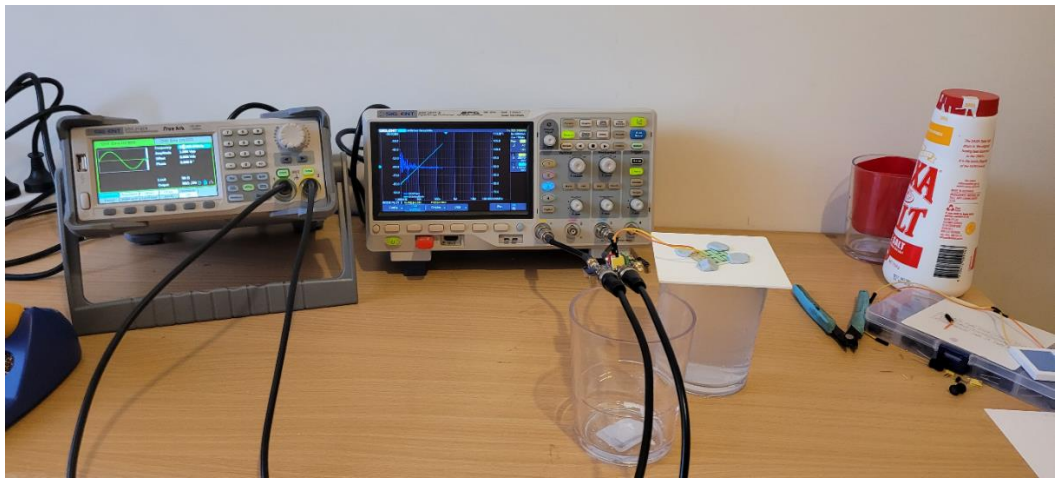


Figure 14: Apparatus used for frequency analysis.

In the circuit used for frequency analysis the capacitive sensor and the 50 Ohm termination resistor form an RC high pass filter. The cut-off frequency  $f_{cutoff}$  of this filter varies with  $\Delta\epsilon$  of the MUT.

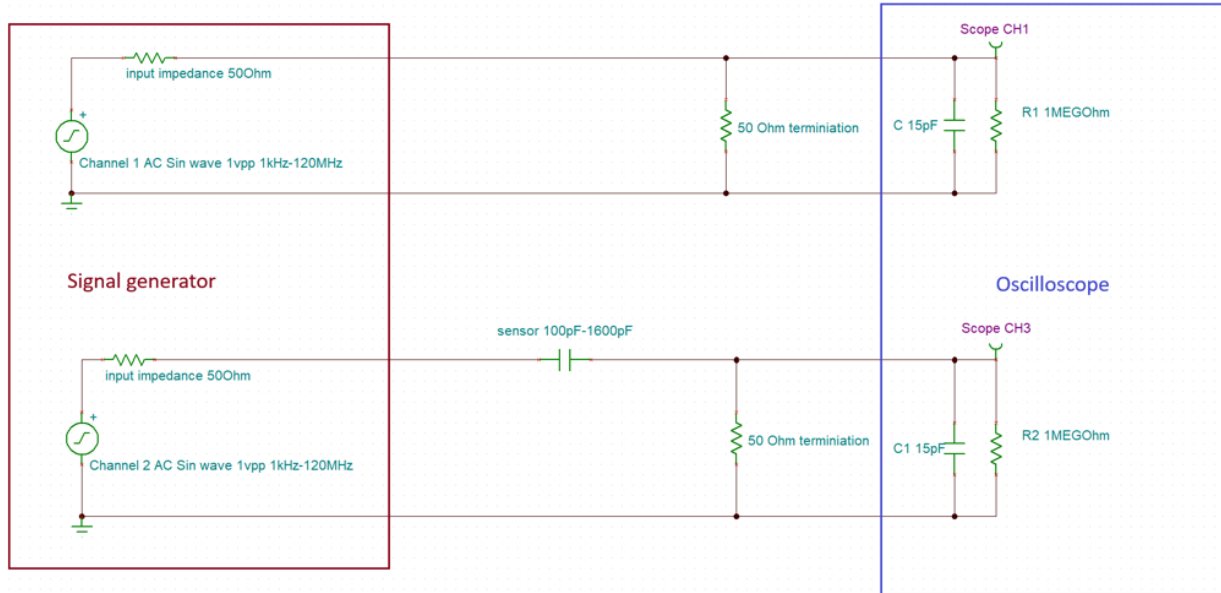
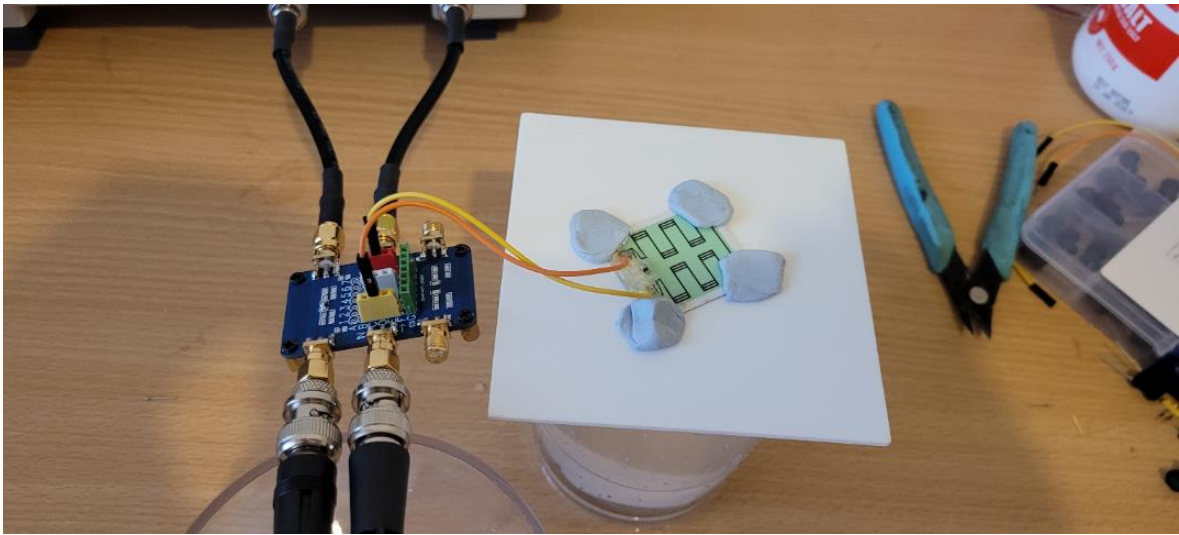


Figure 15: Circuit used for frequency analysis.

Frequency analysis examined the effects of both the change in the relative permittivity and the change in the ionic content by combining the data from the same test performed on 2 separate test groups. To examine the frequency response over a range of  $\epsilon_r$  values, samples of distilled water ( $\epsilon_r \approx 80$ ), methylated spirits ( $\epsilon_r \approx 25$ ), canola oil ( $\epsilon_r \approx 3$ ) and air ( $\epsilon_r \approx 1$ ) were measured. This group is collectively referred to as the permittivity group. The ionic effects were examined using solutions of distilled water and 0.25%, 0.5%, 1% and 1.5% NaCl by volume, this group is collectively referred to as the ionic group.

#### 4.1.4 Substrate Penetration

To assess the ability of the sensors to penetrate the mechanical shield the sensors were attached to a 96% pure  $Al_2O_3$  substrate of 1 mm thickness with the sensing element face down. Substrates were then slid through the meniscus of distilled water samples filled above the rim of the sample cup, so the bottom face of the substrate was in contact with the sample. The frequency sweep process was then repeated in this configuration and results were plotted against the previous readings for air and distilled water submersion.



*Figure 16: Substrate penetration testing setup.*

## 4.2 Design Optimization

The constraints placed on the sensor array by this sensing environment are so severe that it is unlikely an iterative design approach would be effective for this application and software modelling would likely be far more effective for this case. The literature review identified a commonly used method of software modelling for soil moisture sensors was via finite element analysis (FEA) using the COMSOL Multiphysics electrostatics software suite. After discussion with an Australian distributor of the software, access to a 1-month trial version of COMSOL was granted to carry out this modelling. The modelling examined several design parameters to assess the performance of sensor optimization methods.

### 4.2.1 Design Parameters Examined

First several IDC designs were simulated to allow comparison against CPC designs. This was performed as a means of verifying the conclusion of the commercial sensor analysis that CPC designs were more suited to this use-case than IDC designs. During this phase of the modelling the interactions of the fringing fields with the alumina substrate and MUT was also examined to gain some insight into these relationships. Single and dual sided configurations were modelled to assess if the electrode mirroring optimization technique described by Patle et al could be a suitable optimization pathway for this design (Patle, et al. 2022). Single sided designs had a single  $Al_2O_3$  shield covering the sensor side of the PCB with the other side covered completely with a ground plane copper layer at ground potential, while double sided designs had 2 identical  $Al_2O_3$  shields covering the electrodes on both sides of the PCB. These results were compared against the effect of doubling the length of the sensor from 40 mm to 80 mm.

### 4.2.2 Device Under Test Layout

The sensor array detailed in this work has several features that required this modelling to be performed with an approach which differs from many of the approaches found in the literature. The soil depth resolution required for this use-case was set at 10 mm after discussion with industry stakeholders. This requirement places a hard upper bound on the width of individual sensor footprints of less than 10mm. To optimize sensor capacitance within this available area, the sensors in the array must be in very close proximity to each other, with an inter-sensor gap of less than 1 mm. Ensuring the fringing field is directed

through the intended slice of MUT as much as possible is required to prevent noise between these discrete soil depth slices. This will also minimize sensor to sensor noise caused by the fields extending from the input electrode of one sensor to the output electrode of another. The  $Al_2O_3$  layer this use-case requires will attenuate the sensing signal strength, likely by orders of magnitude in comparison to being in direct contact or in micron scale proximity to the MUT. This is the key parameter this optimization must focus on for a design to provide functionality in this use case.

Much of the FEA modelling found in the literature was focussed primarily on optimizing capacitance per unit area, which is one of the primary drivers of the popularity of IDC sensors in capacitive sensing domains. In this work, this parameter is secondary to minimizing signal attenuation from the  $Al_2O_3$  layer. To assess this parameter, it was essential that all modelling was performed in a model space as close as possible to the real-world situation. The approach used will be covered in depth here, as an understanding of how this modelling was performed is required for interpretation of results.

All CPC simulation results presented in tabulated form in this work were modelled as the centre sensor of an array of 5 identical sensors placed on a 1.6 mm 2-layer PCB with 35-micron top and bottom copper layers and the remainder FR-4 dielectric substrate. Model parameters for excitation voltage was set at 12 volt and permittivity of the FR-4 was set at 4.4 in line with the manufacture's specifications (JLCPCB 2024). A constant 2 mm board edge to sensor clearance was used for all simulations. A 0.5 mm thick substrate of 99% pure  $Al_2O_3$  matching the width and height of the PCB and with a real permittivity of 9.5 was then positioned in surface contact with the sensor electrodes.

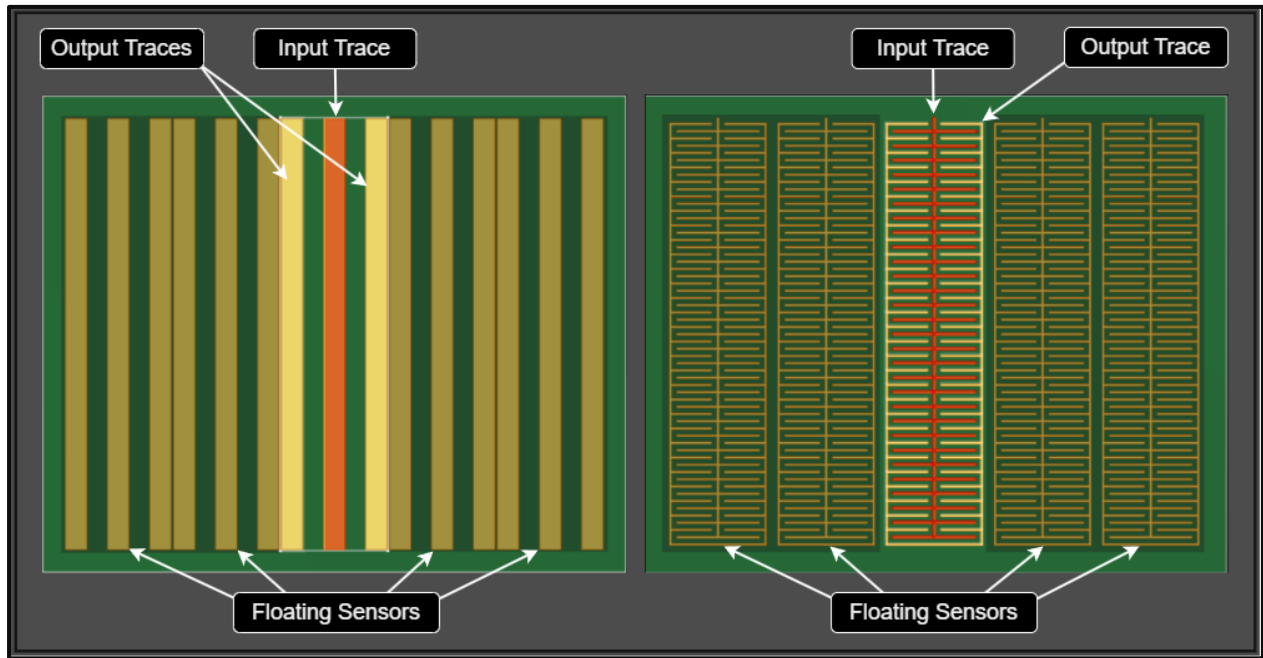


Figure 17: CPC (Left) and IDC(Right) Sensor Array Layout for FEA modelling.

The design of the signal conditioning circuit for this sensing array implements a Texas Instruments TMUX4052 analogue multiplexer to iterate through the sensors in the array. This analogue multiplexer IC contains 2 circuits in a single pole 4 throw arrangement with non-active multiplexer channels left open, not connected to ground (Texas Instruments 2024). All electrodes of the non-active sensors present in the DUT were therefore set to floating potential

for this modelling, not to ground potential, resulting in the only path to ground for the fringing field being via the output trace of the active sensor.

#### *4.2.3 Description of Modelling World*

The Comsol Multiphysics electrostatics module is setup to automatically calculate the total Maxwell capacitance, total energy and magnitude of the E-Field over the entire volume of the modelling space during each simulation. To quantify the effective electric energy and magnitude of the E-field for this use case the modelling space was further divided into 3 subdomains: upper and lower MUT domains MUT domain A and B, and a loss domain extending from the upper face of the top shield to the lower face of the bottom shield in the case of double sided designs, and from the upper face of the shield to the lower face of the ground plane in single sided designs (figure 18). By adding calculations for total energy and magnitude of the E-field in MUT domains A and B and summing the results the effective energy and magnitude of effective E-field can be quantified and compared against the total values. The material of the loss domain was kept constant and set to air for a constant permittivity value of approximately 1 for both the water and air MUT sweeps. The dimensions of the modelling world were setup to automatically scale with the dimensions of the DUT so the world boundary to DUT offsets were kept constant as the DUT geometry changed. Note in the figure below the  $Al_2O_3$  layer is set to be slightly transparent, so the sensor traces were visible throughout the modelling process.

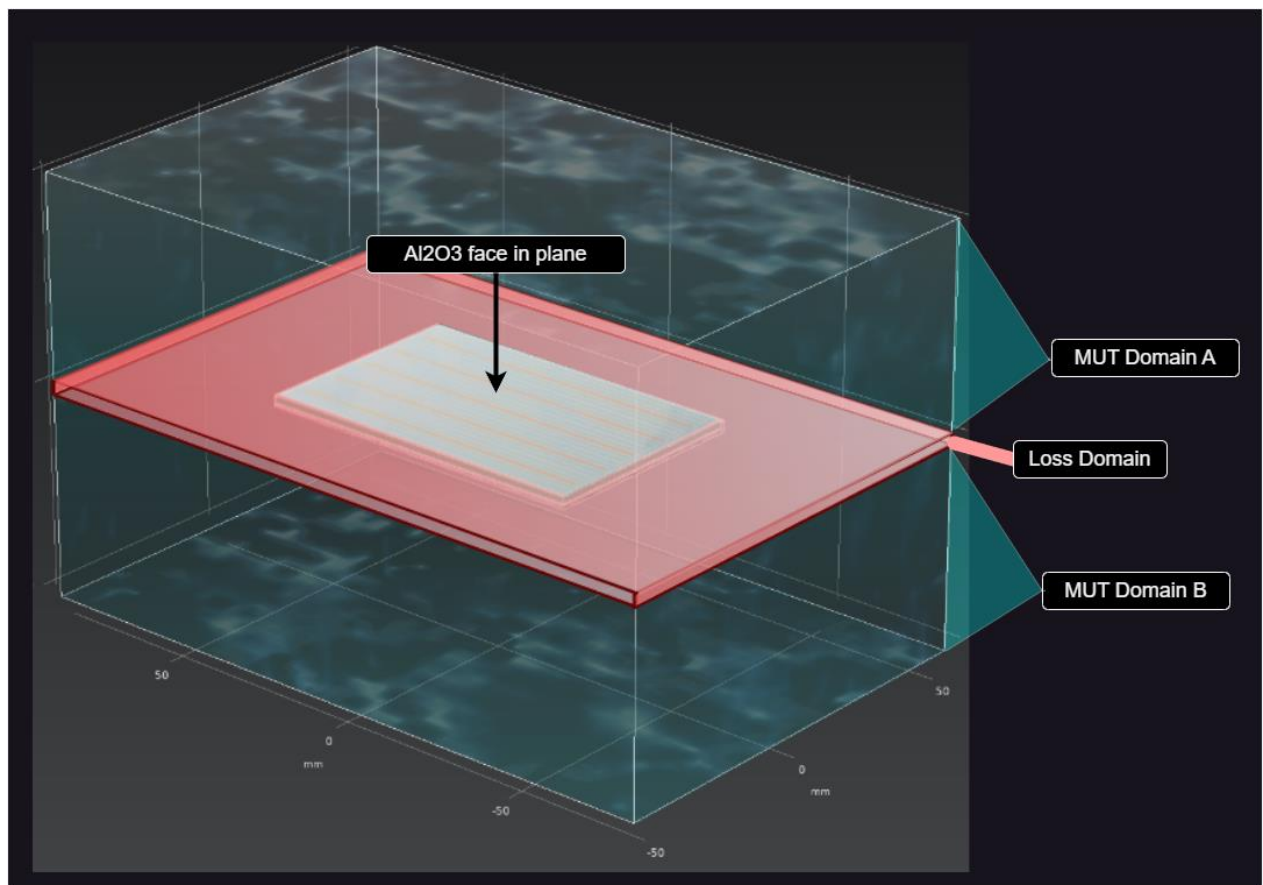


Figure 18: FEA Modelling World Diagram.

#### ***4.2.4 Optimization***

Optimization was carried out by running a parametric sweep of 2 geometric parameters of the sensing elements. For CPC designs, these 2 parameters were the width of the input and output electrodes, for IDC designs these parameters were the metallization ratio and output electrode digit count. Modelling was performed in a nested for loop, where each iteration first updates the geometry of the sensing elements in the model, then runs an electrostatics study with parameters kept constant throughout all sweeps. This process is performed for all combinations of the 2 geometric parameters and run twice on each design to create data series for the MUT domains set to both air and water.

#### ***4.2.5 Design Selection***

The final step of this modelling phase was to select a design to fabricate for further testing. Selection was carried out by examining the results of the parametric sweeps while considering the minimum capacitance value of the sensor designs.

### ***4.3 Prototype Fabrication***

#### ***4.3.1 PCB Design***

Once a design had been selected from the modelling phase a 2D CAD file of the sensor trace footprint was exported from Comsol Multiphysics and imported into the KiCad PCB design software suite so it could be used to create custom footprints for the sensor traces. These footprints were then used in the design of the PCB for a 4-sensor array.

#### ***4.3.2 PCB Fabrication***

On completion of the PCB design phase Gerber build files were generated for the design and physical PCBs were ordered from JLCPCB, a low-cost PCB manufacturer based in China.

#### ***4.3.3 Prototype Validation***

The final stage of the prototype fabrication stage of the project was to validate that the design was functional once the PCBs were received. To evaluate functionality the frequency analysis process described in section 4.1.3 of this report was re-run on one of the prototype PCBs and the results were used to verify basic functionality of the prototype.

### ***4.4 Frequency Analysis of Prototype***

This phase of the experiment was performed before characterization. The purpose of this phase was to generate bode plots at several points across the sample groups and to use these to guide excitation frequency selection. The interaction between clay and moisture in the samples will likely have the largest influence on frequency, so 3 bode plots of the Clay sample group at 0%, 20%, and full saturation were evaluated.

#### **4.4.1 Apparatus:**

- Siglent SDG2122X signal generator
- Siglent SDS1204X-E oscilloscope
- Sensor Array Prototype
- Test Fixture PCB
- Test Samples: *Clay [40 : 60] at 0%, 20% and saturation.*
- Various cables

#### **4.4.2 Methodology:**

The signal generator and oscilloscope were connected via USB to allow the oscilloscope to control the signal generator. Channel 2 of the signal generator was then slaved channel 1. Signal generator channel 2 was then used as a  $V_{in}$  reference signal connected to oscilloscope channel 1 and signal generator channel 1 was connected to the sensor 2 input pin of the prototype through a small test fixture PCB with the output of the sensor then fed into oscilloscope channel 3. The prototype was inserted into a Clay [40 : 60] 0% moisture test sample and the bode plot function was run on the oscilloscope using a  $5 V_{pp}$  sine wave sweep from 1kHz to 40MHz. Once this data was gathered, distilled water was added to the sample, incorporated, and the operation was performed again on the new sample. This was carried out for both the 20% and saturation test samples.

#### **4.4.3 Results Analysis:**

The results of these 3 bode plots were examined to identify any frequencies in this 1kHz to 40MHz band that demonstrate output characteristics beneficial to sensor performance. From this analysis, a constant frequency value for sensor excitation was selected for the next phase of the experiment.

### ***4.5 Characterization of Prototype***

The purpose of this phase was to examine and attempt to characterize the relationship between the output signal of the prototype and soil VMC across variable soil sample groups. These relationships are required to map sensor output signals to estimated soil moisture values through the signal conditioning pipeline.

#### **4.5.1 Apparatus:**

- Siglent SDG2122X signal generator
- Siglent SDS1204X-E oscilloscope
- 3 x Sensor Array Prototype
- Test Fixture PCB
- 10kg of refined kaolinite clay
- 20kg of kiln dried sand
- 2 x 5 litre buckets with lids to hold “master” samples
- Various measuring cylinders
- Electric drill
- Grout mixer drill attachment
- 900ml MUT sample container
- Various cables
- Distilled water as required

-Laptop to record results

-Electronic Scale

#### 4.5.2 Test Samples:

As there are many variables which affect the output of the sensors, the scope of the experiment needed to be limited to allow testing of a single soil feature. Previous research conducted earlier in this project identified clay percentage as a soil parameter which has a large impact on soil moisture sensor output across different soil types, so mixtures of clay and sand were selected as the test sample components. To get some guidance from someone experienced in this field, a meeting was arranged with Dr Julia Easton to discuss how to go about selecting test sample ratios. She suggested doing some research into soil classification and makeup and to base the clay to sand ratios of the test samples on this research. The soil texture triangle below shows a loose classification of soil types versus their sand to clay to silt ratios (soil texture). Anything above 50% clay is classified as a clay soil type. To cover a range of soil types, the test samples were focused on the range from 0% to 60% clay, along the axis of the triangle highlighted in red in the image below.

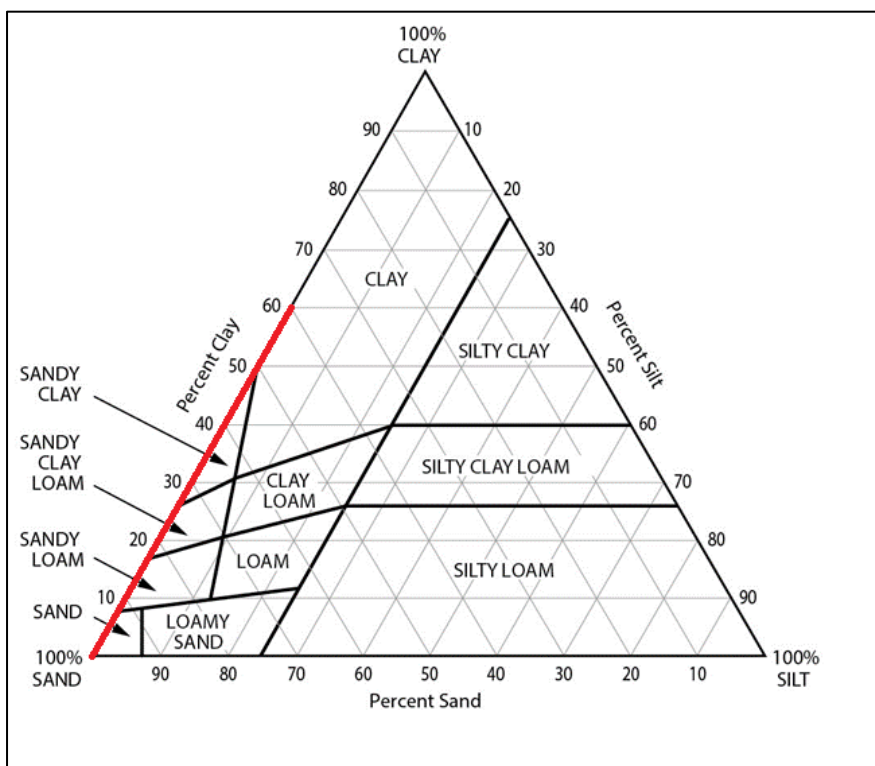


Figure 19: Range of Soil Textures used for Creating Samples.

Refined kaolinite clay was used for the clay component of the samples, and kiln dried sand was used for the sand component. The soil sample groups and their sand to clay ratios are listed below:

1. *Sand [100 : 0]*,
2. *Sandy Loam [80 : 20]*,
3. *Sandy Clay [60 : 40]*,
4. *Clay [40 : 60]*

#### 4.5.3 Sample Preparation:

One of the main hurdles faced in the design of this experiment was developing a method of preparing the samples which would ensure that the mixtures were uniform throughout. Each time water is added to a sample the entire sample would require thorough remixing. The approach developed to ensure sample uniformity is covered in detail here, as it is essential to the quality of the results gathered during this experiment.

1. For each of the 4 soil groups a 2-litre dry “master” mixture was created in a dedicated bucket. These samples were thoroughly mixed with an electric drill and grout mixing drill attachment. Once this initial mixing of the dry soil components was complete, 1 litre of the mixture was measured out and weighed on an electronic scale so the bulk density of each soil type could be calculated and recorded:

$$\text{Bulk Density } (\rho_b) = \frac{\text{Mass (Dry)}}{\text{Volume (Dry)}}$$

Once this measurement had been taken, the 1 litre sample was reincorporated back into the master mixture. This bulk density value could then be used to convert volumetric moisture content (VMC) of results to gravimetric moisture content (GMC) if required:

$$GMC = \frac{VMC}{\rho_b}$$

2. All readings were performed in a smaller test vessel on approximately 800 ml test samples taken from the centre region of the master mixtures after full incorporation. Once readings were obtained, this 800 ml sample was reincorporated back into the master mixture.
3. Distilled water was added in 20 ml to 40 ml increments and incorporated into the master mixture, measurements were taken, and the process was repeated until the master mixture for the soil group reached the point of total saturation and water could no longer be incorporated. This total saturation point varied across the soil sample groups due to the interaction between the clay and water in the samples. Once all results were recorded for the first soil group, the process was repeated for the other 3 groups.

#### 4.5.4 Approach to Measurement:

To measure sensor output on the 800 ml test samples, the sensor array was inserted into the MUT in the centre of the test vessel to ensure the walls of the vessel didn't interfere with the fringing fields of the sensor. The signal generator was setup to generate a  $5 V_{pp}$  sine wave excitation signal at the constant frequency selected during the prototype frequency analysis stage. This input signal was also fed into channel 1 of the oscilloscope and used as a  $V_{in}$  reference signal. The oscilloscope was then used to measure the  $V_{out\ pp}$  of the sensor and time delay between the input and output signals. Measurements were taken for all 4 sensors of the array for each sample so the sensor-to-sensor variance could be examined.

#### **4.5.5 Results Analysis:**

The results of this testing allow individual data series to be created for each of the 4 soil sample groups showing the relationships between the electrical characteristics of the sensor output signal and the soil VMC. These relationships can be used in the signal conditioning pipeline to convert ADC results of the analogue sensor output signal to soil VMC estimates. It was hypothesised that a comparative analysis of these relationships across the 4 soil groups could offer some insight into the influence of the clay component of soil texture on capacitive soil moisture sensor readings.

## 5. Results and Discussion

### 5.1 Investigation and Initial Design Development

#### 5.1.1 Frequency Analysis of IDC and CPC sensors

The CPC sensor frequency results (figure 20) show divergence of the water and methylated spirits samples occurring between ~10 kHz and ~200 kHz. From ~200 kHz to ~10 MHz the permittivity group demonstrate stable responses with  $\Delta f$ . In this frequency range, an increase in  $\epsilon_r$  of the sample results in an increase in magnitude of the output, suggesting permittivity characterization is likely possible. Above ~10 MHz, stability begins to break down as the influence of the pole of the HPF diminishes and  $f$  approaches  $f_{cutoff}$  of the samples. The frequency response of  $\epsilon$  shown in figure 9 of this report suggests this stability would likely continue past the breakdown point shown in this data if a HPF with a higher  $f_{cutoff}$  was used for the test. The ionic group show no discernible divergence for any NaCl concentration at any frequency. This feature renders the dual sensing approach described by Escriba et al unimplementable with this sensor. This is considered a negative feature of these results as the ability to measure ionic characteristics of soil at low frequency is considered a likely source of useful input signals for soil type classification models. It should be noted however, that the region this ionic divergence would likely be occurring in this plot is below -80 dB, and readings this low are likely approaching or below the noise floor of the oscilloscope, so this assumption is made with a low level of confidence.

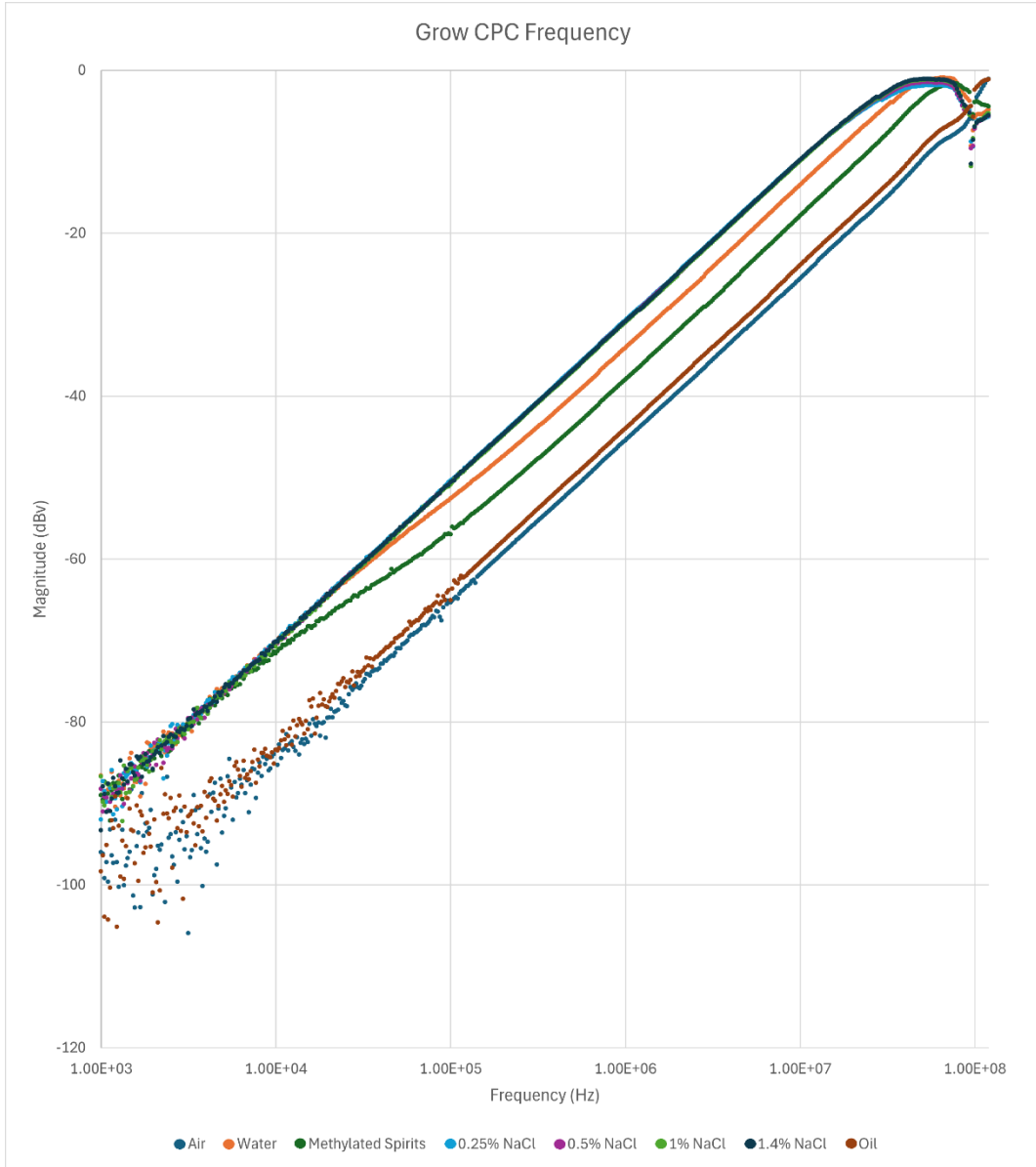
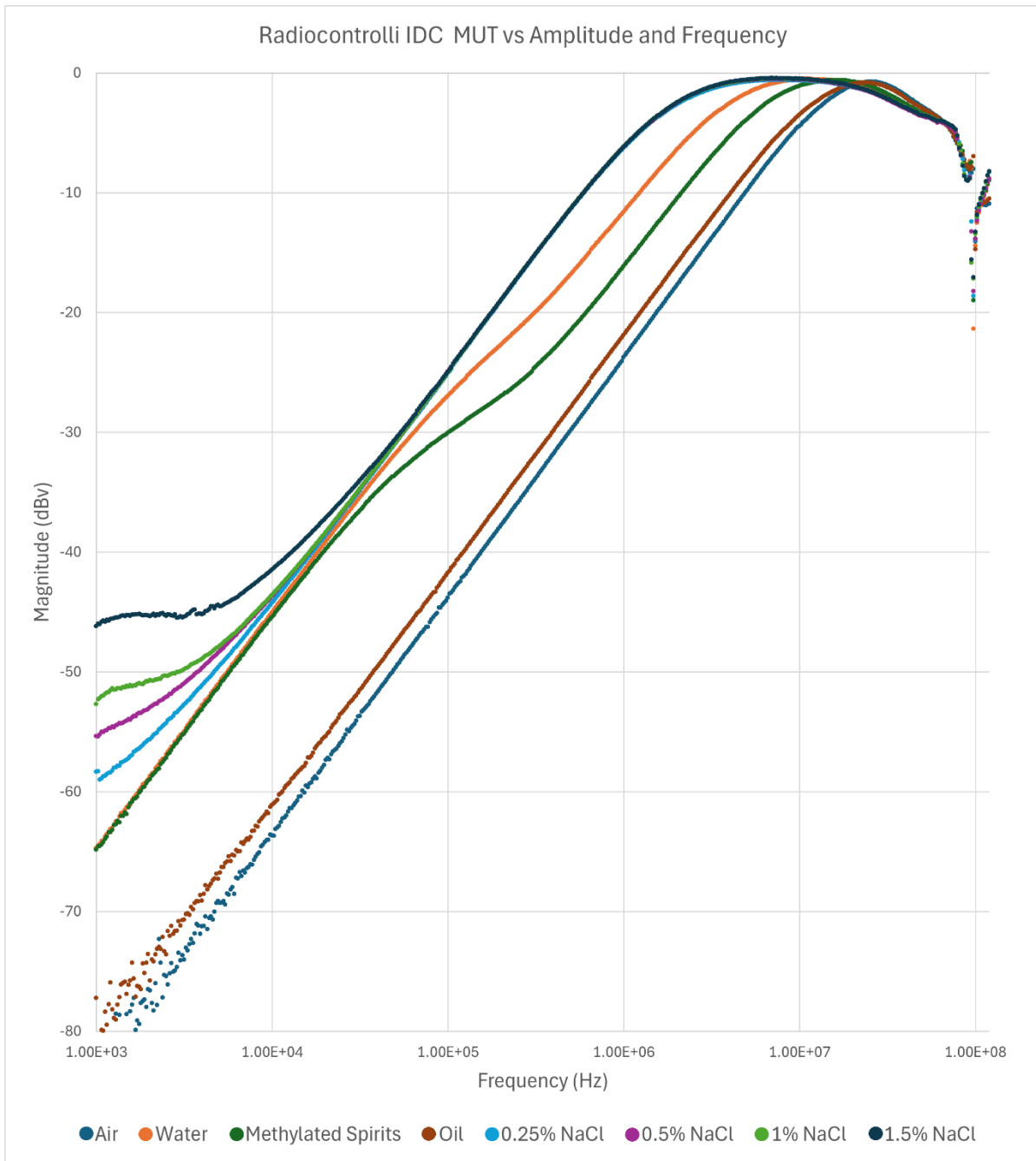


Figure 20: Grow CPC Sensor Frequency Plot.

The IDC sensor results (figure 21) show a transition from an ionic mode towards a dipolar mode of polarization of the MUT centred between 10 kHz and 100 kHz. This feature of the data is highly correlated with the relationship described in figure 9 of this report. Divergence of the water and methylated spirits samples occurs between  $\sim 20$  kHz and  $\sim 800$  kHz. Once divergence is complete, a larger sample  $\epsilon_r$  results in a higher magnitude. The stability seen in the CPC frequency data (figure 20) is much less evident in this dataset due to the higher capacitances of this sensor lowering  $f_{cutoff}$  of the samples, it is likely this frequency stability continues to higher frequencies. The divergence of the NaCl datasets below  $\sim 10$  kHz could enable characterisation of soil parameters such as conductivity and ionic content if the approach of dual frequency characterization demonstrated by Escriba et al were to be implemented in this work.



*Figure 21: Radiocontrolli IDC Sensor Frequency Plot*

A DMM was used to measure the bounds of capacitance of both sensors using the air (lowest) and 1.5% NaCl solution (highest) test samples.

	<b>Radiocontrolli IDC sensor</b>	<b>Grow CPC sensor</b>
Air	110pF	35pF
Submerged in 1.5% NaCl solution	1600pF	80pF

*Table 1: Sensor capacitance values in air and distilled water.*

The larger capacitance range for the IDC sensor of 110-1600pF compared to the CPC sensor range of 35-80pF represents a large increase in the overall dynamic range of the sensor. Maximizing both the lower bound and range of sensor capacitance would be beneficial to future designs. The frequency analysis showed the divergence of the permittivity group was

complete by ~1 MHz for both sensors. Figure 9 shows the minima for the  $\epsilon''$  component occurring between 10 MHz and 100 MHz, an excitation frequency in this 10-100 MHz band is likely suitable for moisture measurement.

### 5.1.2 Substrate Penetration

Figure 22 shows the IDC results of penetration testing into distilled water through the 1mm substrate in brown alongside the submersion in distilled water dataset in blue and the air dataset in yellow. It was initially assumed that these results showed that this sensor was incapable of penetrating the substrate into the MUT, as the substrate dataset is effectively equal to the air dataset. However, a re-examination of this data after the modelling phase of this work identified an error with this assumption that was not initially considered. The apparatus setup used for this testing can be seen in Figure 16 of this report. This testing setup has the sensor electrodes placed between the 1 mm substrate below the electrodes and the approximately 0.3 mm sensor substrate above. It's likely what happened during this testing was that the fringing field of the sensor simply reversed direction to take the path of lowest permittivity and extended out from the back side of the sensor substrate and was sensing the air above the sensor.

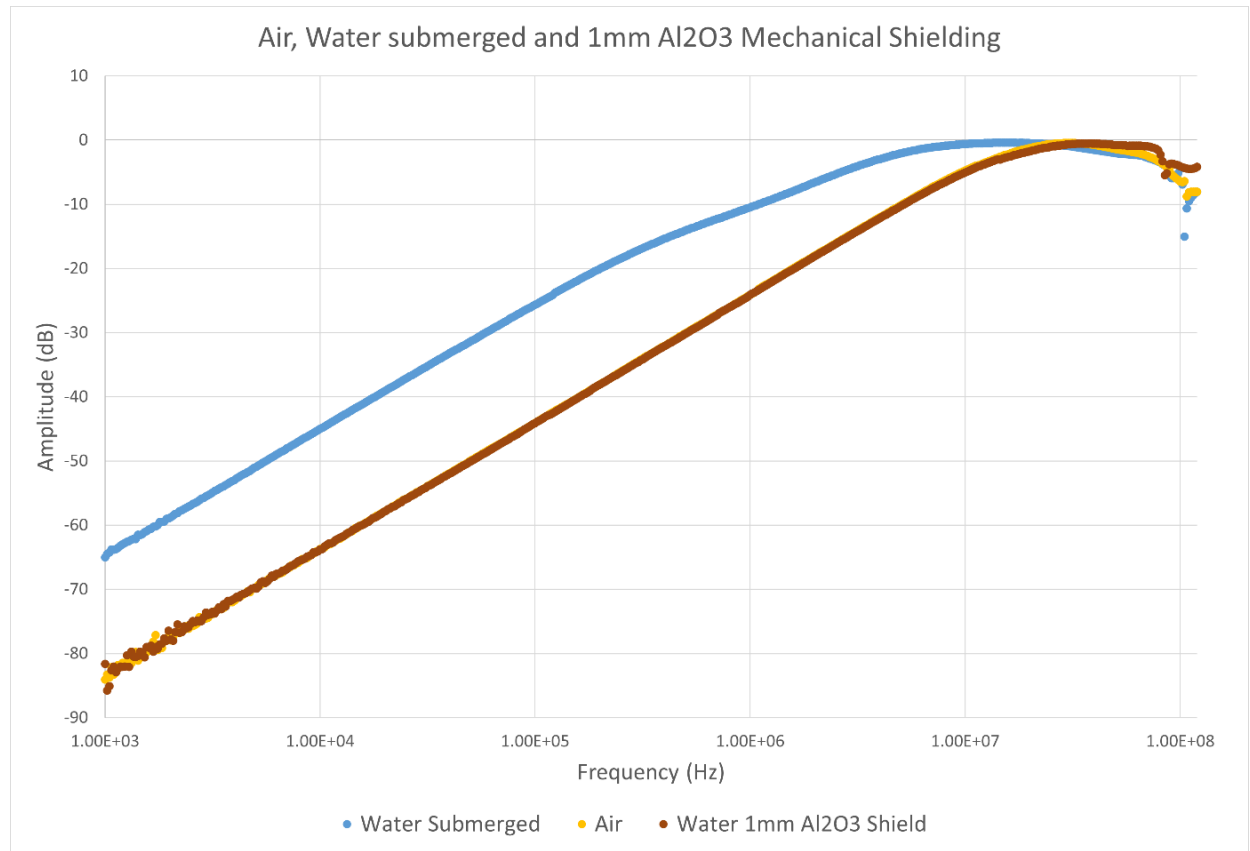
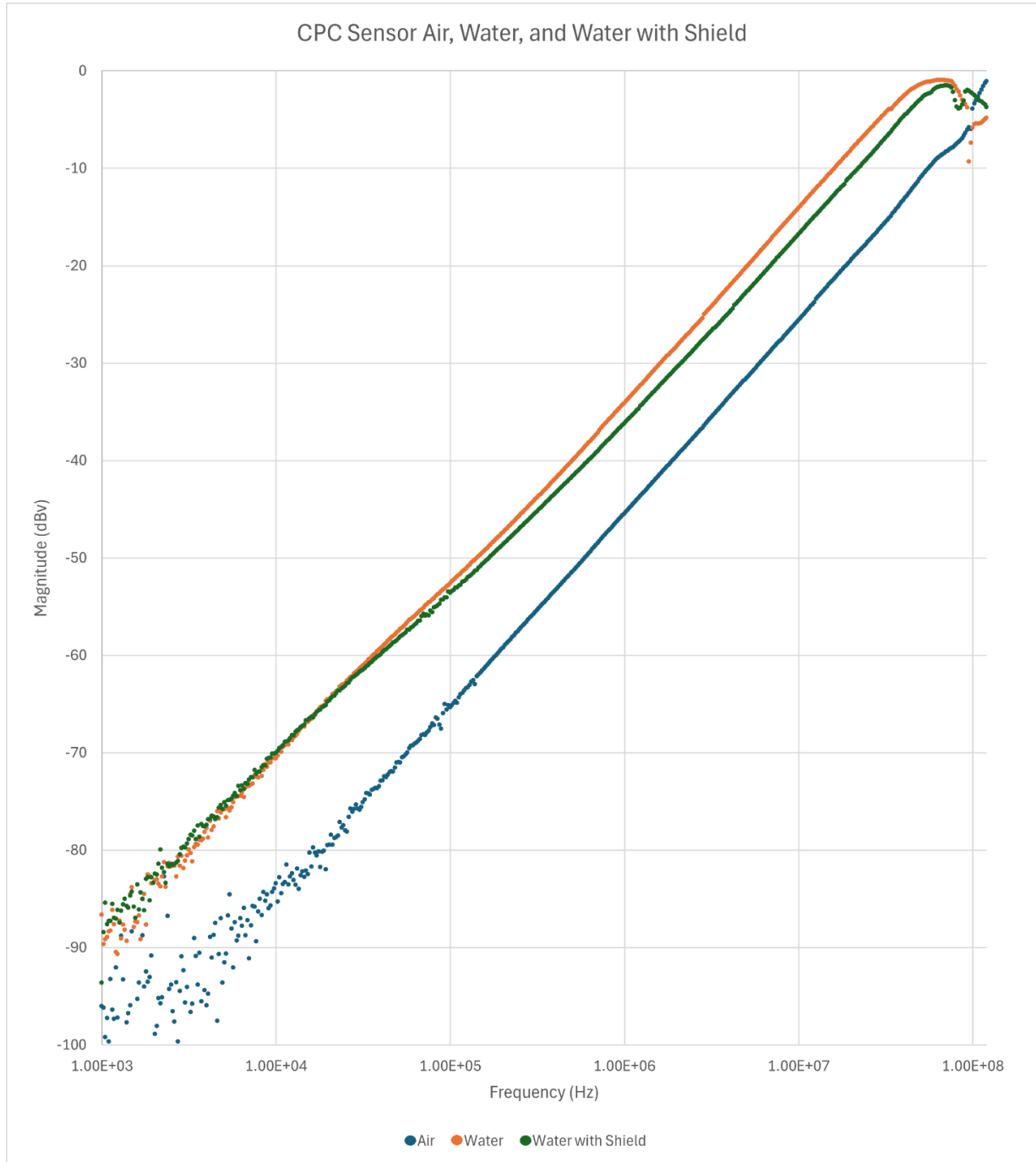


Figure 22: Result of IDC Al<sub>2</sub>O<sub>3</sub> substrate penetration testing.

Figure 23 shows the results of substrate penetration testing performed on the CPC sensor. This test displays promising results for signal retention, with an acceptable drop in magnitude with the shield in place due to the parasitic capacitance introduced by the shield. For this sensor there were additional layers of FR4 PCB substrate and silkscreen that had to be penetrated as the sensor is constructed on the inner 2 copper layers of a 4-layer PCB. This test was

performed twice, the first set of results lost almost all signal above ~30 kHz. In the second test, it was found that placing a blank PCB over the rear of the sensor as a ground plane greatly improved the outcome of the test. The fringing field of this sensor extends out from both the front and rear, the addition of this ground plane negates signal noise from the rear side. The IDC penetration test was rerun with this modification but demonstrated no discernible improvement.



*Figure 23: Result of CPC Al<sub>2</sub>O<sub>3</sub> substrate penetration testing.*

Although the IDC sensor failed to penetrate the alumina substrate, the configuration of this sensor was highly unsuited to this use-case. This sensor was designed for rain sensing applications with fine electrodes in very close proximity to the water droplets being measured. Claudel et al suggest penetration depth of IDC sensors is primarily a function of digit width and inter-digital gap width, so it is likely an IDC with digit dimensions optimized for this use-

case could function more successfully in this application (Claudel, et al. 2021). The use of ground planes for directing the fringing field greatly improved the shield penetration and sensitivity for the CPC sensor. These results identified the penetration of this mechanical shield layer as the most critical constraint on a design. To assist in dealing with this constraint, 51 mm square substrates with a thickness of 0.5 mm and a higher purity of 99.5%  $Al_2O_3$  were sourced for use in further testing.

The main hypotheses drawn from this investigation phase of the project was that CPC designs would likely provide better functionality than IDC designs for this use-case, and that dealing with the attenuation of the fringing field resulting from the addition of the  $Al_2O_3$  shield layer would be the most critical constraint on a design.

## **5.2 Design Optimization**

### 5.2.1 Visual Examination of E-Field Simulations

The modelling process began with visual examinations of the E-Field through various scenarios. This was performed while simultaneously learning how to use the geometry and study components of the software, and unfortunately the number of images of modelling results is limited, but 2 of the main findings will be covered in this section. All the results in this section are from studies performed using the IDC geometry model as the geometry generation for IDC sensors is slightly more involved than the CPC case and was implemented first as it was considered a good way to learn the software.

Once the basic geometry generation was functional, a visual comparison of a single sided IDC and a single sided CPC design was performed. This will be discussed in more depth in the next section, but the data in figure 24 gives a visual representation of one of the major reasons CPC layouts are more suited for this use-case than IDC layouts. The top images show the E-Field of both sensors looking down from above the sensors and demonstrate the trace geometry of the DUT, while the bottom images are a cross section of the PCB and shield layers taken at the centre of the DUT. Comparing the intensity of the E-Field present in the FR4 and  $Al_2O_3$  in the bottom images, it is clear the energy in this loss domain is much higher for the IDC than for the CPC. It is also clear that because of the lower loss of the CPC design, a larger fraction of the E-Field can extend further into the MUT.

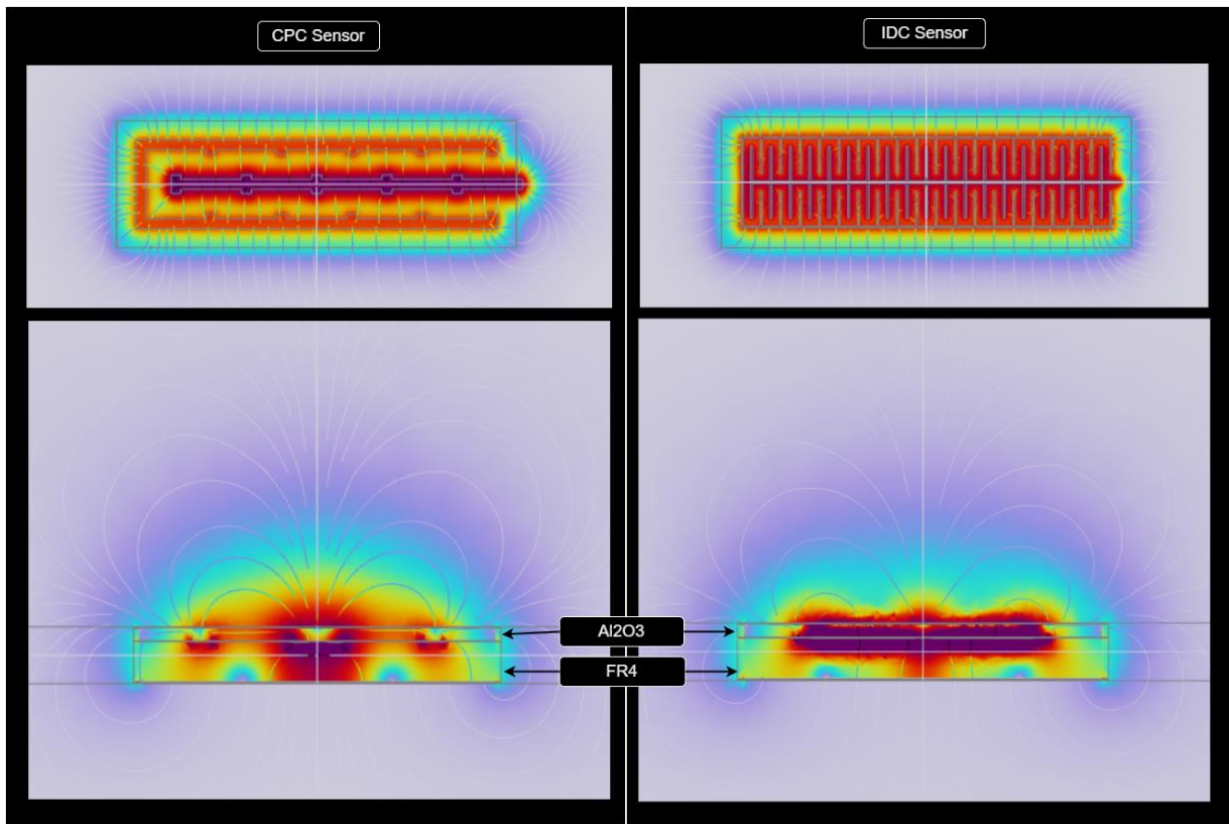


Figure 24: Visual Comparison of E-Field for CPC (Left) and IDC (Right) Designs.

The effect on the E-Field of switching the MUT from air to water was also examined during this phase. Visualizations of this data performed on a double-sided IDC sensor design can be seen in the figure below. This visualization demonstrates how the increase in permittivity of the MUT from  $\sim 1$  for air to  $\sim 80$  for water results in more of the energy being constrained to the loss domain in the FR4 and  $Al_2O_3$  layers of the sensor array.

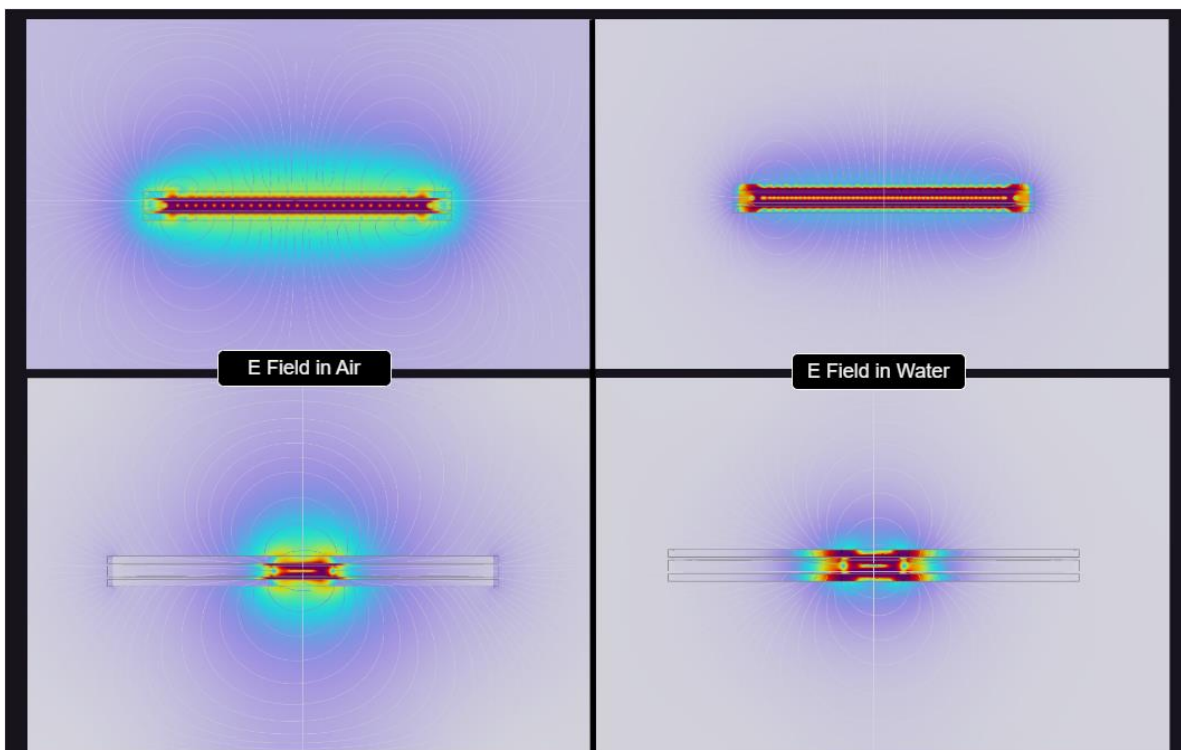


Figure 25: Simulation of E-Field in Air (Left) and Water (Right).

### 5.2.2 IDC Modelling

This IDC modelling was performed early in the modelling process, before any of the CPC parametric sweep studies covered later in this section. IDC sweeps were first performed at a voltage potential of 12 volts and over output digit counts of 5 to 40 and metallization ratios from 0.2 to 0.9. These results were abandoned due to being unworkable for this use-case and further sweeps were performed at 24 volts. The data in the table below shows the results of one of these 24-volt parametric sweeps performed over metallization ratios (MR) from 0.4 to 0.9 and output digit count from 20 to 40.

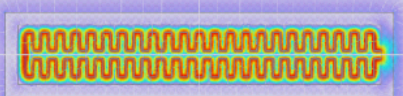
IDC Dual Side 40mm length at 24 Volt																			
Trace Width		Air					Water					Air vs Water Results							
Metal Ratio	Output Digit Count	E Total (J)	C (pF)	E MUT (J)	E-Field Total (V/m)	E-Field MUT (V/m)	E MUT (%)	E Total (J)	C (pF)	E MUT (J)	E-Field Total (V/m)	E Field MUT (V/m)	E MUT (%)	ΔC (pF)	ΔC (%)	ΔE Field MUT (V/m)	ΔE Total (J)		
0.4	20	7.69E-09	26.71	5.05E-09	125.61	98.70	65.61	1.28E-08	44.45	9.94E-09	76.13	45.374	77.63	17.74	39.91	53.33	5.11E-09		
0.4	24	1.06E-08	36.69	6.97E-09	130.15	99.23	65.92	1.51E-08	52.34	1.13E-08	80.62	46.243	74.79	15.65	29.90	52.98	4.51E-09		
0.4	28	1.36E-08	47.24	9.01E-09	133.62	99.33	66.20	1.75E-08	60.89	1.28E-08	84.61	47.182	72.74	13.65	22.42	52.15	3.93E-09		
0.4	32	1.66E-08	58.21	1.11E-08	136.21	99.04	66.44	2.02E-08	70.02	1.44E-08	88.09	48.08	71.28	11.81	16.87	50.96	3.40E-09		
0.4	36	1.98E-08	68.89	1.32E-08	137.71	98.35	66.67	2.28E-08	79.05	1.60E-08	90.67	48.743	70.27	10.17	12.86	49.61	2.93E-09		
0.4	40	2.31E-08	80.13	1.54E-08	139.23	97.81	66.82	2.56E-08	88.96	1.78E-08	93.35	49.583	69.55	8.83	9.93	48.22	2.54E-09		
0.5	20	9.01E-09	31.30	5.91E-09	128.85	100.45	65.60	1.46E-08	50.59	1.13E-08	80.46	48.341	77.41	19.30	38.14	52.11	5.56E-09		
0.5	24	1.23E-08	42.82	8.12E-09	134.3	101.55	65.85	1.72E-08	59.79	1.28E-08	85.43	49.222	74.50	16.97	28.38	52.33	4.89E-09		
0.5	28	1.58E-08	54.97	1.05E-08	138.33	101.99	66.21	2.01E-08	69.67	1.45E-08	89.62	50.136	72.51	14.70	21.10	51.85	4.24E-09		
0.5	32	1.93E-08	67.11	1.29E-08	140.92	101.73	66.49	2.30E-08	79.70	1.63E-08	92.85	50.799	71.09	12.59	15.80	50.93	3.63E-09		
0.5	36	2.31E-08	80.29	1.54E-08	143.39	101.56	66.67	2.62E-08	91.14	1.84E-08	96.25	51.789	70.07	10.85	11.90	49.77	3.12E-09		
0.5	40	2.68E-08	93.02	1.79E-08	144.89	101.00	66.81	2.95E-08	102.37	2.05E-08	98.82	52.524	69.36	9.35	9.13	48.48	2.69E-09		
0.6	20	1.06E-08	36.91	6.97E-09	131.63	101.85	65.60	1.66E-08	57.49	1.27E-08	84.34	50.953	76.88	20.58	35.80	50.90	5.93E-09		
0.6	24	1.45E-08	50.34	9.55E-09	137.9	103.46	65.90	1.97E-08	68.35	1.46E-08	89.65	51.835	74.05	18.01	26.35	51.63	5.19E-09		
0.6	28	1.86E-08	64.46	1.23E-08	142.54	104.31	66.26	2.30E-08	80.02	1.66E-08	94.15	52.79	72.14	15.56	19.44	51.52	4.48E-09		
0.6	32	2.29E-08	79.62	1.52E-08	146.27	104.65	66.45	2.68E-08	92.98	1.89E-08	98.32	53.816	70.71	13.36	14.37	50.83	3.85E-09		
0.6	36	2.71E-08	94.03	1.80E-08	148.3	104.26	66.64	3.04E-08	105.41	2.12E-08	101.14	54.447	69.77	11.38	10.80	49.81	3.28E-09		
0.6	40	3.12E-08	108.39	2.09E-08	149.72	103.73	66.85	3.40E-08	118.13	2.35E-08	103.52	55.084	69.18	9.74	8.25	48.65	2.81E-09		
0.7	20	1.28E-08	44.48	8.42E-09	134.12	103.02	65.77	1.90E-08	66.02	1.45E-08	87.89	53.286	76.13	21.55	32.63	49.73	6.21E-09		
0.7	24	1.73E-08	60.00	1.14E-08	141.02	105.08	66.05	2.27E-08	78.82	1.67E-08	93.43	54.171	73.48	18.81	23.87	50.91	5.42E-09		
0.7	28	2.21E-08	76.78	1.47E-08	146.2	106.24	66.30	2.68E-08	92.96	1.92E-08	98.21	55.126	71.61	16.19	17.41	51.11	4.66E-09		
0.7	32	2.70E-08	93.74	1.79E-08	149.81	106.60	66.40	3.10E-08	107.57	2.18E-08	102.06	55.933	70.26	13.83	12.86	50.67	3.98E-09		
0.7	36	3.19E-08	110.63	2.12E-08	152.22	106.42	66.51	3.52E-08	122.38	2.44E-08	105.10	56.58	69.33	11.75	9.60	49.84	3.39E-09		
0.7	40	3.73E-08	129.38	2.49E-08	154.5	106.40	66.76	4.02E-08	139.46	2.76E-08	108.21	57.6	68.83	10.08	7.23	48.80	2.90E-09		
0.8	20	1.61E-08	55.88	1.06E-08	136.42	104.01	65.89	2.25E-08	78.06	1.68E-08	91.22	55.353	74.95	22.17	28.41	48.66	6.39E-09		
0.8	24	2.16E-08	75.02	1.43E-08	144.03	105.54	66.04	2.72E-08	94.36	1.97E-08	97.15	56.341	72.47	19.35	20.50	50.20	5.57E-09		
0.8	28	2.76E-08	95.83	1.83E-08	149.73	108.06	66.23	3.24E-08	112.44	2.29E-08	102.19	57.369	70.77	16.61	14.77	50.69	4.78E-09		
0.8	32	3.39E-08	117.54	2.24E-08	153.88	108.74	66.32	3.79E-08	131.69	2.64E-08	106.37	58.284	69.56	14.15	10.74	50.46	4.08E-09		
0.8	36	4.00E-08	138.94	2.66E-08	156.74	108.88	66.40	4.35E-08	151.01	2.99E-08	109.70	59.086	68.77	12.07	7.99	49.79	3.48E-09		
0.8	40	4.60E-08	159.80	3.06E-08	158.59	108.60	66.48	4.90E-08	170.13	3.34E-08	112.27	59.71	68.24	10.33	6.07	48.89	2.98E-09		
0.9	20	2.22E-08	77.00	1.46E-08	138.29	104.68	65.77	2.86E-08	99.42	2.09E-08	94.09	57.017	73.01	22.42	22.55	47.66	6.46E-09		
0.9	24	2.98E-08	103.49	1.96E-08	146.71	107.79	65.83	3.54E-08	123.08	2.51E-08	100.52	58.222	70.87	19.59	15.92	49.57	5.64E-09		
0.9	28	3.85E-08	133.58	2.54E-08	153.05	109.76	66.12	4.33E-08	150.43	3.01E-08	105.97	59.482	69.59	16.85	11.20	50.28	4.85E-09		
0.9	32	4.77E-08	165.52	3.15E-08	157.73	110.82	66.05	5.18E-08	179.91	3.55E-08	110.49	60.557	68.49	14.39	8.00	50.26	4.14E-09		
0.9	36	5.67E-08	196.75	3.76E-08	160.9	111.27	66.30	6.02E-08	209.04	4.10E-08	113.93	61.477	68.06	12.29	5.88	49.79	3.54E-09		
0.9	40	7.12E-08	247.19	4.66E-08	165.94	112.31	65.43	7.42E-08	257.80	4.95E-08	119.57	63.299	66.68	10.61	4.12	49.01	3.06E-09		

Figure 26: Simulation Results for Dual Sided 40mm IDC.

The percentage change in capacitance values in this data, along with the visual examination of the data presented in figure 24 of this report confirm the hypothesis generated during the investigation phase that IDC sensors were not well suited to this use-case. From this point onwards the project focussed only on CPC sensor designs.

### 5.2.3 Data Presentation of CPC Modelling

Figure 27 has been included to clarify the data presentation of CPC modelling throughout the remainder of this section.

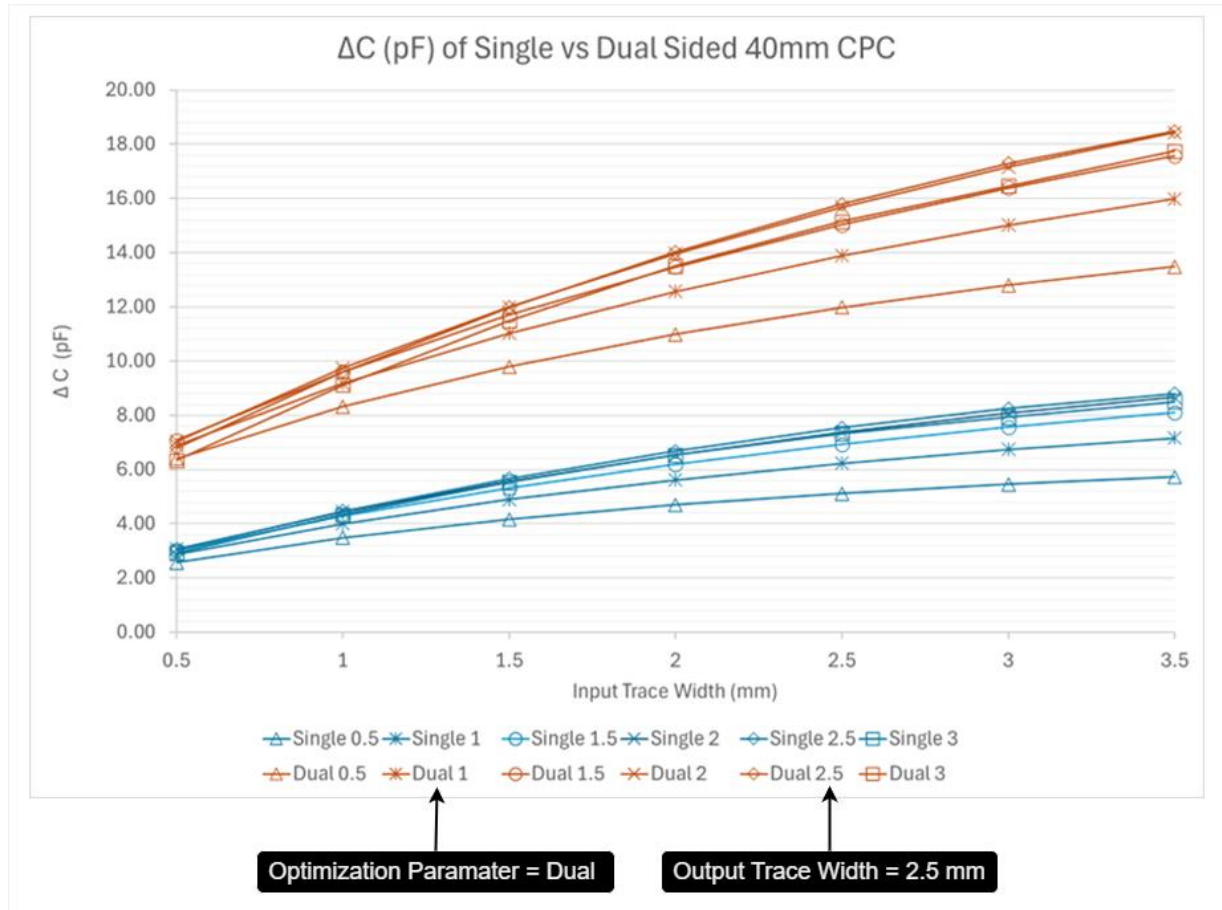


Figure 27: A Note on Data Presentation for CPC Modelling.

### 5.2.4 CPC Single vs Dual Sided

Trace Width		Air						Water						Air vs Water Results			
Output	Input	E Total (J)	C (pF)	E MUT (J)	E-Field Total (V/m)	E-Field MUT (V/m)	E MUT (%)	E Total (J)	C (pF)	E MUT (J)	E-Field Total (V/m)	E Field MUT (V/m)	E MUT (%)	$\Delta C$ (pF)	$\Delta C$ (%)	$\Delta E$ Field MUT (V/m)	$\Delta E$ Total (J)
0.5	0.5	7.32E-10	2.54	3.34E-10	13.37	9.38	45.70	1.47E-09	5.12	1.10E-09	6.66	3.54	74.69	2.58	50.36	5.84	7.42E-10
0.5	1	8.45E-10	2.93	3.69E-10	15.11	10.58	43.64	1.85E-09	6.42	1.40E-09	8.10	4.34	75.64	3.49	54.29	6.24	1.00E-09
0.5	1.5	9.43E-10	3.28	4.02E-10	16.48	11.50	42.58	2.14E-09	7.44	1.63E-09	9.15	4.93	76.02	4.17	56.00	6.57	1.20E-09
0.5	2	1.04E-09	3.60	4.36E-10	17.64	12.27	42.11	2.39E-09	8.30	1.82E-09	9.98	5.38	76.14	4.70	56.65	6.89	1.35E-09
0.5	2.5	1.13E-09	3.91	4.74E-10	18.63	12.92	42.08	2.60E-09	9.03	1.98E-09	10.63	5.74	76.15	5.12	56.70	7.18	1.47E-09
0.5	3	1.22E-09	4.22	5.15E-10	19.51	13.48	42.36	2.79E-09	9.68	2.12E-09	11.16	6.01	76.11	5.46	56.37	7.46	1.57E-09
0.5	3.5	1.31E-09	4.55	5.62E-10	20.27	13.96	42.90	2.96E-09	10.27	2.25E-09	11.60	6.24	76.02	5.73	55.76	7.72	1.65E-09
1	0.5	7.76E-10	2.69	3.55E-10	13.06	9.08	45.77	1.60E-09	5.57	1.20E-09	6.79	3.61	75.10	2.87	51.59	5.47	8.27E-10
1	1	9.05E-10	3.14	3.94E-10	14.88	10.32	43.57	2.06E-09	7.14	1.57E-09	8.43	4.52	76.28	4.00	56.00	5.79	1.15E-09
1	1.5	1.02E-09	3.54	4.32E-10	16.31	11.27	42.40	2.43E-09	8.43	1.86E-09	9.67	5.22	76.79	4.89	58.02	6.05	1.41E-09
1	2	1.13E-09	3.92	4.73E-10	17.56	12.09	41.89	2.75E-09	9.55	2.12E-09	10.69	5.78	77.05	5.62	58.90	6.31	1.62E-09
1	2.5	1.24E-09	4.31	5.19E-10	18.65	12.79	41.82	3.04E-09	10.54	2.34E-09	11.53	6.24	77.13	6.23	59.12	6.55	1.79E-09
1	3	1.36E-09	4.70	5.71E-10	19.62	13.41	42.11	3.30E-09	11.45	2.54E-09	12.24	6.62	77.12	6.74	58.89	6.79	1.94E-09
1	3.5	1.47E-09	5.12	6.30E-10	20.47	13.93	42.73	3.54E-09	12.28	2.72E-09	12.82	6.92	77.06	7.16	58.29	7.01	2.06E-09
1.5	0.5	8.17E-10	2.84	3.81E-10	12.51	8.61	46.60	1.69E-09	5.86	1.27E-09	6.74	3.57	75.27	3.02	51.57	5.04	8.70E-10
1.5	1	9.62E-10	3.34	4.27E-10	14.34	9.84	44.39	2.20E-09	7.63	1.68E-09	8.46	4.53	76.53	4.29	56.20	5.31	1.23E-09
1.5	1.5	1.09E-09	3.80	4.72E-10	15.80	10.81	43.22	2.63E-09	9.12	2.03E-09	9.82	5.29	77.13	5.32	58.38	5.51	1.53E-09
1.5	2	1.22E-09	4.25	5.23E-10	17.07	11.63	42.75	3.01E-09	10.44	2.33E-09	10.94	5.92	77.43	6.20	59.32	5.71	1.78E-09
1.5	2.5	1.36E-09	4.72	5.81E-10	18.21	12.36	42.78	3.36E-09	11.65	2.60E-09	11.90	6.44	77.55	6.93	59.51	5.91	2.00E-09
1.5	3	1.50E-09	5.22	6.51E-10	19.24	13.00	43.24	3.68E-09	12.80	2.86E-09	12.72	6.89	77.55	7.57	59.17	6.11	2.18E-09
1.5	3.5	1.67E-09	5.78	7.34E-10	20.15	13.56	44.07	4.00E-09	13.89	3.10E-09	13.41	7.26	77.45	8.10	58.35	6.30	2.33E-09
2	0.5	8.64E-10	3.00	4.15E-10	11.79	8.05	48.08	1.75E-09	6.08	1.32E-09	6.59	3.48	75.23	3.08	50.62	4.56	8.86E-10
2	1	1.03E-09	3.57	4.73E-10	13.61	9.26	45.95	2.31E-09	8.01	1.77E-09	8.35	4.47	76.57	4.44	55.41	4.79	1.28E-09
2	1.5	1.18E-09	4.11	5.32E-10	15.08	10.22	44.96	2.79E-09	9.68	2.15E-09	9.76	5.26	77.26	5.57	57.58	4.96	1.61E-09
2	2	1.34E-09	4.66	5.99E-10	16.38	11.05	44.65	3.23E-09	11.21	2.50E-09	10.96	5.93	77.55	6.55	58.42	5.12	1.89E-09
2	2.5	1.52E-09	5.26	6.80E-10	17.53	11.78	44.87	3.64E-09	12.64	2.82E-09	11.98	6.50	77.61	7.38	58.37	5.28	2.12E-09
2	3	1.71E-09	5.94	7.82E-10	18.57	12.43	45.68	4.04E-09	14.02	3.13E-09	12.85	6.98	77.54	8.08	57.62	5.45	2.33E-09
2	3.5	1.95E-09	6.77	9.15E-10	19.52	13.00	46.94	4.44E-09	15.43	3.43E-09	13.62	7.39	77.31	8.66	56.14	5.61	2.49E-09
2.5	0.5	9.27E-10	3.22	4.67E-10	10.90	7.38	50.35	1.81E-09	6.27	1.36E-09	6.36	3.35	75.10	3.05	48.63	4.03	8.78E-10
2.5	1	1.12E-09	3.90	5.43E-10	12.70	8.57	48.44	2.41E-09	8.37	1.84E-09	8.13	4.34	76.46	4.47	53.43	4.23	1.29E-09
2.5	1.5	1.31E-09	4.56	6.26E-10	14.17	9.52	47.65	2.95E-09	10.23	2.27E-09	9.57	5.15	77.09	5.67	55.43	4.37	1.63E-09
2.5	2	1.52E-09	5.28	7.25E-10	15.45	10.34	47.71	3.44E-09	11.96	2.66E-09	10.78	5.83	77.34	6.68	55.87	4.50	1.92E-09
2.5	2.5	1.77E-09	6.13	8.55E-10	16.62	11.06	48.38	3.94E-09	13.67	3.04E-09	11.83	6.42	77.25	7.54	55.15	4.65	2.17E-09
2.5	3	2.08E-09	7.23	1.04E-09	17.69	11.72	49.84	4.46E-09	15.49	3.43E-09	12.75	6.92	76.99	8.26	53.31	4.80	2.38E-09
2.5	3.5	2.53E-09	8.78	1.31E-09	18.66	12.31	51.96	5.06E-09	17.57	3.87E-09	13.53	7.35	76.42	8.80	50.05	4.96	2.53E-09
3	0.5	1.03E-09	3.57	5.50E-10	9.82	6.59	53.52	1.87E-09	6.50	1.40E-09	6.08	3.19	74.83	2.93	45.07	3.40	8.43E-10
3	1	1.27E-09	4.41	6.61E-10	11.57	7.74	52.01	2.52E-09	8.75	1.92E-09	7.79	4.15	76.08	4.33	49.55	3.59	1.25E-09
3	1.5	1.53E-09	5.33	7.93E-10	13.02	8.67	51.66	3.13E-09	10.86	2.39E-09	9.21	4.95	76.54	5.53	50.93	3.72	1.59E-09
3	2	1.86E-09	6.46	9.73E-10	14.32	9.49	52.32	3.74E-09	12.99	2.86E-09	10.42	5.64	76.57	6.53	50.30	3.85	1.88E-09
3	2.5	2.31E-09	8.02	1.24E-09	15.50	10.22	53.85	4.42E-09	15.35	3.37E-09	11.45	6.21	76.14	7.33	47.73	4.01	2.11E-09
3	3	3.17E-09	11.00	1.80E-09	16.59	10.90	56.93	5.46E-09	18.94	4.10E-09	12.36	6.72	75.24	7.94	41.90	4.18	2.29E-09
3	3.5	5.41E-09	9.75	2.67E-09	17.80	11.31	49.47	7.77E-09	18.27	5.06E-09	13.64	7.03	65.07	8.51	46.60	4.28	2.36E-09

Figure 28: Simulation Results for Single Sided 40mm CPC.

CPC Dual Side 40mm length at 12 Volt																			
Trace Width		Air					Water					Air vs Water Results							
Input	Input	E Total (J)	C (pF)	E MUT (J)	E-Field Total (V/m)	E-Field MUT (V/m)	E MUT (%)	E Total (J)	C (pF)	E MUT (J)	E-Field Total (V/m)	E Field MUT (V/m)	E MUT (%)	ΔC (pF)	ΔC (%)	ΔE Field MUT (V/m)	ΔE Total (J)		
0.5	0.5	8.54E-10	2.97	5.70E-10	34.03	30.88	66.76	2.70E-09	9.37	2.22E-09	11.64	7.83	82.43	6.40	68.33	23.05	1.84E-09		
0.5	1	9.42E-10	3.27	6.29E-10	36.95	33.60	66.81	3.34E-09	11.59	2.82E-09	13.78	9.47	84.54	8.32	71.78	24.13	2.40E-09		
0.5	1.5	1.02E-09	3.55	6.84E-10	39.29	35.81	66.90	3.84E-09	13.35	3.29E-09	15.29	10.68	85.50	9.79	73.38	25.13	2.82E-09		
0.5	2	1.11E-09	3.85	7.42E-10	41.39	37.80	66.98	4.27E-09	14.84	3.67E-09	16.44	11.62	85.92	11.00	74.09	26.18	3.17E-09		
0.5	2.5	1.20E-09	4.16	8.04E-10	43.33	39.66	67.03	4.65E-09	16.15	4.00E-09	17.35	12.36	86.00	11.98	74.21	27.30	3.45E-09		
0.5	3	1.30E-09	4.52	8.72E-10	45.17	41.42	67.03	4.99E-09	17.31	4.28E-09	18.07	12.96	85.86	12.80	73.92	28.46	3.69E-09		
0.5	3.5	1.42E-09	4.92	9.49E-10	46.91	43.08	67.00	5.30E-09	18.40	4.54E-09	18.66	13.44	85.61	13.49	73.28	29.64	3.88E-09		
1	0.5	9.39E-10	3.26	6.24E-10	32.01	28.90	66.40	2.92E-09	10.15	2.43E-09	11.58	7.88	83.07	6.89	67.86	21.02	1.98E-09		
1	1	1.05E-09	3.63	6.95E-10	35.03	31.69	66.43	3.69E-09	12.82	3.16E-09	13.95	9.71	85.57	9.19	71.68	21.98	2.65E-09		
1	1.5	1.15E-09	3.98	7.62E-10	37.46	33.98	66.50	4.32E-09	15.00	3.75E-09	15.69	11.12	86.84	11.03	73.49	22.86	3.18E-09		
1	2	1.25E-09	4.35	8.34E-10	39.65	36.06	66.58	4.87E-09	16.91	4.26E-09	17.06	12.26	87.45	12.57	74.30	23.80	3.62E-09		
1	2.5	1.37E-09	4.76	9.13E-10	41.71	38.02	66.63	5.37E-09	18.64	4.71E-09	18.19	13.20	87.67	13.89	74.48	24.82	4.00E-09		
1	3	1.51E-09	5.23	1.00E-09	43.68	39.89	66.63	5.83E-09	20.25	5.11E-09	19.13	13.98	87.63	15.02	74.19	25.91	4.33E-09		
1	3.5	1.66E-09	5.77	1.11E-09	45.55	41.67	66.61	6.27E-09	21.76	5.48E-09	19.92	14.62	87.39	15.99	73.47	27.05	4.60E-09		
1.5	0.5	1.04E-09	3.62	6.89E-10	29.53	26.46	66.03	3.08E-09	10.69	2.56E-09	11.28	7.72	83.16	7.07	66.14	18.74	2.04E-09		
1.5	1	1.17E-09	4.08	7.75E-10	32.57	29.27	66.02	3.94E-09	13.68	3.38E-09	13.73	9.64	85.81	9.60	70.21	19.63	2.77E-09		
1.5	1.5	1.30E-09	4.52	8.60E-10	35.05	31.60	66.09	4.67E-09	16.21	4.07E-09	15.59	11.17	87.20	11.70	72.14	20.43	3.37E-09		
1.5	2	1.44E-09	5.00	9.52E-10	37.30	33.72	66.17	5.32E-09	18.48	4.68E-09	17.08	12.42	87.90	13.48	72.96	21.30	3.88E-09		
1.5	2.5	1.60E-09	5.55	1.06E-09	39.42	35.73	66.22	5.93E-09	20.58	5.22E-09	18.34	13.48	88.15	15.03	73.04	22.25	4.33E-09		
1.5	3	1.79E-09	6.21	1.18E-09	41.45	37.66	66.26	6.51E-09	22.60	5.73E-09	19.42	14.39	88.09	16.39	72.54	23.27	4.72E-09		
1.5	3.5	2.02E-09	7.01	1.34E-09	43.42	39.51	66.27	7.08E-09	24.59	6.21E-09	20.36	15.16	87.76	17.57	71.48	24.35	5.06E-09		
2	0.5	1.18E-09	4.09	7.73E-10	26.78	23.77	65.67	3.21E-09	11.13	2.66E-09	10.88	7.46	82.85	7.04	63.25	16.31	2.03E-09		
2	1	1.35E-09	4.67	8.83E-10	29.85	26.59	65.63	4.15E-09	14.41	3.55E-09	13.35	9.42	85.56	9.74	67.58	17.17	2.81E-09		
2	1.5	1.51E-09	5.26	9.95E-10	32.35	28.93	65.71	4.97E-09	17.25	4.32E-09	15.25	10.99	86.97	11.99	69.53	17.94	3.45E-09		
2	2	1.71E-09	5.92	1.12E-09	34.65	31.08	65.80	5.73E-09	19.89	5.02E-09	16.83	12.32	87.64	13.96	70.21	18.76	4.02E-09		
2	2.5	1.94E-09	6.72	1.28E-09	36.82	33.13	65.87	6.45E-09	22.40	5.66E-09	18.19	13.47	87.79	15.67	69.99	19.66	4.51E-09		
2	3	2.22E-09	7.72	1.47E-09	38.91	35.08	65.98	7.16E-09	24.87	6.27E-09	19.37	14.45	87.57	17.15	68.97	20.64	4.94E-09		
2	3.5	2.60E-09	9.04	1.72E-09	40.95	36.98	66.08	7.91E-09	27.48	6.88E-09	20.43	15.30	86.98	18.43	67.09	21.68	5.31E-09		
2.5	0.5	1.36E-09	4.74	8.92E-10	23.81	20.87	65.38	3.32E-09	11.53	2.73E-09	10.39	7.11	82.17	6.79	58.93	13.76	1.96E-09		
2.5	1	1.59E-09	5.54	1.04E-09	26.92	23.70	65.31	4.36E-09	15.14	3.70E-09	12.87	9.07	84.82	9.61	63.45	14.63	2.77E-09		
2.5	1.5	1.84E-09	6.38	1.20E-09	29.48	26.06	65.40	5.29E-09	18.36	4.55E-09	14.81	10.68	86.13	11.98	65.27	15.39	3.45E-09		
2.5	2	2.13E-09	7.38	1.39E-09	31.83	28.25	65.58	6.16E-09	21.40	5.34E-09	16.44	12.04	86.63	14.02	65.52	16.21	4.04E-09		
2.5	2.5	2.50E-09	8.69	1.64E-09	34.05	30.31	65.72	7.05E-09	24.48	6.10E-09	17.86	13.22	86.49	15.79	64.51	17.09	4.55E-09		
2.5	3	3.03E-09	10.52	2.00E-09	36.22	32.30	65.94	8.01E-09	27.81	6.87E-09	19.13	14.24	85.83	17.29	62.17	18.06	4.98E-09		
2.5	3.5	3.83E-09	13.31	2.54E-09	38.34	34.23	66.32	9.15E-09	31.79	7.75E-09	20.27	15.12	84.64	18.48	58.13	19.11	5.32E-09		
3	0.5	1.64E-09	5.71	1.07E-09	20.67	17.79	65.21	3.47E-09	12.04	2.81E-09	9.86	6.68	80.98	6.34	52.61	11.11	1.82E-09		
3	1	1.98E-09	6.88	1.29E-09	23.80	20.60	65.20	4.61E-09	16.01	3.84E-09	12.28	8.59	83.40	9.12	56.99	12.01	2.63E-09		
3	1.5	2.37E-09	8.24	1.55E-09	26.42	22.98	65.32	5.69E-09	19.74	4.80E-09	14.23	10.17	84.36	11.50	58.24	12.81	3.31E-09		
3	2	2.90E-09	10.08	1.90E-09	28.84	25.19	65.61	6.80E-09	23.59	5.74E-09	15.89	11.54	84.40	13.52	57.29	13.65	3.89E-09		
3	2.5	3.69E-09	12.82	2.44E-09	31.16	27.29	66.02	8.06E-09	27.97	6.74E-09	17.34	12.70	83.61	15.15	54.17	14.59	4.36E-09		
3	3	5.33E-09	18.51	3.56E-09	33.47	29.36	66.75	1.01E-08	34.97	8.22E-09	18.71	13.75	81.65	16.46	47.06	15.61	4.74E-09		
3	3.5	9.68E-09	15.50	5.27E-09	35.54	30.65	54.49	1.46E-08	33.25	1.01E-08	20.03	14.33	69.28	17.75	53.38	16.31	4.93E-09		

Figure 29: Simulation Results of Dual Sided 40mm CPC.

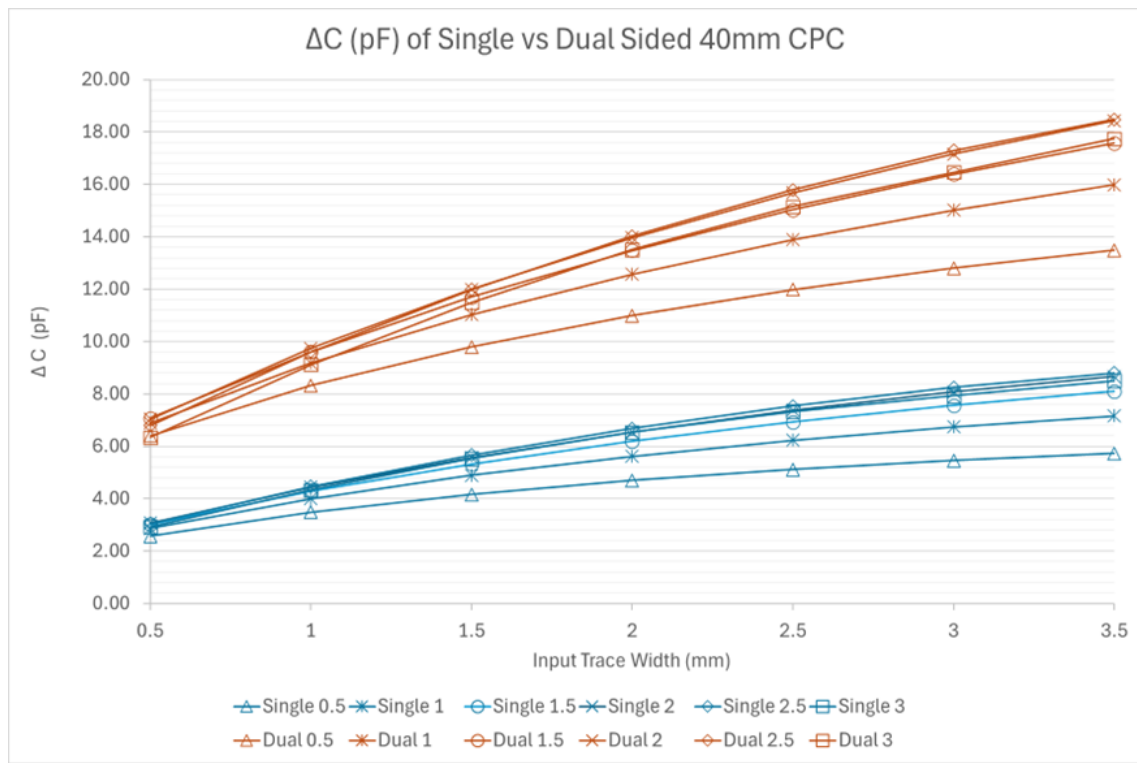


Figure 30: Change in Capacitance of Single and Dual Sided 40mm CPC.

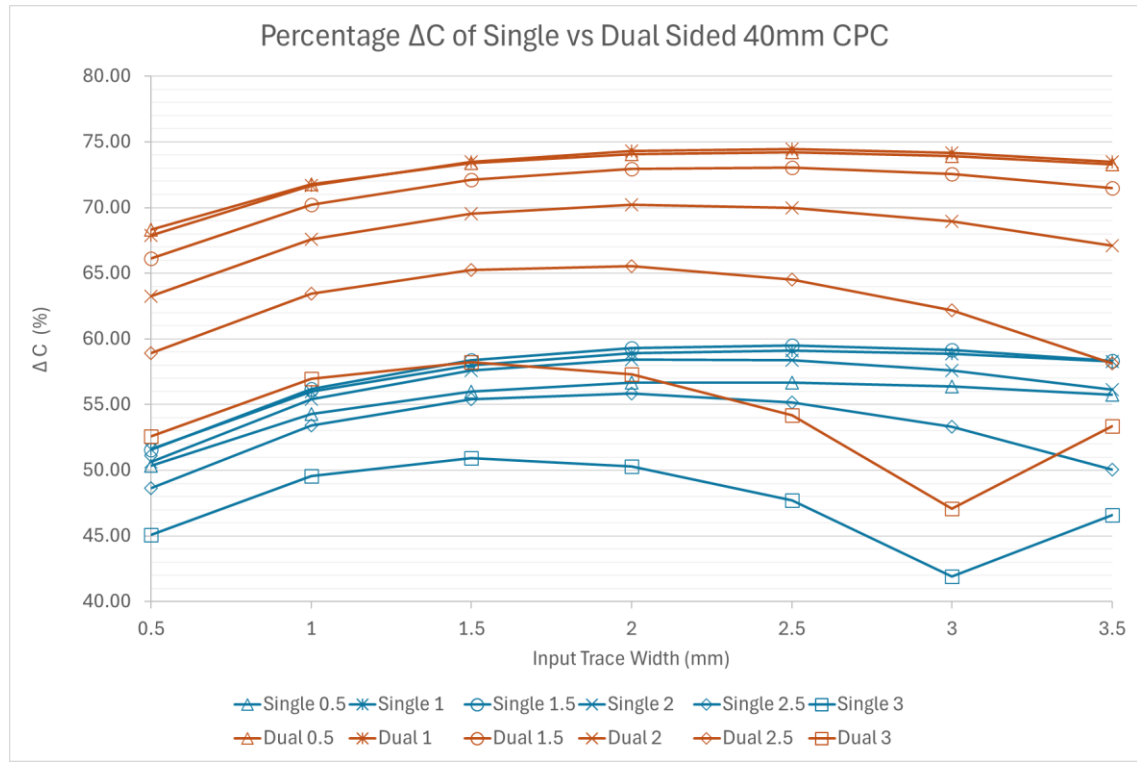


Figure 31: Percentage Change in Capacitance of Single and Dual Sided 40mm CPC.

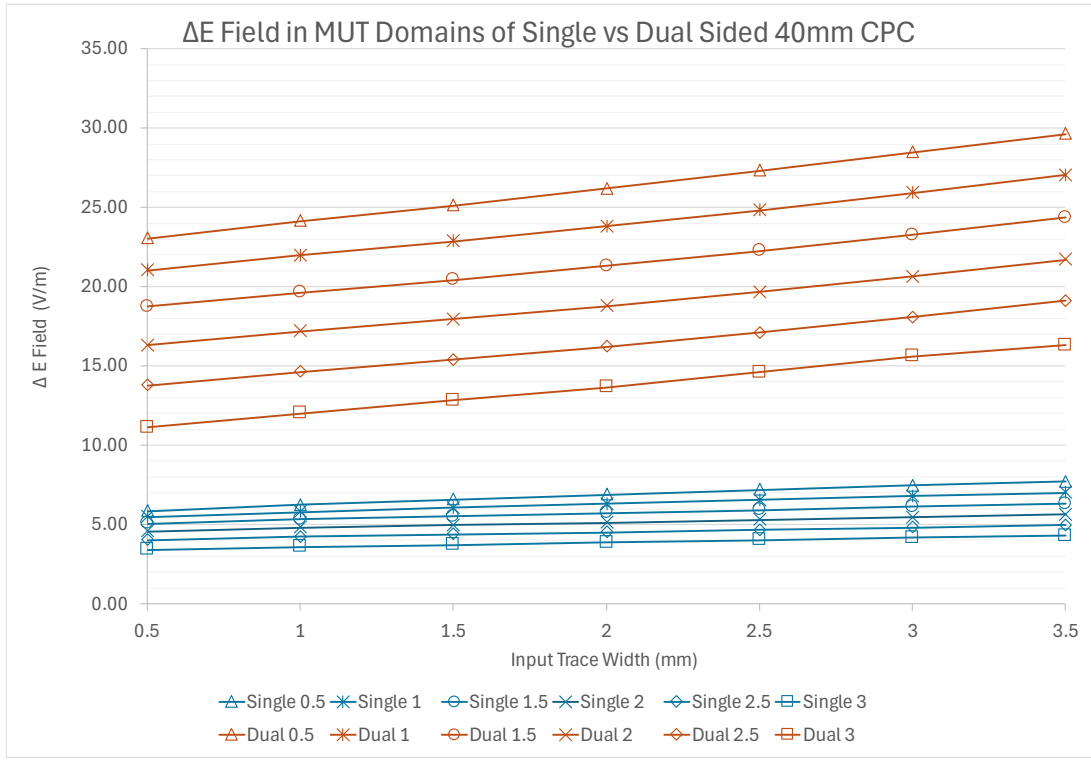


Figure 32: Change in E Field in MUT of Single and Dual Sided 40mm CPC.

The results of these simulations show the electrode mirroring technique demonstrated by Patle et al is an optimization pathway that can provide substantial improvement to the performance of a sensor for this use case. While the scalar increase in overall capacitance is a positive feature of this dataset, the substantial shift in the percentage  $\Delta C$  and  $\Delta E \text{ Field}_{MUT}$  represents a large shift in the dynamic range of the sensor. It's likely this optimization is so significant it has the potential to shift a sensor design from non-function to functional and was therefore considered a requirement to include in the design.

Note the upward shift present in the percentage  $\Delta C$  data at the maximum electrode widths of 3.5 mm input, 3 mm output was noticed during the modelling and is likely due to the inter-electrode gap width reducing to 50  $\mu\text{m}$ , a point where the resolution of the mesh used during simulation was too coarse for the geometry. This only affects this final simulation value which was identified as non-critical early in the modelling. This could have been resolved by removing the final 3.5 mm input trace simulations from the parametric sweeps, but simulations of this 3.5 mm input trace dataset for lower output trace widths was considered relevant to the modelling results. Another option would have been to increase the mesh resolution, but this would have vastly increased the computation time of each parametric sweep, which was already at approximately 25 minutes per sweep on a PC well suited to this type of workload, so leaving this point in the dataset and discussing it here was considered the most appropriate course of action.

### 5.2.5 CPC Dual Sided 40mm vs 80mm Length



Figure 33: Simulation Results of Dual Sided 80mm CPC.

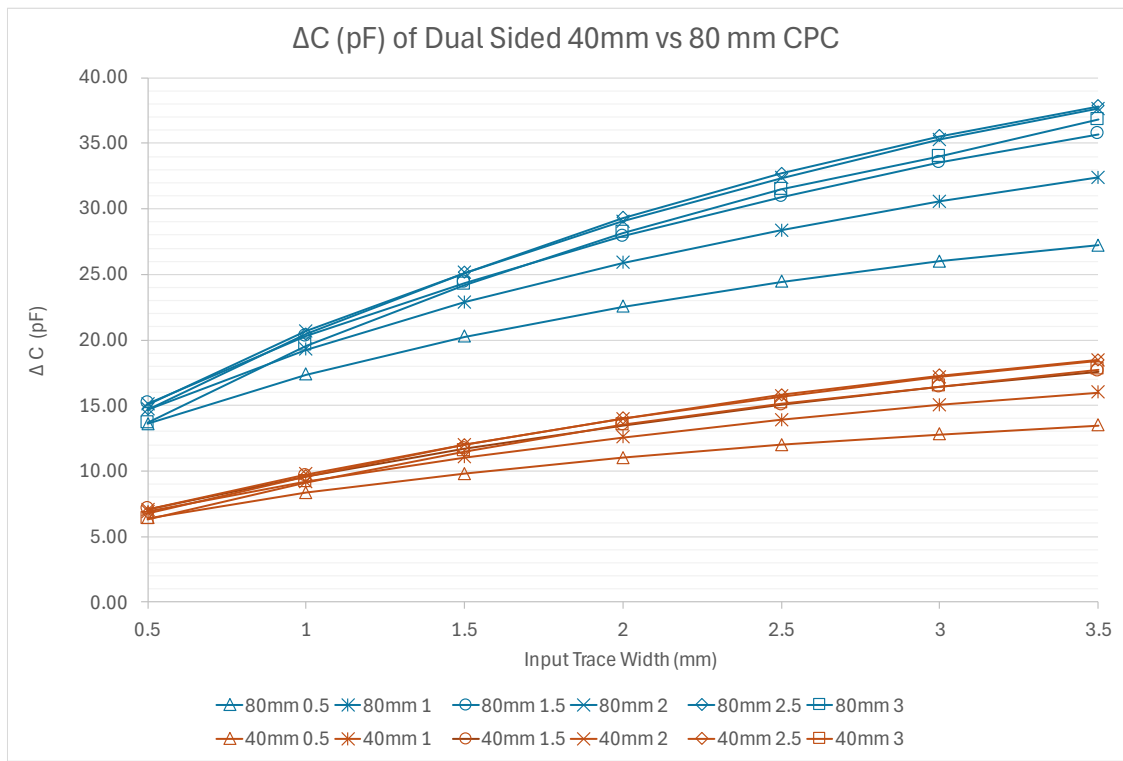


Figure 34: Change in Capacitance of Dual Sided 40mm and 80mm CPC.

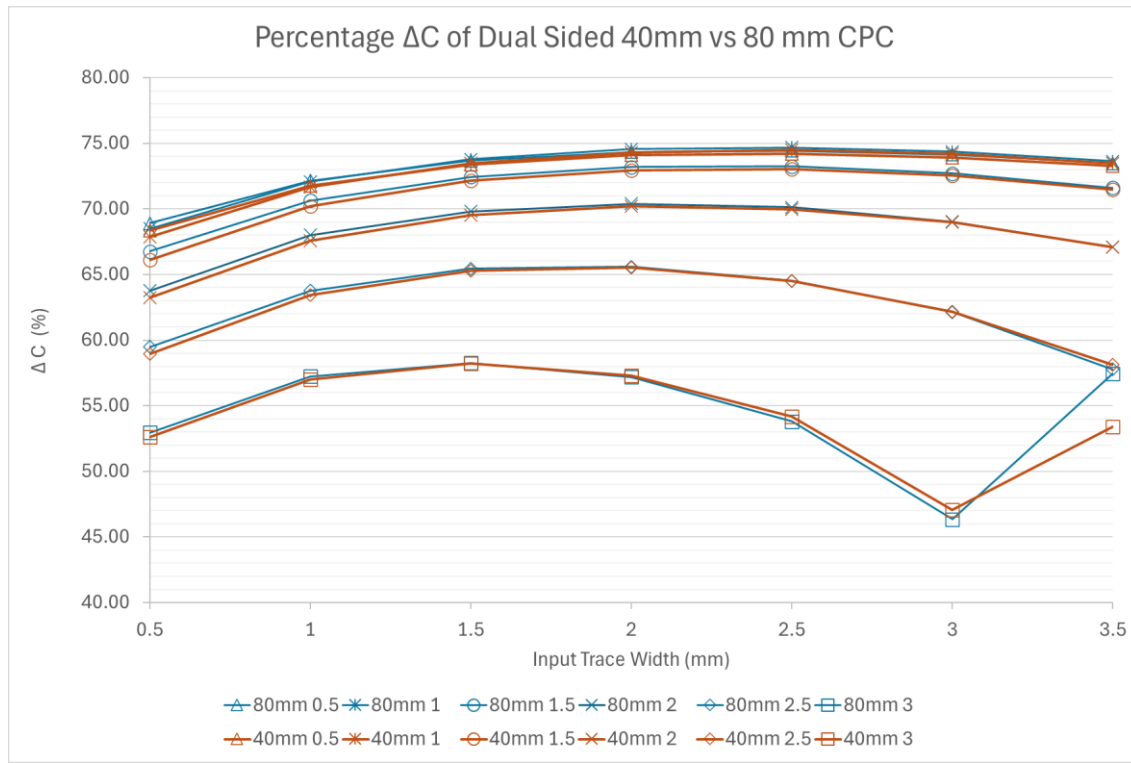


Figure 35: Percentage Change in Capacitance of Dual Sided 40mm and 80mm CPC.

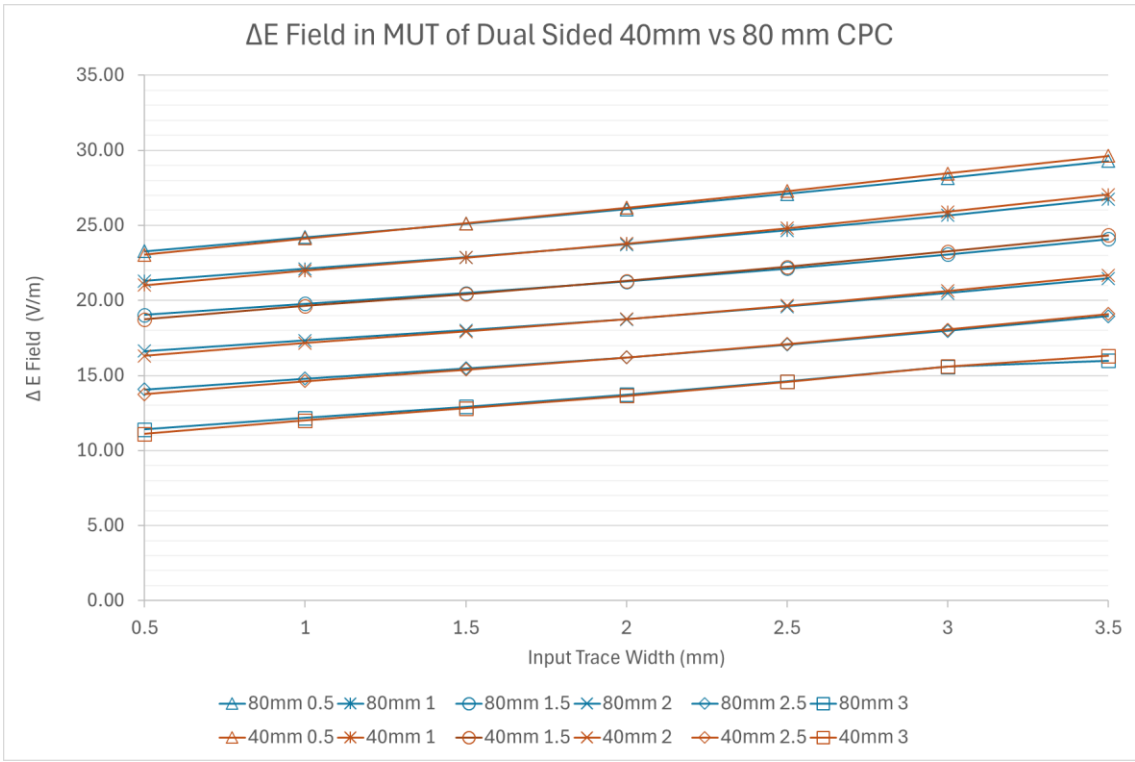


Figure 36: Change in E Field in MUT of Dual Sided 40mm and 80mm CPC.

Comparing the results of doubling the sensor length from 40 mm to 80 mm with the results from mirroring the electrodes on both sides of the PCB further demonstrate the benefits the electrode mirroring technique suggested by Patle et al has in this use-case (Patle, et al. 2022). In both optimization techniques the area of the sensor electrodes is increased by a factor of 2 (very close to 2 in the case of doubling the sensor length). However, the difference in the simulation results for the  $\Delta E$ -Field<sub>MUT</sub> and percentage  $\Delta C$  is large between the 2 optimization methods. Doubling the length of the sensor results in a doubling of capacitance, but no discernible shift in  $\Delta E$ -Field<sub>MUT</sub> or percentage  $\Delta C$ , in contrast the electrode mirroring results show large changes to these values. This is likely due to the repulsive force of like charges acting through the FR4 PCB substrate repelling the fringing field out from the PCB and into the MUT and lowering the energy present in the loss domain.

While this doubling of the sensor length is not as effective as electrode mirroring, this increase in capacitance would still be highly beneficial in a real-world implementation of a sensor array. Increasing the length to 80 mm was not done for this work only because 51 by 51 mm  $Al_2O_3$  substrates had been sourced prior to this modelling being performed. Doubling the minimum capacitance of the sensors would have simplified several aspects of this work a great deal, particularly on the signal conditioning side of the project, so a double sided 80 mm length sensor layout would likely be preferable over a 40 mm design in future work.

### ***5.2.6 Selection of Sensor Design***

The final design selected was a double-sided design of 40 mm length with an input trace width of 3 mm and an output trace width of 1.5 mm. This design was selected as it was within 2% of the maximum percentage  $\Delta C$  value for the double sided 40 mm modelling results and offered a higher minimum capacitance of 6.21 pF when compared to designs of lower output trace widths.

## ***5.3 Prototype Fabrication and Verification***

### ***5.3.1 PCB Design***

The PCB design process was initially assigned a time budget of 1 week in the Gantt chart of the mid-project progress report. This was a serious under-estimation of the time the PCB design would require, with this design process taking closer to 4 weeks to complete. It was initially assumed this would be a simple design, as all that was required was a board connector, the 4 sensors, and input and output traces, but several factors complicate the design substantially and this was not realized until the design process had begun.

The first issue was that these signal paths needed to support analogue signals in the 10 to 50 MHz band with a peak-to-peak voltage somewhere between 1 and 5 volts and exact values for these variables could not be assigned until development of the signal conditioning circuitry had progressed, so it was decided to attempt to support this entire signal range. Analogue signal paths like this complicate PCB design significantly in comparison to digital signals as they should be treated as transmission lines (Altium 2024). The next issue was that it would be desirable to incorporate waterproofing and environmental protection features directly into the PCB design to the largest extent possible. To accomplish this, it was decided to switch from a 2-layer to a 4-layer board stack-up and run the sensor traces and ground plane on internal copper layers 2 and 3. Finally, the placement of the ground plane layer in relation to the sensors had to be carefully considered to ensure sensor functionality was not impacted by the internal ground layer.

The final design can be seen in figure 37. The design ensures the MUT and sensor circuits are kept electrically isolated below the max sample depth line once the  $Al_2O_3$  substrates were fixed in place by keeping all copper on layers 1 and 4 inside the shield boundary and using vias to connect the sensors directly to the traces on layer 2. A custom footprint was also created that allows either a 2.54 mm pin header connection or SMA board edge connectors to be soldered directly to the board.

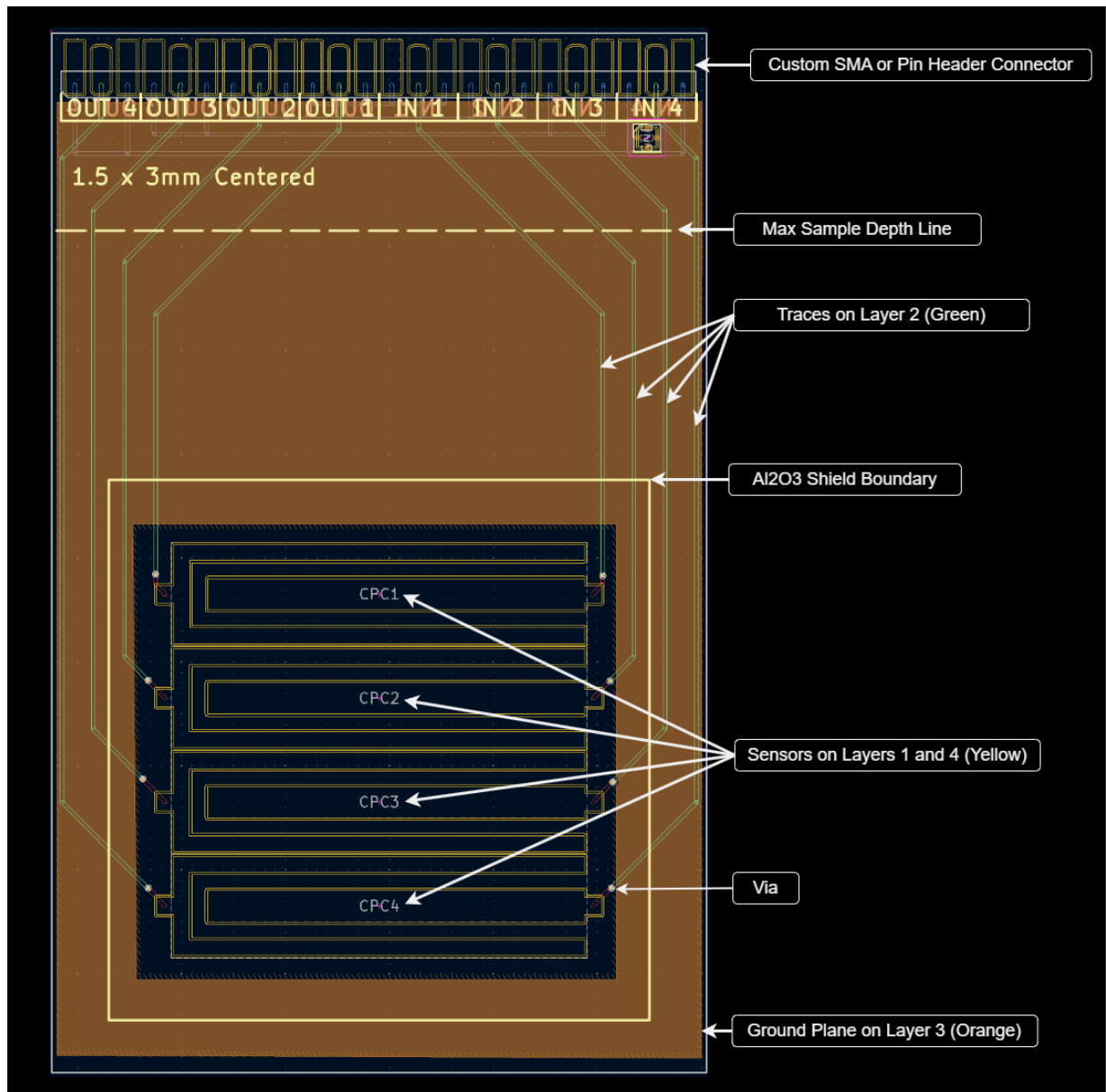


Figure 37: KiCad PCB Design of Prototype.

### 5.3.2 PCB Fabrication

Once the PCB design phase was complete the Gerber build files were generated for the design and an order was placed with the manufacturer of choice JLCPCB. A premium surface finish of Electroless Nickel Immersion Gold (ENIG) was selected for the design as this finish results in much flatter surfaces and superior corrosion resistance in comparison to Hot Air Solder Leveling (HASL) (JLCPCB 2024). The fabricated bare PCB and fully assembled sensor array prototype can be seen in figure 38.

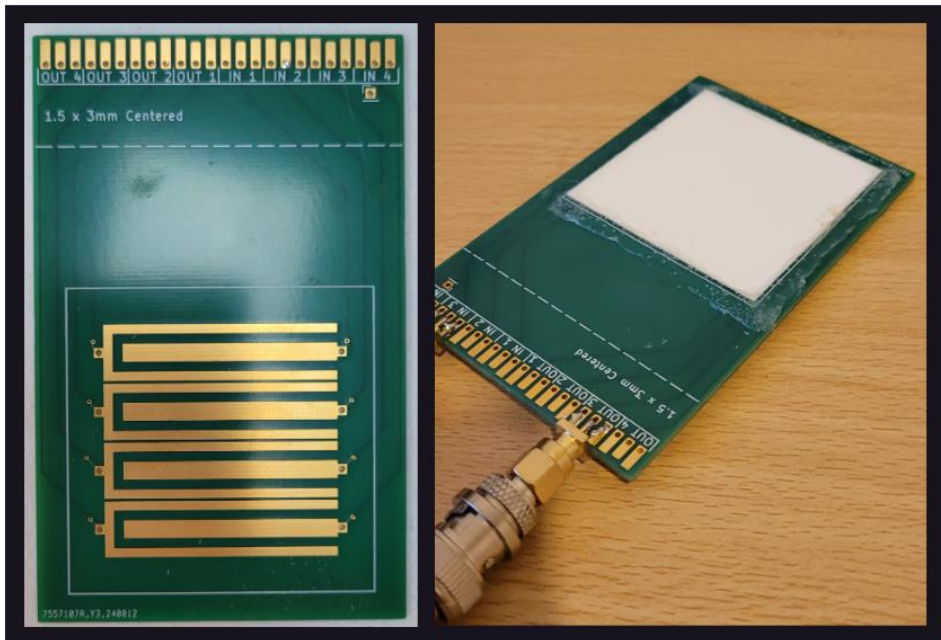


Figure 38: Bare PCB of Prototype (Left) and with Al<sub>2</sub>O<sub>3</sub> Shield Installed (Right).

### 5.3.3 Prototype Validation

Once the PCB prototypes were received, the frequency sweep process detailed in section 4.4 was performed on one of the prototype assemblies to verify the sensor arrays were functional.

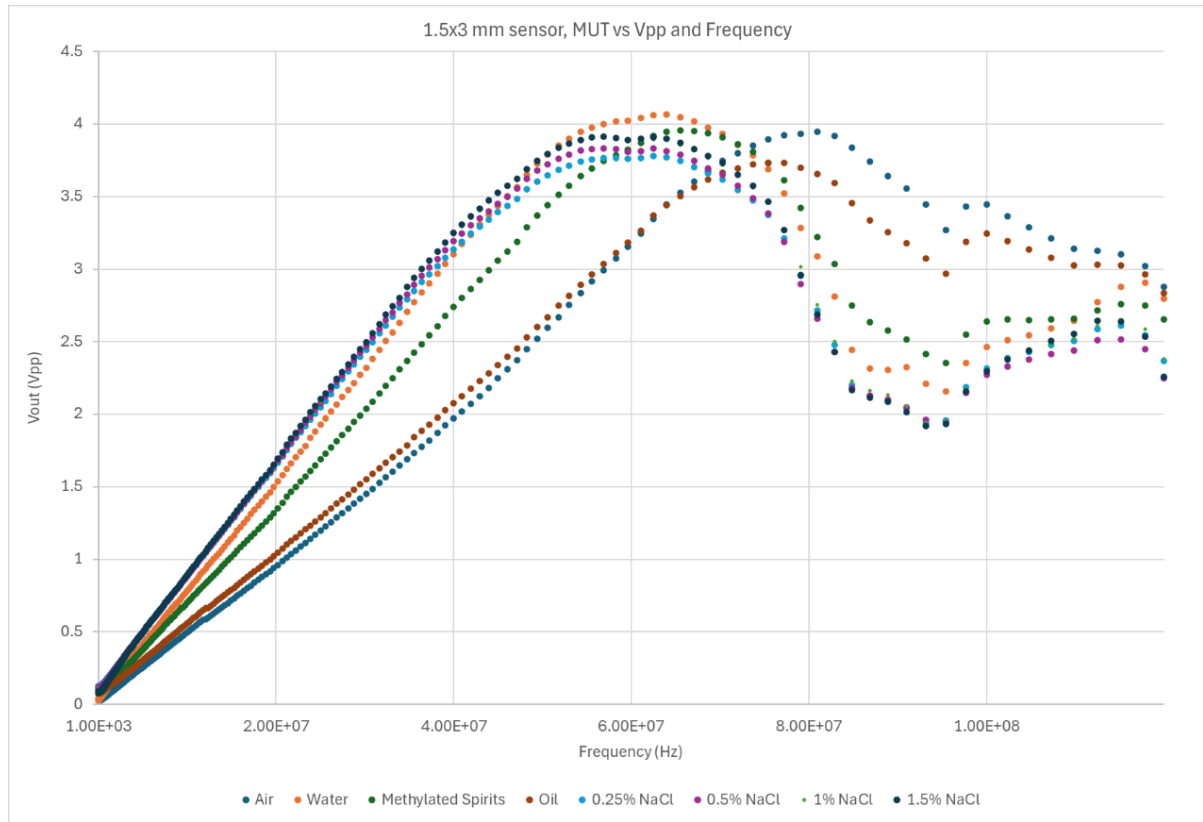
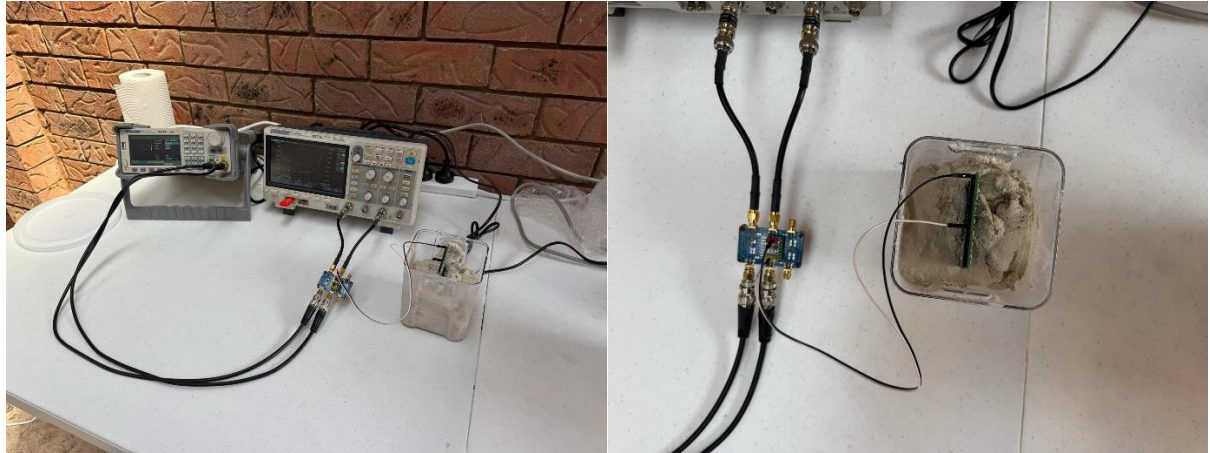


Figure 39: Results of Prototype Verification Frequency Sweep.

These results show an acceptable frequency response below 40 MHz and divergence between the MUT sample groups which appears to be acceptable for characterization.

### 5.4 Frequency Analysis of Prototype

The apparatus used for the prototype frequency analysis can be seen in figure 40 and the results of the testing can be seen in figure 41.



*Figure 40: Prototype Frequency Sweep Apparatus.*

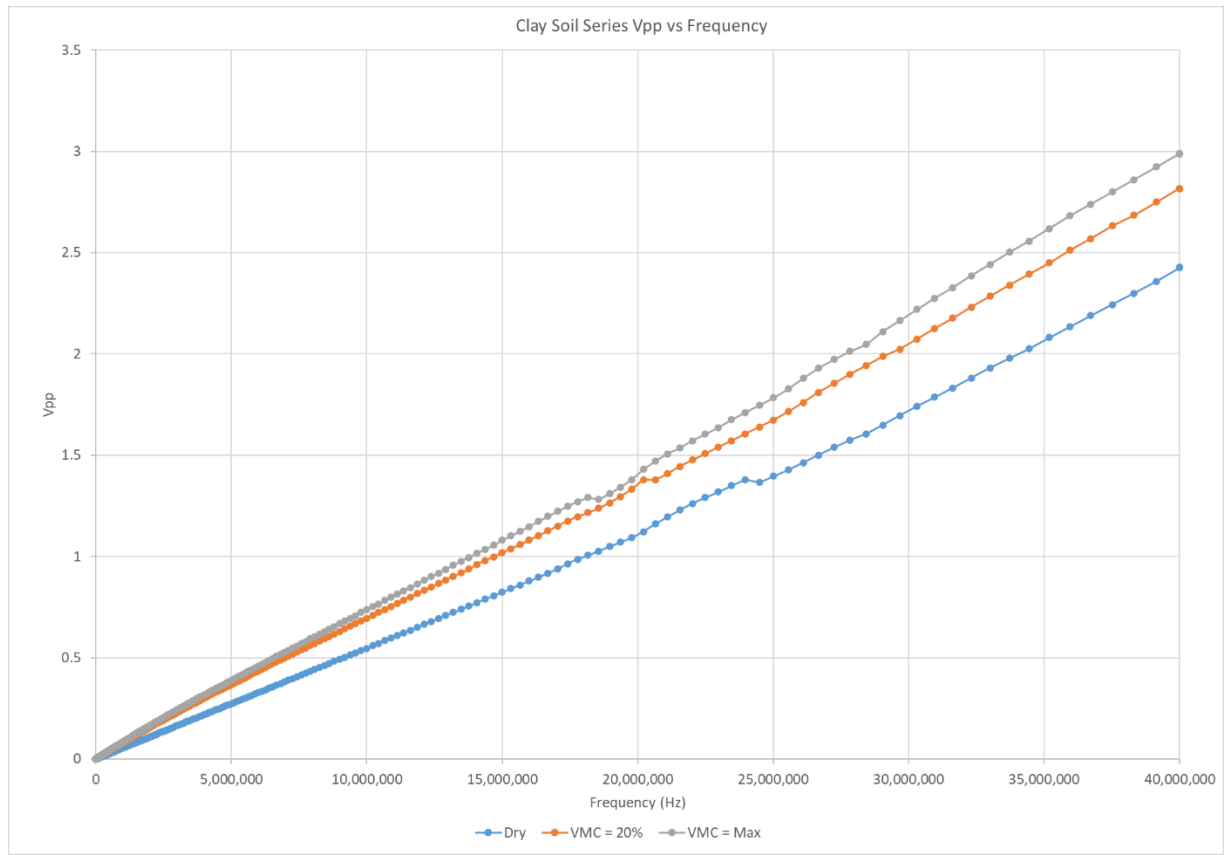


*Figure 41: Prototype Frequency Sweep Results.*

These results show several slight perturbations in the data between 15 and 30 MHz so this band was avoided. Ideally a frequency at the higher end of this band, at 40MHz, would be preferable as it would likely simplify aspects of circuit design when dealing with the low capacitance values of the sensors. However, this had to be balanced against the complexity of

the input signal generation circuitry, and after discussion with a fellow student who was working on this aspect of the project, a frequency of 10 MHz was chosen for characterization.

## 5.5 Characterization of Prototype

### 5.5.1 Initial Attempt at Characterization

The results and plot of the initial attempt at characterization of the sensor array can be seen in figures 42 and 43.

Sand Soil Series [100 : 0]										Sandy Loam Soil Series [80 : 20]											
Temp (°C)	g/litre									Temp (°C)	g/litre										
	20	1636	Sensor 1 (Top)		Sensor 2		Sensor 3		Sensor 4 (Bottom)		ml water		Sensor 1 (Top)		Sensor 2		Sensor 3		Sensor 4 (Bottom)		
ml Water	Vpp	Δt	Vpp	Δt	Vpp	Δt	Vpp	Δt	Vpp	Δt	ml water	Vpp	Δt	Vpp	Δt	Vpp	Δt	Vpp	Δt		
0	564	77	556	78	568	78	572	78	0	572	78	588	78	600	78	600	78	600	78		
40	560	78	572	78	588	78	588	78	40	560	78	596	78	604	78	612	78	612	78		
80	560	78	572	78	580	78	580	78	80	572	78	592	78	608	78	612	78	612	78		
160	556	78	572	78	588	78	588	78	120	588	79	592	78	600	78	604	78	604	78		
240	564	78	576	78	588	78	596	78	160	588	79	600	79	612	79	612	79	612	79		
320	564	78	580	78	596	78	600	78	200	600	79	608	79	624	79	628	79	628	79		
400	572	78	580	78	592	78	596	78	240	604	79	612	79	620	79	632	79	632	79		
480	572	78	584	78	592	78	600	78	280	620	79	628	79	644	79	644	79	644	79		
560	580	78	596	78	604	78	604	78	300	628	79	644	79	652	79	648	79	648	79		
640	676	78	672	78	676	78	684	78	320	620	79	636	79	644	79	652	79	652	79		
									340	636	79	650	79	668	79	676	79	676	79		
									380	636	80	652	80	668	80	684	80				
									400	644	80	652	80	668	80	680	80				
									420	644	80	660	80	676	80	684	80				
									440	644	80	652	80	660	80	684	80				
									480	660	80	668	80	676	80	684	80				
									520	676	80	676	80	692	80	700	80				
									560	644	81	676	80	692	80	708	80				
									600	676	80	680	80	692	80	708	80				
									640	676	80	684	80	700	80	716	80				
									680	676	80	676	80	700	80	724	80				
									720	692	80	680	80	708	80	732	80				
									740	692	80	700	80	712	80	740	80				
									800	688	80	700	80	716	80	748	80				
Sandy Clay Soil Series [60 : 40]										Clay Soil Series [40 : 60]											
Temp (°C)	g/litre										Temp (°C)	g/litre									
	20	1400	Sensor 1 (Top)		Sensor 2		Sensor 3		Sensor 4 (Bottom)			19.6	900	Sensor 1 (Top)		Sensor 2		Sensor 3		Sensor 4 (Bottom)	
ml water	Vpp	Δt	Vpp	Δt	Vpp	Δt	Vpp	Δt	Vpp	Δt	ml Water	Vpp	Δt	Vpp	Δt	Vpp	Δt	Vpp	Δt		
0	568	78	580	78	596	78	600	78	0	548	78	576	78	588	78	588	78	588	78		
40	564	78	580	78	604	78	600	78	200	532	81	588	79	604	79	612	80				
80	564	78	588	78	596	78	596	78	240	620	80	636	79	628	79	656	79				
120	580	79	588	79	604	79	604	79	280	716	80	720	80	716	80	700	80				
160	628	79	628	79	632	79	628	79	300	692	80	704	80	724	80	748	80				
200	604	79	620	79	632	79	644	79	320	764	80	764	80	776	80	800	80				
220	636	80	640	80	648	80	652	80	340	724	80	700	82	756	80	772	80				
240	644	81	644	80	660	80	676	80	360	732	80	740	80	788	80	800	80				
260	660	81	676	81	668	80	652	80	380	748	80	744	80	732	81	780	81				
280	648	80	668	81	660	80	676	80	400	748	81	748	80	788	80	808	80				
300	676	80	692	81	688	80	700	80	420	764	80	792	81	804	81	820	82				
320	692	80	700	81	692	80	708	81	440	804	81	716	84	780	82	788	83				
340	692	80	700	81	700	81	712	81	460	780	81	772	81	792	81	812	81				
360	708	81	672	81	700	81	716	81	480	840	81	828	81	820	82	864	82				
380	724	81	724	80	724	80	740	81													
400	708	81	724	80	732	80	756	81													
420	712	81	716	80	724	80	744	80													
440	716	80	716	80	724	80	748	80													
460	704	80	708	80	716	80	740	80													
480	720	80	720	80	716	80	724	81													
500	708	80	712	80	724	80	740	80													
540	712	80	712	80	720	80	744	80													

Figure 42: Table of Results from Initial Attempt at Characterization.

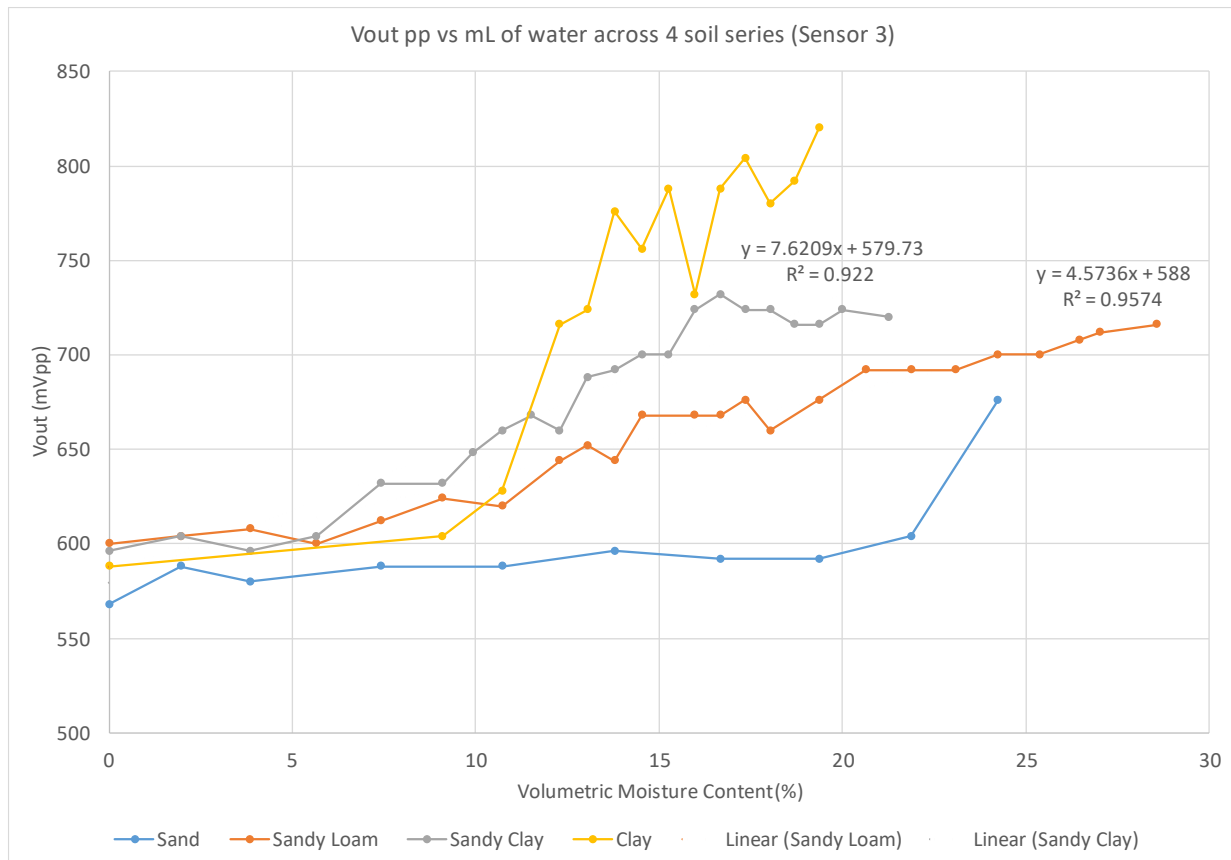


Figure 43: Plot of First Attempt at Characterization.

The initial attempt at characterization uncovered some significant unforeseen factors that can have a large impact on results. The amount of water that was required to allow mixtures to be fully incorporated varied greatly between the soil series, increasing from approximately 80 ml for the sand, sandy loam and sandy clay series to 200 ml for the clay series. As the clay percentage of soil series increased the water and clay in the samples tended to bind into small balls which made even incorporation impossible at these moisture levels.

Two major sources of experimental noise were identified in this data. Towards the end on the experiment while measuring the Clay soil series the connector and wires used to connect the sensors to the SMA test fixture board started to wear and the quality of the connection degraded noticeably. This connection was made with standard 2.54 mm pin headers and individual wire connectors for sensor input and output. As these cables were not fixed in relation to each other and were not shielded the inductive properties of the cables was variable, it's likely these inductive effects also contributed to noise in the data. The final issue identified during this testing which leads to high variability of readings is not easily resolved. The largest cause of loss of accuracy for stationary capacitive soil moisture sensors is air gaps getting trapped between the sensor and soil during installation (Meter Group n.d.). While carrying out this experiment the sensor must be reinserted for every measurement, resulting in inherent variability of the results due to the nature of how the samples must be prepared. The level of compaction of the soil around the sensor can change the voltage output significantly. This was remedied by attempting to compact the soil around the sensor to a similar degree with each measurement, but due to the change in viscosity of the samples as VMC increased this was not a precise operation, so some noise is expected when using this characterization method. While there is a great deal of noise in the clay soil series due to the connector issue discussed above, the results for the Sandy Loam and Sandy Clay datasets show linear fits with good  $R^2$  values of 0.9574 and 0.922 respectively.

As the data in the Sandy Loam series was considered the most reliable, this dataset was used to examine the sensor-to-sensor variability (Figure 44).

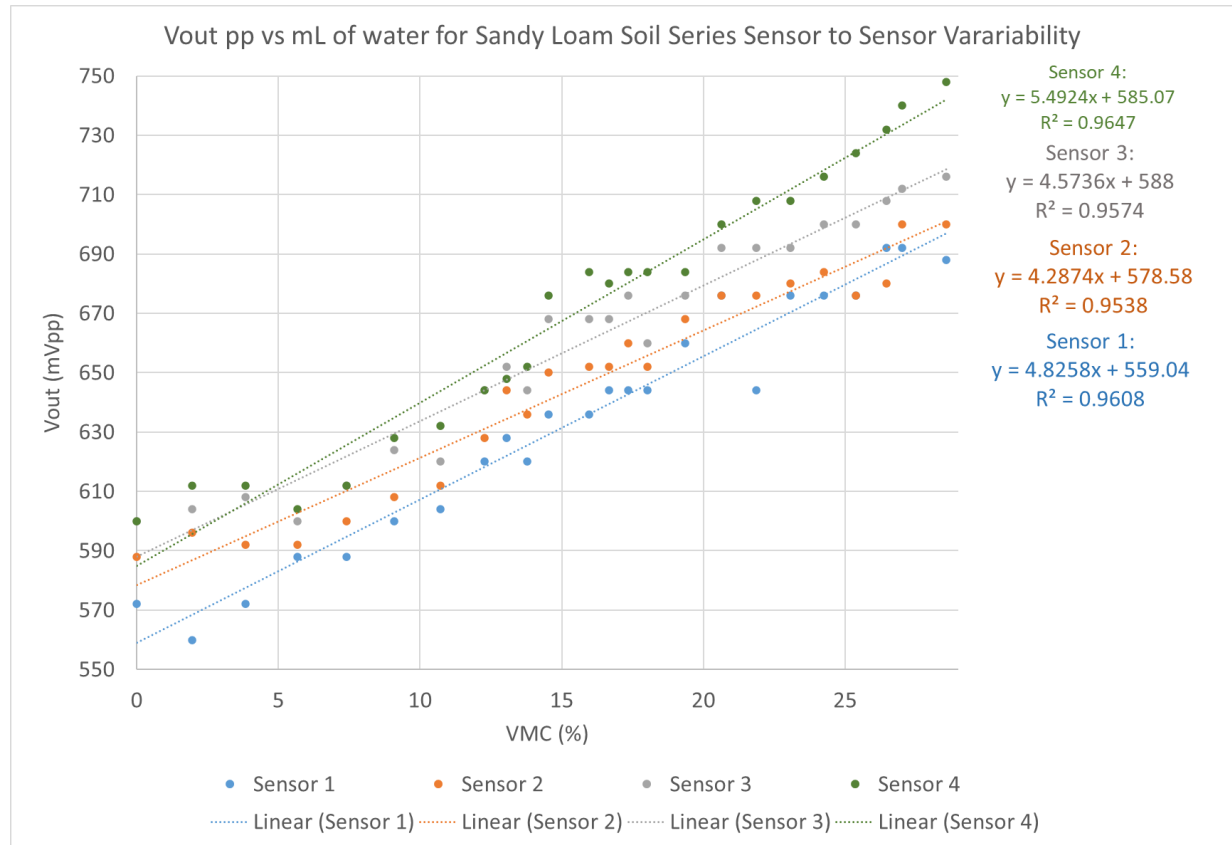


Figure 44: Examination of Sensor-to-Sensor Variability for Sandy Loam Dataset.

Notice in this data, the linear approximations appear to be divisible into 2 distinct sub-sets based on their derivatives, with sensors 1 and 4 in one sub-set exhibiting a steeper slope than sensors 2 and 3 in a second sub-set. This was an expected feature of this data and was hypothesized during the literature review. It is also the reason that an array of 4 sensors was selected for the prototype. Figure 45 is from the paper by Claudel et al on the optimization of IDC sensors. The model discussed in this paper, although targeted towards IDC sensor optimization, separates digit capacitance models into edge digits ( $C_E$ ) and internal digits ( $C_I$ ) to account for the lack of a conductor on one side of the edge digits (Claudel, et al. 2021). It is likely a similar effect is occurring here, with the sensors at the top and bottom of the array exhibiting slightly different responses to those in the centre. It's possible that the addition of copper strips at floating potential at the top and bottom of the array could resolve this difference between these sets. If this method proved

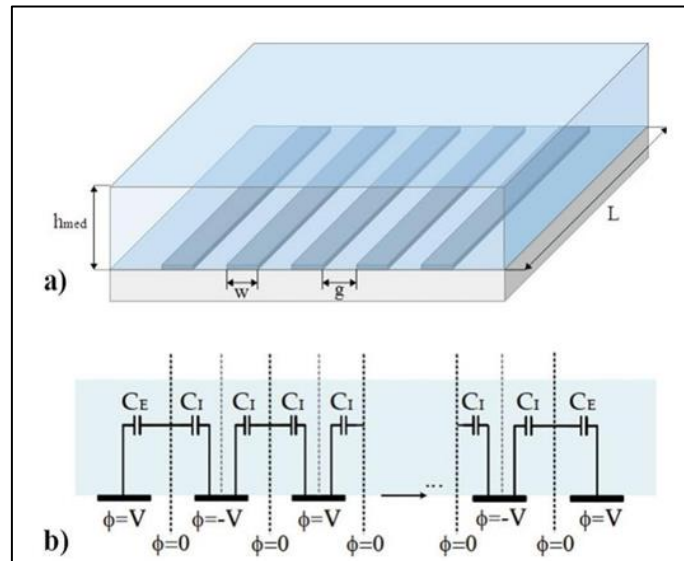


Figure 45: IDC Optimization Model Parameters (Claudel, et al. 2021).

unsuccessful, slightly different models for internal and external sensors could be used. The shift in Y-intercept of these models is likely due to the additional capacitance from the extra trace length required in the PCB for sensors lower in the array (see figure 37). It's likely these could be bought closer inline by length matching all sensor traces during the PCB design.

### *5.5.2 Updates to Characterization Methodology*

The large spike in voltage of the sand series between 20 and 25% VMC which is visible in figure 43 is due to a known moisture repellent property of high sand percentage soils. Below approximately 5% clay content, it is a common practice in the Australian agricultural industry to add clay to these sand soils to negate this water repellent effect (GRDC 2015). This data series was removed from the sample groups and replaced with 2 addition sand-clay mixtures as these were considered more relevant for this use-case. The updated sample groups for the second characterization attempt were:

1. *Sandy Loam [80 : 20],*
2. *Sandy Clay Loam [70 : 30],*
3. *Sandy Clay 1 [60 : 40],*
4. *Sandy Clay 2 [50 : 50],*
5. *Clay [40 : 60]*

To improve the stability of the sensor connections a perf-board PCB and 2 coaxial SMA connectors were added to the top of the sensor array and connected directly to the signal generator and oscilloscope allowing the test fixture board to be removed entirely. This setup provides fixed geometry for all unshielded sections of the signal path and the improvement in signal stability was visually noticeable on the oscilloscope screen once this alteration was carried out. Finally, the master mixtures of sand and clay were reduced to 1 litre to conserve these materials in case future attempts at characterization would be conducted.

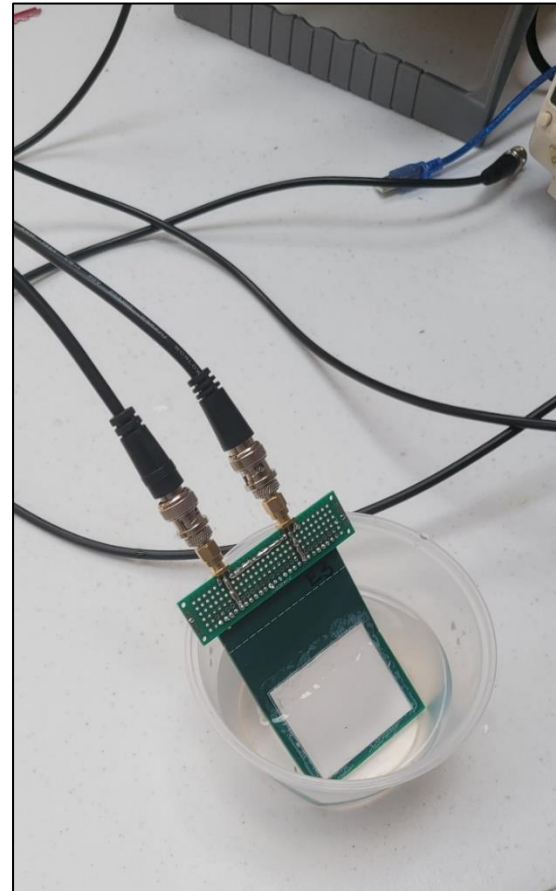


*Figure 46: Revised Sensor Connection Method.*

### 5.5.3 Second Attempt at Characterization

The table and plot below show the results from the second attempt at characterization of the sensor array.

Sandy Loam			Sandy Clay Loam			Sandy Clay 1			Sandy Clay 2			Clay			
S [80 : 20] C			S [70 : 30] C			S [60 : 40] C			S [50 : 50] C			S [40 : 60] C			
T (°C)	1L Mass		T (°C)	1L Mass		T (°C)	1L Mass		T (°C)	1L Mass		T (°C)	1L Mass		
19.4	1400		18.8	1271		19.2	1163		19.2	1107		19.2	963		
ml water	Sensor 3		ml water	Sensor 3		ml Water	Sensor 3		ml Water	Sensor 3		ml Water	Sensor 3		
	Vpp	VMC (%)		Vpp	VMC (%)		Vpp	VMC (%)		Vpp	VMC (%)		Vpp	VMC (%)	
0	0.34	0.00	0	0.34	0.00	0	0.336	0.00	0	0.34	0.00	0	0.34	0.00	
40	0.34	3.85	40	0.344	3.85	40	0.34	3.85	40	0.348	3.85	40	0.346	3.85	
80	0.348	7.41	80	0.356	7.41	80	0.352	7.41	80	0.356	7.41	80	0.348	7.41	
100	0.356	9.09	100	0.354	9.09	100	0.38	9.09	100	0.372	9.09	100	0.364	9.09	
120	0.376	10.71	120	0.38	10.71	120	0.404	10.71	120	0.388	10.71	120	0.4	10.71	
140	0.388	12.28	140	0.416	12.28	140	0.404	12.28	140	0.428	12.28	140	0.456	12.28	
160	0.396	13.79	160	0.436	13.79	160	0.46	13.79	160	0.444	13.79	160	0.484	13.79	
180	0.404	15.25	180	0.444	15.25	180	0.472	15.25	180	0.46	15.25	180	0.508	15.25	
200	0.428	16.67	200	0.456	16.67	200	0.48	16.67	200	0.492	16.67	200	0.52	16.67	
220	0.436	18.03	220	0.46	18.03	220	0.484	18.03	220	0.508	18.03	220	0.524	18.03	
240	0.444	19.35	240	0.468	19.35	240	0.488	19.35	240	0.512	19.35	240	0.524	19.35	
260	0.452	20.63	260	0.472	20.63	260	0.492	20.63	260	0.512	20.63	260	0.524	20.63	
280	0.46	21.88	280	0.476	21.88	280	0.492	21.88	280	0.512	21.88	280	0.524	21.88	
300	0.472	23.08	300	0.484	23.08	300	0.492	23.08	300	0.512	23.08	300	0.524	23.08	

Figure 47: Table of Results for Second Attempt at Characterization.

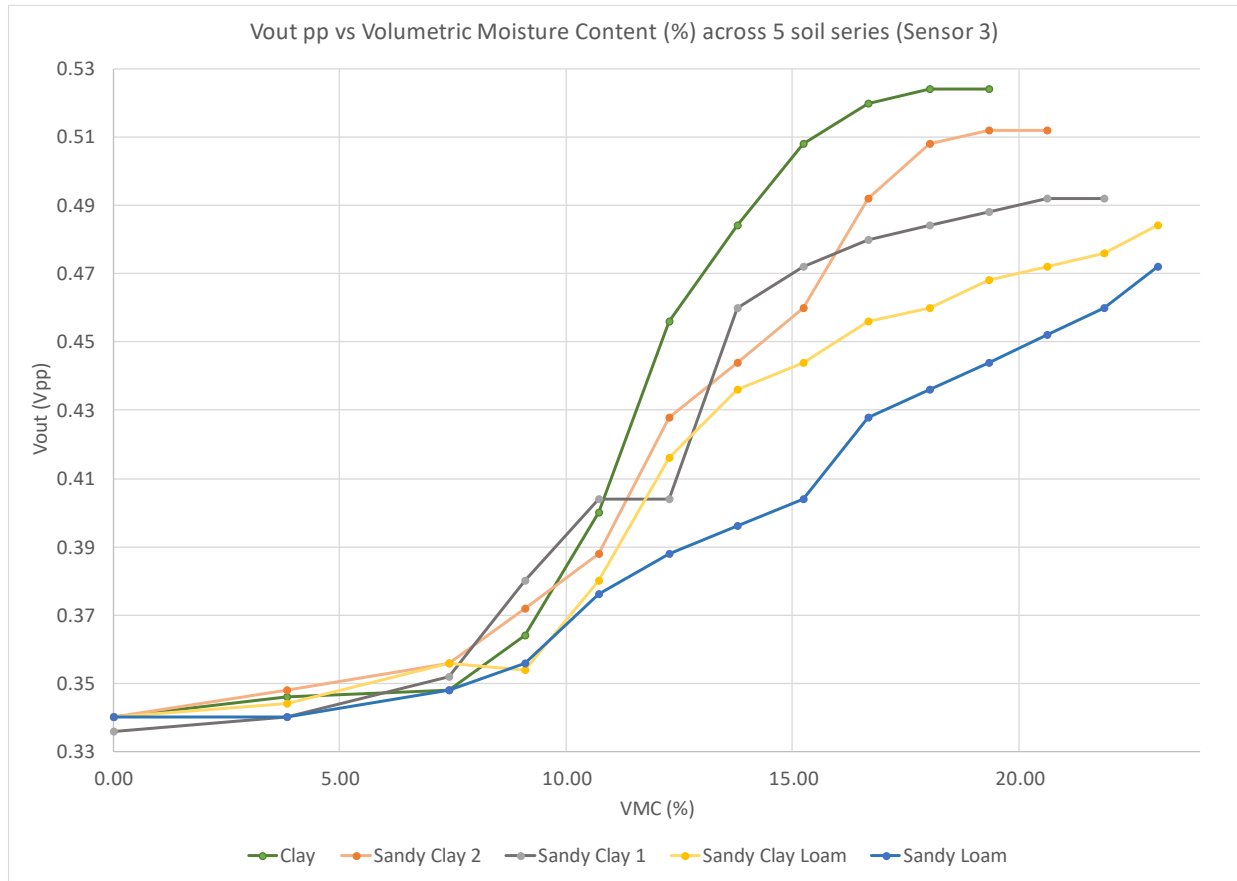


Figure 48: Plot of Second Attempt at Characterization.

The first thing to note with these results in comparison to the initial characterization method is the significant drop in  $V_{out\ pp}$  between the two attempts. This is likely due to the updated

connection method altering the parasitic inductive effects present in the cable. There is still some noise present in this data, with an obvious outlier in the Sandy Clay 1 dataset between 10 and 15 % VMC, this is likely due to the sensor insertion issues discussed in the previous section. The relationship between  $V_{out\ pp}$  and VMC in this data appears to follow a sigmoid-like relationship which increases in prominence as the clay content of the soil is increased. After further research into what might be causing the relationship seen in this data, it is hypothesized that the lowering of the porosity of the soil samples as the clay content increases may be a factor affecting the results of this method of characterization (Mukhlisin and Saputra 2013). Unfortunately, this parameter was not considered until very late in the project after this data had been gathered and analysed, so further work is required for a full characterization of the sensor.

## 6. Conclusions

While the results of this work have provided some insight into the viability of a sensor array design for use in real time measurement of soil moisture during moisture seeking operations, the design presented is a long way from being shown to be suitable for this use-case. The initial investigation phase of this experiment identified  $Al_2O_3$  as a material that may be suitable, and the results of this work have shown that sensing is possible through 0.5 mm shields made of this material, but the ability of this material to withstand the severe mechanical constraints of this environment were outside the scope of this work. Until these aspects are studied the efficacy of the presented design remains unknown.

The results of the comparisons between IDC and CPC sensor designs carried out during the investigation and modelling phases have demonstrated that CPC designs offer superior functionality in this sensing domain due to the requirement that sensor signals can penetrate the shield layer while and still provide usable output. The modelling phase of this work has also demonstrated the benefits of the electrode mirroring technique described by Patle et al to be a significant optimization for this use-case, offering substantial benefits over increases in sensor length. Increasing the length of the sensor array to 80 mm in addition to mirroring electrodes would likely result in a superior design than the 40 mm prototype tested in this work as this change would likely assist in alleviating some of the issues experienced during this work due to the low capacitance values of the prototype.

The PCB design for the prototype, while taking much longer than expected, caused no issues through testing, demonstrating the method of running all traces on internal copper layers was robust enough to handle the harsh environment the array must handle during characterization. Using shielded coaxial cables and connectors to connect sensors with dedicated transmission lines proved far superior to standard pin header connections.

While the characterization did demonstrate the sensor array is capable of measuring changes in soil moisture, the characterization methodology requires significant adjustment before a full characterization of the sensors can be carried out reliably. Characterization would likely be far more successful if performed at a stage in development when the signal generation, signal conditioning, and sensing pipeline was finalized. As both aspects were being developed concurrently throughout this work, the inter-dependencies of both aspects resulted in many parameters remaining unknown until late in the development cycle.

## **7. Future Work**

### ***7.1 Evaluation of Mechanical Performance of Shield in Real-World Environment***

While this work has demonstrated a design that satisfies the electromagnetic requirements, the mechanical performance has not been examined. This aspect of the design is critical to achieving functionality of a sensor array in this environment and will require examination.

### ***7.2 In-Depth Characterization of Sensor Response to Soil Texture***

While an attempt was made to characterize the clay and sand components in this work, the presented method requires further work, and the silt component has not been examined. An in-depth analysis of these relationships will be required for any design to perform reliably in this sensing domain.

### ***7.3 Examination of Lower Frequency Sensor Response to Characterize Conductivity***

Although beyond the scope of this work, the dual frequency approach to characterizing both the real and imaginary sides by measuring the conductivity at low frequency and permittivity at high frequency described by Escriba et al and Rêgo Segundo et al would likely lead to better characterization results of the sensors. Characterization of these aspects of a design would likely be beneficial to the performance of designs for this use-case.

## References

- Accuratus. 2013. “Aluminium Oxide Ceramic Properties.” <https://accuratus.com/>.  
<https://accuratus.com/alumox.html>.
- Altium. 2024. “Stripline vs Microstrip: PCB Routing Differences and Guidelines.” [resources.altium.com](https://resources.altium.com/p/stripline-vs-microstrip-understanding-their-differences-and-their-pcb-routing-guidelines). <https://resources.altium.com/p/stripline-vs-microstrip-understanding-their-differences-and-their-pcb-routing-guidelines>.
- Arcone, Steven, Steven Grant, Ginger Boitnott, and Benjamin Bostick. 2008. “Complex permittivity and clay mineralogy of grain-size fractions in a wet silt soil.” *Geophysics* 73: J12. doi:10.1190/1.2890776.
- Ausplow. 2024. “SOIL HEALTH AN AGENDA ITEM.” *Ausplow*.  
<https://www.ausplow.com.au/soil-health-an-agenda-item/>.
- Bilskie, Jim. 2001. “Soil water status: content and potential.” *campbellsci.com*.  
<https://s.campbellsci.com/documents/us/technical-papers/soilh20c.pdf>.
- Bodini, A, E Sardini, M Serpelloni, and S Pandini. 2018. “Novel Coplanar Capacitive Force Sensor for Biomedical Applications: A Preliminary Study. .” *Sensors* 329-336.  
doi:[https://doi.org/10.1007/978-3-030-04324-7\\_41](https://doi.org/10.1007/978-3-030-04324-7_41).
- China Alumina Ceramic. 2022. “ALUMINA CERAMIC PLATE.”  
<https://www.aluminaceramicball.com/>.  
<https://www.aluminaceramicball.com/product/alumina-ceramic-plate/>.
- Claudel, J, A L Alves de Araujo, D Kourtiche, M Nadi, and A Bourjilat. 2021. “Optimization of Interdigitated Sensor.” *Interdigital Sensors* 36: 91-122.  
doi:[https://doi.org/10.1007/978-3-030-62684-6\\_5](https://doi.org/10.1007/978-3-030-62684-6_5).
- Congreve, Mark. 2022. *Paddock Practices: Dry sowing and pre-emergent herbicides*. GRDC.  
<https://grdc.com.au/resources-and-publications/all-publications/paddock-practices/2022/national/march/dry-sowing-and-pre-emergent-herbicides>.
- Dean, Robert N, Aditi Rane, Michael Baginski, Zane Hartzog, and David J Elton. 2010. “Capacitive fringing field sensors in printed circuit board technology.” *2010 IEEE Instrumentation & Measurement Technology Conference Proceedings*. Austin, TX, USA: IEEE. 970-974. doi:10.1109/IMTC.2010.5488058.
- Department of Primary Industries. 2024. “Western Australian Crop Sowing Guide.”  
*agric.wa.gov.au*.  
<https://www.agric.wa.gov.au/sites/gateway/files/Crop%20Sowing%20Guide%202024%20-%20full%20guide.pdf>.
- Disco Technology. n.d. “Co-fired Ceramics.” <https://technology.discousa.com/>.  
<https://technology.discousa.com/material/ceramics/#:~:text=HTCC%20is%20a%20ceramic%20based,is%20also%20called%20glass%20ceramics>.
- Dong, Xiaobo, and Yu-Hsing Wang. 2008. “The Effects of the pH-influenced Structure on the Dielectric Properties of Kaolinite–Water Mixtures.” *Soil Science Society of America Journal* 72: 1532-1541. doi:10.2136/sssaj2007.0238.
- Electronics Tutorials. 2024. <https://www.electronics-tutorials.ws/>. [https://www.electronics-tutorials.ws/capacitor/cap\\_1.html](https://www.electronics-tutorials.ws/capacitor/cap_1.html).
- Escriba, Christophe, Eli Gabriel Avina Bravo, Julien Roux, Jean-Yves Fourniols, Michel Contardo, Pascal Acco, and Georges Soto-Romero. 2020. “Toward Smart Soil Sensing in v4.0 Agriculture: A New Single-Shape Sensor for Capacitive Moisture and Salinity Measurements.” *Sensors* 20: 6867. doi:<https://doi.org/10.3390/s20236867>.
- Fernandez, Diego P, Y Mulev, A.R.H. Goodwin, and J.M.H. Levent Sengers. 1995. “A database for the static dielectric constant of water and steam.” Thermophysics division, National Institute of Standards and Technology, Gaithersburg, 35.  
<https://www.nist.gov/document/jpcrd487pdf>.

- Finlay, David, and Gordon Howard. 2024. *Integrating soil moisture sensor technology into seeding equipment to optimise seeding depth and crop establishment*. Moisture Planting Technologies Pty Ltd, GRDC, 1-6.  
[https://grdc.com.au/\\_\\_data/assets/pdf\\_file/0032/597236/Paper-Finlay-David-2024.pdf](https://grdc.com.au/__data/assets/pdf_file/0032/597236/Paper-Finlay-David-2024.pdf).
- González, Gabriel, Eleazar Samuel Kolosovas-Machuca, Edgar López-Luna, Heber Hernández-Arriaga, and Francisco Javier González. 2015. “Design and Fabrication of Interdigital Nanocapacitors Coated with HfO<sub>2</sub>.” *sensors* 15: 1998-2005. doi:10.3390/s150101998.
- GRDC. 2015. “CLAY SPREADING AND DELVING IN LIGHT, SANDY SOILS.” [grdc.com.au](https://grdc.com.au/__data/assets/pdf_file/0027/142587/grdc-fs-clayspreadingdelving-south_lr-pdf.pdf). [https://grdc.com.au/\\_\\_data/assets/pdf\\_file/0027/142587/grdc-fs-clayspreadingdelving-south\\_lr-pdf.pdf](https://grdc.com.au/__data/assets/pdf_file/0027/142587/grdc-fs-clayspreadingdelving-south_lr-pdf.pdf).
- GRDC. n.d. “MANAGING SOIL WATER TO IMPROVE GRAIN PROFITS.” 1-6. [https://grdc.com.au/\\_\\_data/assets/pdf\\_file/0036/287892/Managing-Soil-Water-Central-Queensland.pdf](https://grdc.com.au/__data/assets/pdf_file/0036/287892/Managing-Soil-Water-Central-Queensland.pdf).
- GRDC. 2024. “Trials to dive deep into moisture-seeking wheats.” <https://groundcover.grdc.com.au/>. <https://groundcover.grdc.com.au/crops/cereals/trials-to-dive-deep-into-moisture-seeking-wheats>.
- GRDC. 2016. “WHEAT PLANT GROWTH AND PHYSIOLOGY.” 1-10. [https://grdc.com.au/\\_\\_data/assets/pdf\\_file/0028/373906/GrowNote-Wheat-South-04-Physiology.pdf](https://grdc.com.au/__data/assets/pdf_file/0028/373906/GrowNote-Wheat-South-04-Physiology.pdf).
- Innovacera. 2023. “Do you know the difference between HTCC and LTCC?” <https://www.innovacera.com/>. <https://www.innovacera.com/news/do-you-know-the-difference-between-htcc-and-ltcc.html>.
- JLCPCB. 2024. “JLCPCB Surface Finish.” *JLCPCB.com*. <https://jlcpb.com/help/article/jlcpb-surface-finish>.
- JLCPCB. 2024. *PCB Manufacturing & Assembly Capabilities*. <https://jlcpb.com/capabilities/pcb-capabilities>.
- Kim, Man-Il, Byung-Gon Chae, and Makoto Nishigaki. 2008. “Evaluation of geotechnical properties of saturated soil using dielectric responses.” *Geosciences* 83-93. doi:10.1007/s12303-008-0010-0.
- Kyocera. 2024. “Fine Ceramics Material Characteristic Table-Alumina.” *Kyocera Global*. <https://global.kyocera.com/prdct/fc/material-property/material/comparison/index.html>.
- Li, Chuanlan, Changying Wu, and Lifei Shen. 2022. “Complex Permittivity Measurement of Low-Loss Anisotropic Dielectric Materials at Hundreds of Megahertz.” *electronics* 11: 2. doi:<https://doi.org/10.3390/electronics11111769>.
- Li, Fangxin, Yangong Zheng, Changzhou Hau, and Jiawen Jian. 2019. “Gas Sensing by Microwave Transduction: Review of Progress and Challenges.” *Frontiers in Materials* 6: 4. doi:10.3389/fmats.2019.00101.
- Llewellyn, Rick, and Jackie Ouzman. 2020. “Conservation agriculture in Australia: 30 years on.” 22.
- Meter Group. n.d. “Soil moisture sensors—How they work. Why some are not research grade.” *metergroup.com*. <https://metergroup.com/measurement-insights/soil-moisture-sensors-how-they-work-why-some-are-not-research-grade/>.
- MIT. n.d. “Capacitance and Dielectrics .” <https://web.mit.edu/>. [https://web.mit.edu/8.02t/www/802TEAL3D/visualizations/coursenotes/modules/guide\\_05.pdf](https://web.mit.edu/8.02t/www/802TEAL3D/visualizations/coursenotes/modules/guide_05.pdf).
- Mukhlisin, Muhammad, and Almshfi Saputra. 2013. “Performance Evaluation of Volumetric Water Content and Relative Permittivity Models.” *ScientificWorldJournal* 1-7. doi:10.1155/2013/421762.

- Nguyen, Manh Duc, Romulus Costache, An Ho Sy, Hassan Ahmadzadeh, Hiep Van Le, Indra Prakash, and Binh Thai Pham. 2022. "Novel approach for soil classification using machine learning methods." *Bulletin of Engineering Geology and the Environment* 81 (468): 1-17. doi:<https://doi.org/10.1007/s10064-022-02967-7>.
- Oregon State University. 2024. "Germination and Seedling Emergence." <https://forages.oregonstate.edu/>. <https://forages.oregonstate.edu/regrowth/how-does-grass-grow/developmental-phases/vegetative-phase/germination-and-seedling>.
- Oyeniran, Oyedotun Kabir. 2018. "Synthesis and characterization of carbon-based nanostructured material electrodes for designing novel hybrid supercapacitors." PhD Thesis, Faculty of Natural and Agricultural Sciences, University of Pretoria. doi:10.13140/RG.2.2.20007.50084.
- Patle, Kamlesh S, Vishvеш Panchal, Riya Saini, Yash Agrawal, and Vinay S Palaparthi. 2022. "Temperature compensated and soil density calibrated soil moisture." *Measurements* 201: 111703. doi:<https://doi.org/10.1016/j.measurement.2022.111703>.
- Pumpa, Jennifer, Peter Martin, Frank McRae, and Neil Coombes. 2013. "Coleoptile length of wheat varieties." NSW Department of Primary Industries, 1-5. [https://www.dpi.nsw.gov.au/\\_\\_data/assets/pdf\\_file/0006/459006/Coleoptile-length-of-wheat-varieties.pdf](https://www.dpi.nsw.gov.au/__data/assets/pdf_file/0006/459006/Coleoptile-length-of-wheat-varieties.pdf).
- Queensland Government. 2024. *Soil texture*. <https://www.qld.gov.au/environment/land/management/soil/soil-properties/texture>.
- Radiocontrolli. n.d. "RC-SPC1K Rain Sensor Datasheet." <https://www.radiocontrolli.com/>. [https://www.radiocontrolli.com/media/1327\\_19f7fbdeee533922c0340d47b898e025e70c0574.pdf](https://www.radiocontrolli.com/media/1327_19f7fbdeee533922c0340d47b898e025e70c0574.pdf)/o/RC-SPC1K.pdf.
- RecoChem. 2022. "Diggers methylated spirits saftey data sheet." [www.recochem.com](http://www.recochem.com). <https://www.recochem.com>.
- Rêgo Segundo, A.K., É. Silva Pinto, G Almeida Santos, and P.M. de Barros Monteiro. 2019. "Capacitive Impedance Measurement: Dual-frequency Approach." *Sensors* 19: 1-12. doi:<https://doi.org/10.3390/s19112539>.
- Sigma-Aldrich. 2024. "Solvent Miscibility Table." [www.sigmaaldrich.com](http://www.sigmaaldrich.com). <https://www.sigmaaldrich.com/AU/en/technical-documents/technical-article/analytical-chemistry/purification/solvent-miscibility-table>.
- Sulek, Alicja, and Monika Ogorkiewicz. 2020. "Impact of sowing depth and seed size on the dynamics of germination and productivity of spring wheat." *Polish Journal of Agronomy* 43: 63-69. doi:doi: 10.26114/pja.iung.421.2020.43.06.
- Texas Instruments. 2024. "TMUX405x Datasheet." [ti.com](http://ti.com). <https://www.ti.com/lit/ds/symlink/tmux4052.pdf>.
- Topp, G.C., D.R. Lapen, G.D. Young, and M. Edwards. n.d. "EVALUATION OF SHAFT-MOUNTED TDT READINGS IN DISTURBED AND UNDISTURBED MEDIA." [https://www.researchgate.net/publication/267924009\\_EVALUATION\\_OF\\_SHAFT-MOUNTED\\_TDT\\_READINGS\\_IN\\_DISTURBED\\_AND\\_UNDISTURBED\\_MEDIA](https://www.researchgate.net/publication/267924009_EVALUATION_OF_SHAFT-MOUNTED_TDT_READINGS_IN_DISTURBED_AND_UNDISTURBED_MEDIA).
- University of Washington. n.d. "Dielectric constants of Common Solvents." *UW Departments Web Server*. [https://depts.washington.edu/eoptic/linkfiles/dielectric\\_chart%5B1%5D.pdf](https://depts.washington.edu/eoptic/linkfiles/dielectric_chart%5B1%5D.pdf).
- Yang, Yang, Thomas Vervust, Frederick Bossuyt, Jan Vanfleteren, Gabriele Chiesura, Geert Luyckx, Joris Degrieck, and Markus Kaufmann. 2015. "Non-destructive evaluation of an infusion process using capacitive sensing technique." In *Emerging Technologies in Non-Destructive Testing VI*, 293-297. <https://core.ac.uk/download/pdf/55781827.pdf>.
- Yu, Limin, Wanlin Gao, Redmond R Shamshiri, Sha Tao, Yanzhao Ren, Yanjun Zhang, and Guilian Su. 2021. "Review of research progress on soil moisture sensor technology." *International Journal of Agricultural and Biological Engineering* 32-42. doi:10.25165/j.ijabe.20211404.6404.

Zareian, A, A Hamidi, H Sadeghi, and M.R. Jazaeri. 2013. "Effect of Seed Size on Some Germination Characteristics, Seedling Emergence Percentage and Yield of Three Wheat (*Triticum aestivum* L.) Cultivars in Laboratory and Field." *Middle-East Journal of Scientific Research* 13 (8): 1126-1131. doi:10.5829/idosi.mejsr.2013.13.8.651.

## Appendix A: Coleoptile Length Classification of Certain Wheat Varieties

Figure 18 shows data from a field trial conducted in 2021 comparing coleoptile length, seedling establishment and yield results at 0, 4 and 10 cm sowing depths over a range of wheat varieties. Figure 19 show a list of wheat varieties and their coleoptile group classifications (Department of Primary Industries 2024).

Variety (Coleoptile group)	Coleoptile length (cm)		Establishment (m <sup>2</sup> ) at 10cm deep	Grain yield (t/ha)	
	Filter paper	Sown at 10cm		at 10cm deep	at 4cm deep
DS Pascal (S)	6.3	4.9	27	2.3	4.4
Scepter (S/M)	7.5	5.5	31	2.5	5.0
Calibre (L)	8.5	6.7	48	3.0	4.9
Yitpi (L)	9.4	6.8	58	2.7	4.6
Halberd (VL)	12.3	7.8	100	3.3	4.2
Isd			30 (m <sup>2</sup> )	0.5 (t/ha)	0.5 (t/ha)

Figure 49: Coleoptile length, establishment rate, and yield of a range of wheat varieties at 0, 4 and 10 cm sowing depth.

Variety	Black point*	Falling number index	Coleoptile group
Brumby	MSp	6p	M
Calibre	MSp	6p	L
Catapult	S	6	M
Chief CL Plus	MS	4	M
Cutlass	MS	4	L
Denison	MS	5	M/L
Devil	MSS	3	M
DS Bennett	MSS	-	M
DS Pascal	MS	7	S
Hammer CL Plus	MRMS	4	M
Illabo	MRMS	5	M
Kinsei	S	4	M
LRPB Anvil CL Plus	Sp	2/3p	M
LRPB Avenger	MS	5p	-
LRPB Havoc	MS	3	-
LRPB Nighthawk	MS	-	-
LRPB Trojan	MS	5	-
Mace	MRMS	5	M
Magenta	MSS	3	L
Mowhawk	-	5	Mp
Ninja	MRMS*	4	S/M
Razor CL Plus	MS	4	M
Rockstar	MSS	2	M
Scepter	MS	5	S/M
Sheriff CL Plus	MS	4	-
Sting	S	4p	M/L
Valiant CL Plus	MSp	2/3p	M
Vixen	MSS	3	M
Westonia	MS*	2	M
Wyalkatchem	MS*	3	S
Yitpi	MS	5	L
Zen	MRMS	3	S

Figure 50: List of wheat varieties and their coleoptile group classifications.

## Appendix B: Deviation of Method Described by Rego Segunda et al

Rego Segundo et al demonstrate the following method for complex admittance approximation (Rêgo Segundo, et al. 2019):

$$\boldsymbol{\varepsilon}_r = \varepsilon_r' - j \frac{\sigma}{\omega \varepsilon_0} \quad (11)$$

Ohms law for AC circuits states:

$$\mathbf{V} = \mathbf{ZI} \quad (12)$$

Where  $\mathbf{V}$  and  $\mathbf{I}$  are the AC voltage and current phasors respectively and  $\mathbf{Z}$  is the complex impedance:

$$\mathbf{Z} = R + jX \quad (13)$$

Where  $R$  is resistance and  $X$  is reactance in Ohms. The admittance  $\mathbf{Y}$  is the inverse of  $\mathbf{Z}$ :

$$\mathbf{Z}^{-1} = \mathbf{Y} = G + jB \quad (14)$$

Where  $G$  is conductance and  $B$  is the susceptance in Siemens. Both  $G$  and  $B$  are dependent on the geometric configuration constant of the sensor  $k_g$ , (i.e. for the simple PPC case in equation 2,  $k_g = \frac{A}{d}$ ) and:

$$G = k_g \sigma, \quad B = k_g \omega \varepsilon_0 \varepsilon_r' \quad (15)$$

$$\mathbf{Y} = k_g \sigma + j k_g \omega \varepsilon_0 \varepsilon_r' \quad (16)$$

Taking out the factor  $j k_g \omega \varepsilon_0$  from equation 16:

$$\mathbf{Y} = j k_g \omega \varepsilon_0 \left( \frac{\sigma}{j \omega \varepsilon_0} + \varepsilon_r' \right) \quad (17)$$

Simplifying the imaginary denominator:

$$\mathbf{Y} = j k_g \omega \varepsilon_0 \left( \frac{\sigma(-j \omega \varepsilon_0)}{j \omega \varepsilon_0 (-j \omega \varepsilon_0)} + \varepsilon_r' \right) = j k_g \omega \varepsilon_0 \left( \frac{\sigma(-j \omega \varepsilon_0)}{-j^2 \omega^2 \varepsilon_0^2} + \varepsilon_r' \right) \quad (18)$$

$$\mathbf{Y} = j k_g \omega \varepsilon_0 \left( -j \frac{\sigma}{\omega \varepsilon_0} + \varepsilon_r' \right) \quad (19)$$

Using equation 11 in equation 19:

$$\therefore \mathbf{Y} = j k_g \omega \varepsilon_0 \boldsymbol{\varepsilon}_r \quad (20)$$

## Appendix C: Properties Table of Alumina Ceramics

Item		ALUMINA ( $\text{Al}_2\text{O}_3$ )															
Material Code (New)		AO201B AO4450 AO4710 AO4730 AO4840 AO484B AO4760 AO4790 AO479S AO479M AO479G AO479U AO480S AO601L															
Material Code (Old)		A201B A445 A471 A473 A484 A484B A476 A479 A479S A479M A479G A479U A480S A601L															
Appearance		Dense															
Color		Black	Dark Brown	White	White	White	White	White	Ivory	Ivory	White	Ivory	Ivory	Ivory	Ivory		
Content (%)		91	90	92	92	92	92	96	99	99.5	99.5	99.6	99.7	99.9			
Main Characteristics		<ul style="list-style-type: none"> <li>• High Frequency Insulation</li> <li>• High Mechanical Strength</li> <li>• Wear Resistant</li> <li>• High Corrosion Resistance</li> <li>• High Temperature Resistance</li> <li>• Low Light Reflectivity</li> <li>• Intercepting Reflectivity</li> <li>• High Heat Dissipation</li> <li>• Wear Resistance</li> <li>• Metallizing</li> <li>• High Mechanical Strength</li> <li>• High Wear Resistance</li> <li>• Excellent Surface Finish</li> <li>• Excellent Printability</li> <li>• High Hardness</li> <li>• High Corrosion Resistance</li> <li>• High Wear Resistance</li> <li>• High Hardness</li> <li>• High Corrosion Resistance</li> <li>• High Wear Resistance</li> <li>• High Hardness</li> <li>• High Corrosion Resistance</li> <li>• Good Plasma Resistance</li> <li>• Low Dielectric Tangent</li> <li>• High Purity</li> <li>• High Corrosion Resistance</li> <li>• Good Plasma Resistance</li> <li>• High Wear Resistance</li> </ul>															
Main Applications		<ul style="list-style-type: none"> <li>• Semiconductor Processing Equipment</li> <li>• IC Packages</li> <li>• Liner</li> <li>• Pulverizer</li> <li>• C Multi-Layer packages</li> <li>• Electromechanical Housing</li> <li>• Wear Resistant Parts</li> <li>• Wear Resistant Parts</li> <li>• Sliding Parts</li> <li>• Capslans</li> <li>• Hybrid IC Substrates</li> <li>• Heat, Corrosion and Wear Resistant Parts</li> <li>• Corrosion and Wear Resistant Parts</li> <li>• Corrosion and Wear Resistant Parts</li> <li>• Semiconductor Processing Equipment</li> <li>• Semiconductor Processing Equipment</li> <li>• Corrosion and Wear Resistant Parts</li> <li>• Semiconductor Processing Equipment</li> </ul>															
Density ( $\text{g/cm}^3$ )		JIS R 1634	3.6	3.6	3.6	3.6	3.6	3.7	3.7	3.8	3.9	3.9	3.9	3.9	3.9	3.9	
Water Absorption (%)		JIS C 2141	0	0	0	0	0	0	0	0	0	0	0	0	0	0	
Mechanical Characteristics	Vickers Hardness HV9.807N	GPa	JIS R 1610	12.0	12.7	11.8	12.3	12.3	12.3	13.7	15.2	16.0	15.7	15.2	17.2	17.5	
	Flexural Strength 3 P.B.	MPa	JIS R 1601	400	320	390	340	370	460	350	310	400	370	380	480	500	
	Compressive Strength	MPa	JIS R 1608	2,781	2,430	3,024	2,300	2,910	2,900	2,992	2,160	2,350	2,984	2,530	2,900	3,229	
	Young's Modulus of Elasticity	GPa	JIS R 1602	320	320	280	280	280	300	320	360	370	370	387	380	380	
	Poisson's Ratio	-	JIS R 1607	0.24	0.23	0.23	0.23	0.23	0.23	0.23	0.23	0.23	0.23	0.23	0.23	0.23	
	Fracture Toughness (SEPB)	MPa · m <sup>1/2</sup>	JIS R 1607	3.6	4.1	3.4	3.5	3.4	3.6	2.9	3-4	4	4.3	4.3	4.3	4.5	
Thermal Characteristics	Coefficient of Linear Thermal Expansion	$\times 10^{-6}/\text{K}$	JIS R 1618	7.0	7.3	7.1	6.9	6.8	6.6	7.2	7.2	7.2	7.2	7.2	7.2	7.2	
	Thermal Conductivity 20°C	W/(m · K)	JIS R 1611	8.0	8.1	7.9	7.8	7.7	7.6	7.9	8.0	8.0	8.0	8.0	8.0	8.0	
	Specific Heat Capacity	J/(g · K)	JIS R 1611	0.79	0.75	0.79	0.78	0.78	0.79	0.78	0.79	0.78	0.78	0.77	0.79	0.78	
	Thermal Shock Temperature Difference (Put in Water/Relative Method)	°C	JIS R 1648	150	150	150	150	150	150	150	150	180	180	180	180	180	
	Dielectric Strength	kV/mm	JIS C 2141	14	12	16	16	14	14.5	15	15	15	15	14.6	15	15	
	Volume Resistivity	$\Omega \cdot \text{cm}$		$>10^{14}$	$10^{11}$	$>10^{14}$	$>10^{14}$	$>10^{14}$	$>10^{12}$	$>10^{14}$	$>10^{14}$	$>10^{14}$	$>10^{14}$	$>10^{14}$	$>10^{14}$	$>10^{14}$	
	Dielectric Constant (1MHz)	-		$10^{10}$	$10^7$	$10^{12}$	$10^{12}$	$10^{10}$	$10^{11}$	$10^{13}$	$10^{10}$	$10^{11}$	$10^{13}$	$10^{12}$	$10^{15}$	$10^{15}$	
	Dielectric Loss Angle (1MHz)	( $\times 10^{-6}$ )		$10^8$	$10^5$	$10^3$	$10^{10}$	$10^3$	$10^5$	$10^6$	$10^4$	$10^{10}$	$10^{10}$	$10^{10}$	$10^{10}$	$10^{10}$	
	Loss Factor	( $\times 10^{-6}$ )		9.7	9.8	8.9	9.0	8.9	9.2	9.4	9.9	9.9	9.9	10	9.9	9.9	
	Nitric Acid (60%) 90°C ,24H	(Weight Loss) mg/cm <sup>2</sup>		11	20	6	6	9	4	4	2	1	1	<1	1	1	
	Sulphuric Acid (95%) 95°C ,24H			106	190	53	54	80	37	38	20	10	10	-	10	10	
	Sodium Hydroxide (30%) 80°C ,24H			0.00	1.17	-	0.32	0.14	-	0.02	0.10	0.00	0.01	-	0.05	0.01	

Figure 51: Properties Table of Alumina Ceramics (Kyocera 2024).